Imaging and modeling of pore scale processes in porous media using X-ray computed tomography and lattice Boltzmann solver

Dissertation

zur Erlangung des Grades

“Doktor der Naturwissenschaften”

im Promotionfach **Geologie/Paläontologie**

am Fachbereich

Chemie, Pharmazie und Geowissenschaften

der Johannes Gutenberg–Universität Mainz

vorgelegt von

Faisal Khan

geb. in Hangu, Pakistan

Mainz, March 2014

Imaging and modeling of pore scale processes in porous media using X-ray computed tomography and lattice Boltzmann solver

Dekan:

Tag der mündlichen Prüfung:

Abstract

Pore scale imaging and modeling is becoming a routine practice in the oil and gas industry, and has potential applications in environmental aspects of contaminant fate and transport, carbon storage, and enhanced natural attenuation. X-ray computed microtomography (μCT) is frequently used as a non-destructive 3D imaging technique for the investigation of internal structure of geologic material. The first objective of this thesis was to implement the image processing techniques that mainly involve the removal of beam-hardening artefacts, and segmentation process. The second objective was to study the combined effect of pore characteristics, porosity and pore tortuosity on the fluid flow simulation and transport modeling using the lattice Boltzmann method.

In a cylindrically-shaped geologic sample, the position of each phase was extracted with the observation that the presence of beam-hardening in the reconstructed μCT image is a radial function from the periphery to the center of the sample and thus, automatically segmented the different phases. Moreover, the beam-hardening was also removed by simply applying surface fitting to the reconstructed image data regardless of any object shape. Since, the least square support vector machine is characterized by a great degree of modularity, and it is very convenient and applicable for a large-scale pattern recognition problem, and classification task. For these reasons, the least square support vector machine was implemented as a pixel-based classification task. This algorithm proves to classify a complex multi-mineral geologic sample, but seems computationally costly in the case of a high dimensional training data set.

The dynamics of immiscible air-water phases were investigated by a combination of pore morphology and lattice Boltzmann method for drainage and imbibition processes in a 3D soil image obtained by synchrotron-based μCT. Though, the pore-morphology is a simple method which applies fitting spheres into an accessible pore space, but compatible to interpret a complex capillary pressure hysteresis as function of water saturation. A hysteresis was seen for both capillary pressure and hydraulic conductivity which was mainly caused by the inter-connected pore network, and the available pore size distribution. The hydraulic conductivity as a function of water saturation levels were compared to macroscopic calculations of empirical models and matched well, especially at higher water saturation. To predict the presence of pathogens in drinking water and waste water, the microorganisms e.g., Escherichia coli known as indicator organisms, was investigated in a soil aggregate with the effect of grain size, pore geometry, and pore water velocity. The asymmetrical and long tailed breakthrough curves, especially at higher water saturation, were caused by dispersive flow due to the interconnected pore geometry, and heterogeneity of the fluid velocity field. It was observed that the biocolloid residence is also a function of pressure gradients and colloidal size, and our simulation results supported the data that was reported in the literature.

Zusammenfassung

In der Erdöl– und Gasindustrie sind bildgebende Verfahren und Simulationen auf der Porenskala im Begriff Routineanwendungen zu werden. Ihr weiteres Potential lässt sich im Umweltbereich anwenden, wie z.B. für den Transport und Verbleib von Schadstoffen im Untergrund, die Speicherung von Kohlendioxid und dem natürlichen Abbau von Schadstoffen in Böden. Mit der Röntgen-Computertomografie (XCT) steht ein zerstörungsfreies 3D bildgebendes Verfahren zur Verfügung, das auch häufig für die Untersuchung der internen Struktur geologischer Proben herangezogen wird. Das erste Ziel dieser Dissertation war die Implementierung einer Bildverarbeitungstechnik, die die Strahlenaufhärtung der Röntgen-Computertomografie beseitigt und den Segmentierungsprozess dessen Daten vereinfacht. Das zweite Ziel dieser Arbeit untersuchte die kombinierten Effekte von Porenraumcharakteristika, Porentortuosität, sowie die Strömungssimulation und Transportmodellierung in Porenräumen mit der Gitter-Boltzmann-Methode.

In einer zylindrischen geologischen Probe war die Position jeder Phase auf Grundlage der Beobachtung durch das Vorhandensein der Strahlenaufhärtung in den rekonstruierten Bildern, das eine radiale Funktion vom Probenrand zum Zentrum darstellt, extrahierbar und die unterschiedlichen Phasen ließen sich automatisch segmentieren. Weiterhin wurden Strahlungsaufhärtungeffekte von beliebig geformten Objekten durch einen Oberflächenanpassungsalgorithmus korrigiert. Die Methode der „least square support vector machine" (LSSVM) ist durch einen modularen Aufbau charakterisiert und ist sehr gut für die Erkennung und Klassifizierung von Mustern geeignet. Aus diesem Grund wurde die Methode der LSSVM als pixelbasierte Klassifikationsmethode implementiert. Dieser Algorithmus ist in der Lage komplexe geologische Proben korrekt zu klassifizieren, benötigt für den Fall aber längere Rechenzeiten, so dass mehrdimensionale Trainingsdatensätze verwendet werden müssen.

Die Dynamik von den unmischbaren Phasen Luft und Wasser wird durch eine Kombination von Porenmorphologie und Gitter Boltzmann Methode für Drainage und Imbibition Prozessen in 3D Datensätzen von Böden, die durch synchrotron-basierte XCT gewonnen wurden, untersucht. Obwohl die Porenmorphologie eine einfache Methode ist Kugeln in den verfügbaren Porenraum einzupassen, kann sie dennoch die komplexe kapillare Hysterese als eine Funktion der Wassersättigung erklären. Eine Hysterese ist für den Kapillardruck und die hydraulische Leitfähigkeit beobachtet worden, welche durch die hauptsächlich verbundenen Porennetzwerke und der verfügbaren Porenraumgrößenverteilung verursacht sind. Die hydraulische Konduktivität ist eine Funktion des Wassersättigungslevels und wird mit einer makroskopischen Berechnung empirischer Modelle verglichen. Die Daten stimmen vor allem für hohe Wassersättigungen gut überein. Um die Gegenwart von Krankheitserregern im Grundwasser und Abwässern vorhersagen zu können, wurde in einem Bodenaggregat der Einfluss von Korngröße, Porengeometrie und Fluidflussgeschwindigkeit z.B. mit dem Mikroorganismus Escherichia coli studiert. Die asymmetrischen und langschweifigen Durchbruchskurven, besonders bei höheren Wassersättigungen, wurden durch dispersiven Transport aufgrund des verbundenen Porennetzwerks und durch die Heterogenität des Strömungsfeldes verursacht. Es wurde beobachtet, dass die biokolloidale Verweilzeit eine Funktion des Druckgradienten als auch der Kolloidgröße ist. Unsere Modellierungsergebnisse stimmen sehr gut mit den bereits veröffentlichten Daten überein.

List of Publications

This thesis research contains three Journal Papers that are listed here. The first two are published in international journals; the third paper is in review process.

Paper I

Khan, F; Enzmann, F; Kersten, M; Wiegmann, A; Steiner K. 3D simulation of the fluid velocity field in a heterogeneous soil aggregate on basis of nanotomographic imaging and LBE solver. *Journal of Soils and Sediments 2012;12:86–96*

Paper II

Jovanovic, Z; **Khan, F**; Enzmann, F; Kersten, M. Simultaneous segmentation and beam-bardening correction in computed microtomography of rock cores. *Computers & Geosciences 2013;56:142–150*

Paper III

Khan, F; Enzmann, F; Kersten, M. Pore-morphology and lattice Boltzmann approach to modeling unsaturated soil capillary hysteresis and permeability tensor. *Submitted to Soil Science Society of America Journal, 2013*.

List of Conferences attended

Parts of the results of this thesis were presented as the following talks and posters:

Abstract and Oral presentation

Chauhan, S; Rühaak, W; Enzmann, F; **Khan, F**; Mielke, P; Kersten, M; Sass, I. Comparison of micro X-ray computer tomography image segmentation methods: Artificial neutral networks versus least square support vector machine. *Proceedings of the 15th annual conference of the international association for mathematics geosciences, Madrid, Spain. 2–6 September, 2013. PP. 141-145*

Abstract and Oral presentation

Khan, F; L, Leon; Enzmann, F; Kersten M. Time resolved micro tomographic data from multiphase flow experiments: Image analysis and SatuDict simulation. *Material images, material models, and material property prediction–GeoDict User Conference, Kaiserslautern, Germany. 3-4 September, 2013.*

Abstract and Poster presentation

Khan, F; Enzmann, F; Kersten, M. Transport of biocolloids at the pore-scale under saturated and unsaturated conditions: Modeling and imaging. *Biohydrology conference, Landau/Pfalz, Germany. 21–24 May, 2013.*

Abstract and Poster presentation

Khan, F; Enzmann, F; Kersten, M; Becker, J; Wiegmann, A. Quantitative description of two phase (air-water) system by capillary pressure-saturation-relative permeability relationship in a soil aggregate. *2nd International conference on Hydropedology, Leipzig, Germany 22–27 July, 2012.*

Abstract and oral presentation

Khan, F. Enzmann ,F; Kersten, M. Pore scale investigation: Characterization and modeling. *Connecting imaging, spectroscopy and microbiology, Bayreuth, Germany. 5–6 March, 2012*

Table of Contents

Annex

List of Figures

1 Introduction

1.1 Relevance

Pore scale modeling is the fundamental approach for modeling single or multiphase flow in porous media, which is of great importance to many scientific and engineering concerning of; groundwater and vadose zone flow and transport, contaminant remediation, oil recovery processes, and energy-related activities such as geothermal energy production, and geologic sequestration of CO_2. This approach provides a way for the parameterization of macro-scale constitutive parameters i.e., porosity, and permeability that in effect govern the overall performance of many flow and transport models. Pore scale modeling is a challenging task in a complex and tortuous nature of the pore structures that require techniques for obtaining the integral description of the pore geometries, and methods to analysis and quantify pore structure, and efficient and robust numerical methods of handling complex geometries.

The advent of X-ray microtomography (μCT) has made it possible to obtain three-dimensional (3D) images with a resolution of only a few microns which is sufficient to capture the internal structure of wood, composites, and pore space of reservoir rock cores and soil. This allows for characterization of pore space structure, and observation of pore scale processes. Polychromatic X-ray sources are used universally in conventional laboratory-based μCT technology to obtain adequate intensity of photons which consists of different energies. In polychromatic radiation, the average energy of the X-ray beam increases as the beam propagates through a material since the lower energy of the X-ray are preferentially attenuated. This implies the grey levels of the projection data are not linear with the material thickness and consequently, the reconstructed CT image produces some visual distortions, such as pronounced edges, and artefacts. Beam-hardening (BH) is one such artefact, which produces false line integrals due the photon-energy dependence of the attenuation co-efficient. The presence of BH artefact remains a problem in 3D image processing and hampers correct image analysis i.e., segmentation process. A variety of algorithms and schemes are developed for eliminating BH artefacts including pre-filtering or hardware filtering, dual-energy and post-processing techniques. Recently, monochromatic synchrotron-based μCT has been introduced as a powerful tool for an effective visualization of the morphological features of the pore-space geometry at a voxel resolution down to microns. Illuminating the sample with a monochromatic beam has the advantage of mitigating BH artefacts.

Image segmentation is one of the crucial steps in image processing. The segmentation of μCT images is very important for the measurement of properties as well as detecting and recognizing

object (mineral composition, pore space). In the literature, a diversity of segmentation methods has been developed and the outcome result is significantly related to the image quality and with the sensitivity of the technique itself employed. The properties of the resulting segmented image can vary greatly with small changes in segmentation parameters.

A pore characterization of geomaterials i.e., pore-size distribution, porosity, and pore geometry structure are some of the most important material properties for the investigation of the permeability of fluid flow in porous media. The permeability tensor (hydraulic conductivity) of fluid flow is not only dependent on the connectivity of pore spaces allowing the fluid that flows through it, but also the conditions imposed by the flow process. In recent years, the lattice Boltzmann (LB) equation for modeling of fluid flow and transport has received the most attention because of its simple formulation and applications in complex and multi scale flows. LB method follows simple and local update rules based on the motion and collision of particles on a cubic lattice (voxels) of a digital μCT image to approximate Navier Stokes equation for the fluid flow simulation at the pore level. With increasing μCT images spatial resolution, it has become feasible to visualize colloids and particles in porous media. A recent advancement in computer technology introducing high performance computing (HPC) and development of easy-to-use graphical user interface software, effective 3D visualization of generated results from those simulations plays an important role in understanding the complex dynamics of fluid flow data (velocity vector field) and transport processes (solute/colloid tracking) at a pore scale level.

1.2 Motivation and objectives

Driven by the technological and computational progress, high-resolution μCT is a frequently used nondestructive 3D imaging and analysis technique for the investigation of internal structures of geomaterials i.e., rock cores, soil. The grayscale images that are produced from μCT commences by performing image processing i.e., noise reduction, artefacts removal, and image segmentation. Segmentation is dependent on the choice of approach and introduces a major uncertainty in our interpretation of the results. The pore structure and the physical characteristics of a porous medium and the fluid-fluid interface and fluid distribution in the pore volume determine several macroscopic parameters of the flow and transport processes and is a subject of significant scientific and environmental interest, for example, groundwater contamination, mass transfer process such as retention of organic compounds and biocolloids, enhanced natural attenuation and bioremediation, water treatment systems, enhanced oil and gas recovery.

To achieve our grand goal, the systematic implementation of methods and simulation strategy that were employed, is shown in Fig. 1.

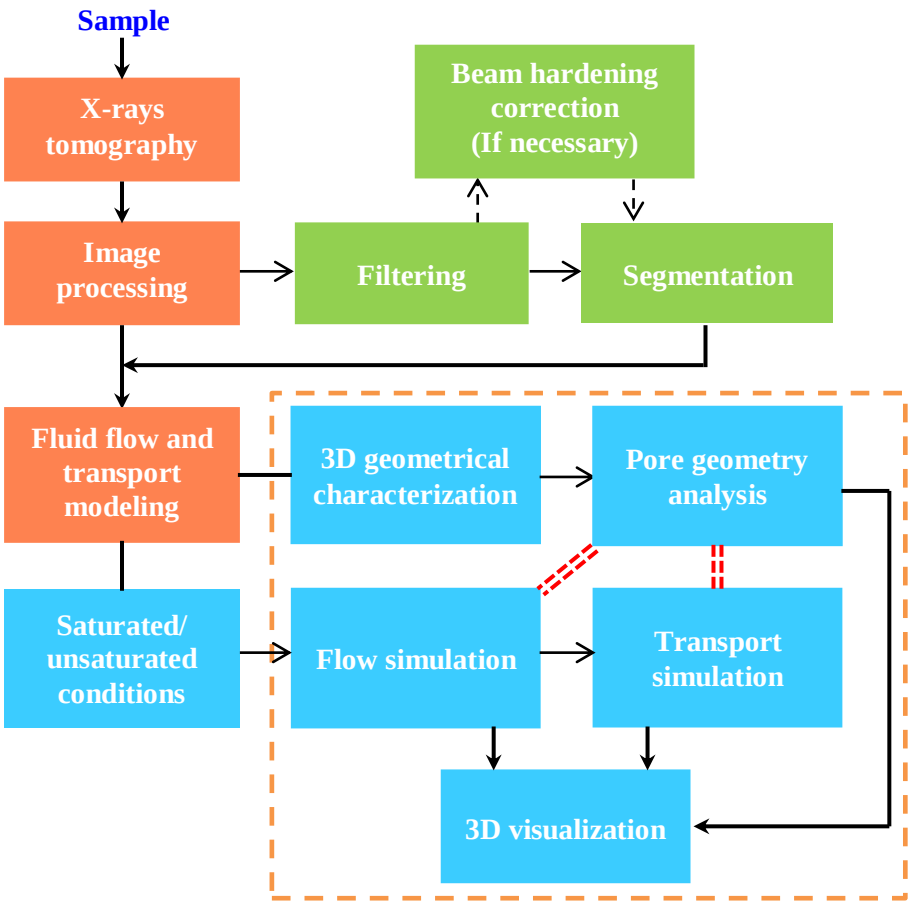

Fig. 1 Schematic illustration of our research work

The two main objectives of this thesis are:

(i) µCT Image processing

The reduction of noise is one of the first important tasks in image processing. Spatial filtering has been used effectively for noise reduction in tomography. Moreover, a polychromatic character of the µCT is posed by the existence of beam-hardening artefacts that affect the quality or hamper the subsequent segmentation process. Therefore, the removal of beam-hardening image artefact, and data image classification originated from laboratory-based µCT

technology is the vital steps for image data analysis to estimate mineral composition, and pore/fractures geometry.

(ii) Pore scale fluid flow and transport modeling

The second part of this thesis is about pore scale fluid flow and transport modeling in a porous medium. The main objective of this work is to understand and interpret the effect of complex pore geometry on the predictive fluid flow and particle breakthrough curves under saturated and unsaturated flow conditions. Also, the 3D visualization of pore scale processes is an important tool to interpret the modeling results.

1.3 Thesis Outline

A more detailed description of the bulk part of the performed work has been reported in three Journal Papers enclosed in this thesis. The experimental set of μCT technology (both laboratory-based and synchrotron-based), and data image acquisition and reconstruction can be found in Papers **I** & **II**, and therefore is not presented here. The description of geomaterial properties used for image segmentation, and pore scale simulation can be found in the introductory part of each chapter.

Chapter **2** presents the summary of the implementation of two methods dealing with BH correction and segmentation in cylindrically shaped multi-mineral geologic samples i.e., rock cores. In Section 2.1, we introduced the first method that simultaneously correct beam-hardening and segment the image data by extracting useful information of BH and X-ray attenuation values for each phase. In Section 2.2, the second method introduces the segmentation as a classification task (labeling image) by utilizing least square support vector machine on the BH corrected image done by surface fitting algorithm.

Chapter **3** introduces the summary of the research work leading up to simulating single phase flow and solute transport in a saturated and unsaturated porous media, here soil peds, using LB method. In Section 3.1, we present the results of water permeability tensor of different region-of-interests (ROI's) in a saturated soil aggregate. The variation in parameters of geometrical characterization and hydraulic conductivity values of three independent ROI's are also discussed. The results of the capillary pressure hysteresis and water permeability tensor in unsaturated soil aggregate are presented in Section 3.2. In addition, the fluid-fluid interfacial area as a function of

water saturation is also discussed here. The results of biocolloid transport with different particle sizes under different pressure gradient in a variably soil aggregate is presented in Section 3.3. For the better interpretation of results, 3D visualization of flow simulations and particle tracking are also presented.

Finally, the conclusions and future perspectives can be found in chapter **4** & **5**, respectively.

2 Image processing

After the reconstruction of grey scale μCT images, digital image processing deals with the manipulation and analysis of images by using computer algorithm. The μCT images contain a certain level of noise and artefacts that severely hamper the segmentation process. Spatial filtering is one of the choices that have been used effectively for noise reduction in tomography. We employed 3D median filter technique, a smoothing (low pass) filter. The window size masking (3×3×3) replaces a pixel by the median of all defined window size pixels in the neighborhood. After the filtering, we employed different techniques to deal with beam-hardening (BH) artefacts and image segmentation which are discussed below.

2.1 Simultaneous segmentation and beam-hardening correction in computed micro-tomography of rock cores

The image of multi-mineral evaporite rock core composed of anhydrite with halite-sealed factures at a spatial pixel resolution of 53 μm was obtained by polychromatic μCT. A variety of algorithms and schemes are developed for eliminating BH artefacts including pre-filtering or hardware filtering, dual-energy and post-processing techniques. We proposed a method that corrects BH artefact and segment multi-mineral of cylindrical shaped geologic samples, simultaneously. It does not require any prior knowledge of the X-ray spectrum and attenuation coefficients of the material. The method is based on the observation that the BH artefact in the reconstructed CT image is not only related to each material but is also a radial function, i.e. the distance of material from the center of cylinder. Using this observation, the method acquires the information of BH artefacts to distinguish different phases of a material. The procedure proceeds to attain information of one particular phase reconstructed attenuation values from the center to the periphery in order to construct artificial object. The arithmetic difference of zero (± error) between measured data and an image of artificial object data allows us to attain information of that phase present in the whole sample. The presence of another phase can be achieved only if the difference is smaller or bigger than the error. The repetition of this approach for all different phases yields the segmented image (Fig. 2c).

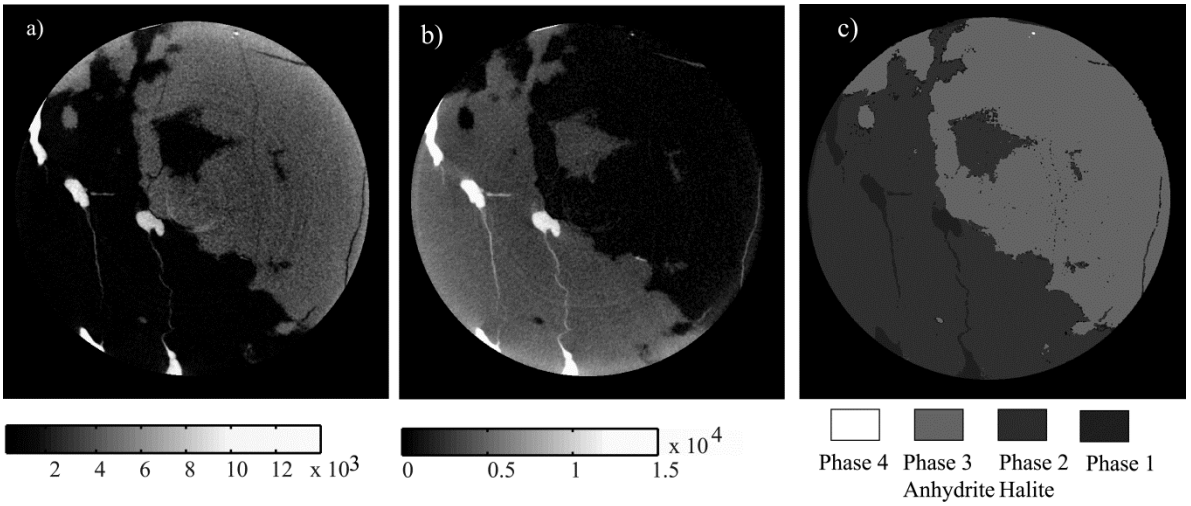

Fig. 2 (a) The original evaporite sample image and (b) the arithmetic difference between the original image and image for a calculated mono-mineral assemblage. A result value around zero means that the targeted mineral is present at that position. (c) Final segmented image for an evaporite sample, following a stepwise arithmetic-difference assignment approach shown in (b).

2.2 Beam-hardening correction and pixel-based classification of microtomography images of rock cores using surface fitting and least square support vector machine

The method is tested on the μCT image of multi-mineral rock core sample which is composed of anhydrite, clay minerals and cracks/fractures as shown in Fig. 3a. The pixel spatial resolution of the image is 42 μm. The consequence of the presence of BH artefact is that for the same solid phases the attenuation values varies across the whole sample. Also, the attenuation value at the periphery is higher than in the central regions of sample. Thus, data values of a line-profile across the reconstructed image shows a non-linear trend i.e., parabola (see red curve in Fig. 3c). Consequently, the grey scale values of one phase overlap with the remaining phase's values regardless at any positions in a sample which extremely hampered the segmentation process. As a post-processing technique, the BH artefact is removed and corrected by fitting a 2D polynomial i.e., quadratic surface to the reconstructed CT data (2D slice). The implementation of fitting surface has been done in MATLAB®.

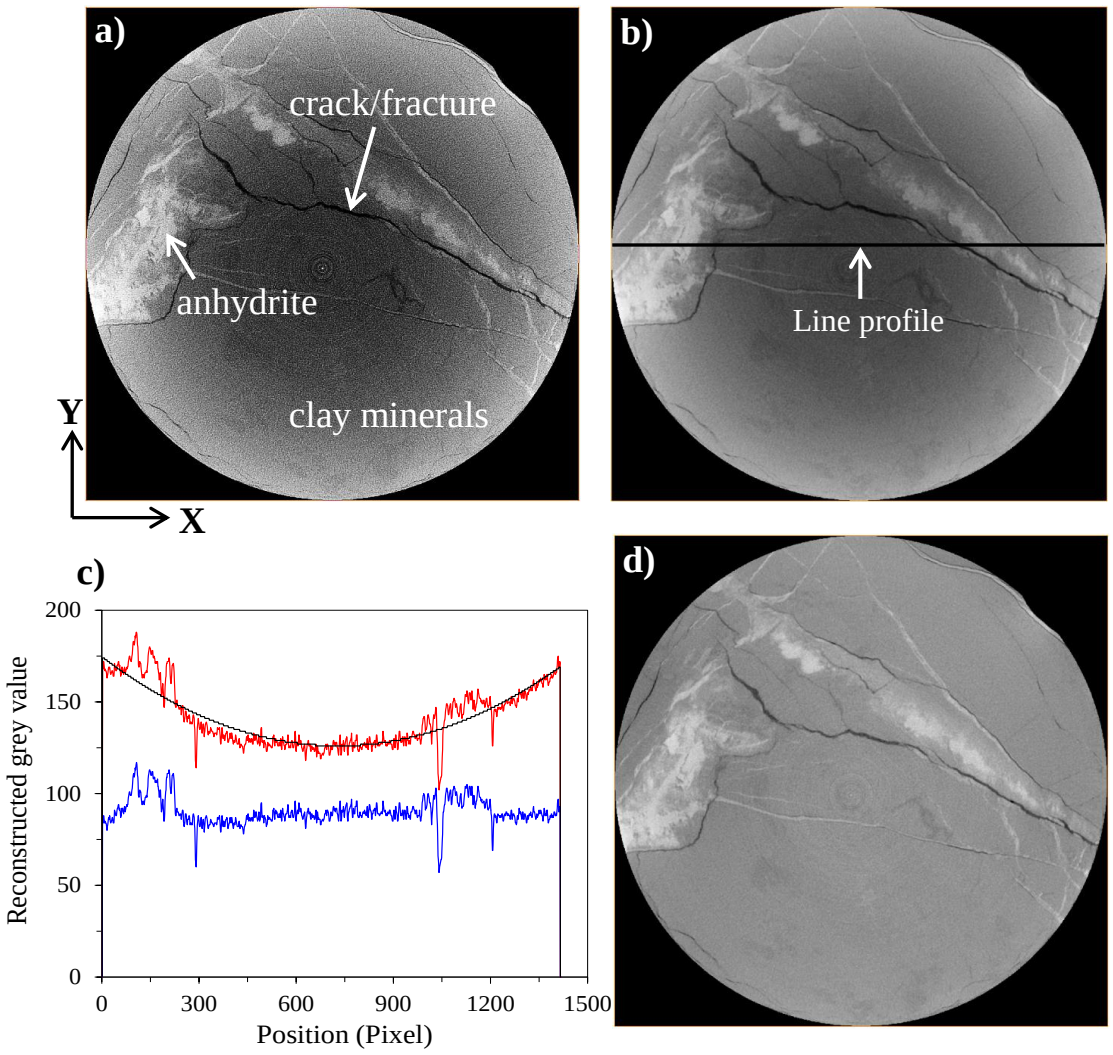

Fig. 3 Image processing by applying filtering and BH correction where (a) original sample with noise and BH artefacts, (b) the data represent 3D median filtering result, (c) the BH correction where the red color curve represent the original data values of the horizontal cross-section in (b), the fitted curve is represented by solid black curve, and blue color curve is the result of the difference between data values and fitted curves at each pixel values, (d) is the BH corrected image.

The surface fitting (i.e., 2nd order polynomial) has a mathematical expression of the form:

$$P(x_k,y_k)=a_1+a_2x+a_3y+a_4x^2+a_5xy+a_6y^2,\ k=1,2,...,N, \quad (1)$$

for some choice of unknown coefficients $a_1,a_2,\ldots,a_6$.

Consider $f_k \in (x_k,y_k), k=1,2,....N,$ are arbitrary data points of the 2D slice. The normal equations for fitting a polynomial (Eq. 1) can be expressed in a matrix-vector form as:

$$M=\begin{bmatrix} 1 & x_1 & y_1 & x_1^2 & x_1y_1 & y_1^2 \\ 1 & x_2 & y_2 & x_2^2 & x_2y_2 & y_2^2 \\ . & . & . & . & . & . \\ . & . & . & . & . & . \\ . & . & . & . & . & . \\ 1 & x_N & y_N & x_N^2 & x_Ny_N & y_N^2 \end{bmatrix}, \quad \mathbf{a} = \begin{bmatrix} a_1 \\ a_2 \\ a_3 \\ a_4 \\ a_5 \\ a_6 \end{bmatrix}, \quad \mathbf{f} = \begin{bmatrix} f_1 \\ f_2 \\ . \\ . \\ . \\ f_N \end{bmatrix} \tag{2}$$

The Eq. 2 can be solved to yield the solution vector **a** by,

$$M^TM\,\mathbf{a}=M^T\mathbf{f} \tag{3}$$

The solution of Eq. 3 for **a** determine the best fit of polynomial of Eq. 1 to a given set of data points (Fig. 3c). The final BH corrected image is the residual data which is the difference of surface elevation values and original values (Fig. 3d).

Later, we performed pixel-by-pixel multi-classification (here 3- classification) by utilizing least square support vector machine (LS-SVM). To do this job, we implemented MATLAB LS-SVMlab toolbox (www.esat.kuleuven.be/sista/lssvmlab/). Basically, the LS-SVM is derived from a non-linear support vector machines (NL-SVM) therefore some basic work on NL-SVM for classification problems is reviewed here. The NL-SVM method maps the input vector into the high dimensional feature space by some non-linear mapping called Kernel function. Therefore, NL-SVM is often named as "Kernel-based classifier". The target is to construct the optimal separating hyperplane in the feature space as shown in Fig. 4.

To solve pattern classification problems, let $\{y_i, x_i\}_{i=1}^N$ is a set of *N* data points, where $x_i \in R^n$ denote n-dimensional training inputs and $y_i \in R$ is the associated output class label such that $y_i \in \{\pm 1\}$. Using the non-linear vector function $\varphi(\cdot)$ which maps the original input space into a high-dimensional i.e., *i*-dimensional feature space, the SVM is aiming to construct a classifier i.e., the optimal separating hyperplane of the form:

$$w^T\varphi(x_i)+b \geq 1, \qquad \text{if } y_i=+1, \tag{4}$$

$$w^{\mathrm{T}}\varphi(x_i)+b\le -1, \qquad \text{if } \mathrm{y}_i=-1, \tag{5}$$

which is equivalent to

$$\mathrm{y}_i[w^{\mathrm{T}}\varphi(x_i)+b]\ge 1, \quad i=1,...,N, \tag{6}$$

where w is an i-dimensional vector (= $[w_1, w_2, \ldots w_i]^{\mathrm{T}}$) and b is a bias term.

The LS-SVM method is aiming to construct a classifier of the form:

$$y(x)=\operatorname{sign}\left[\sum_{i=1}^{N}\alpha_i \mathrm{y}_i H(x,x_i)+b\right], \tag{7}$$

where α_i's are positive real constant, and $H(x,x_i)$ is the kernel function dealing linearly non-separable data in a high-dimensional feature space.

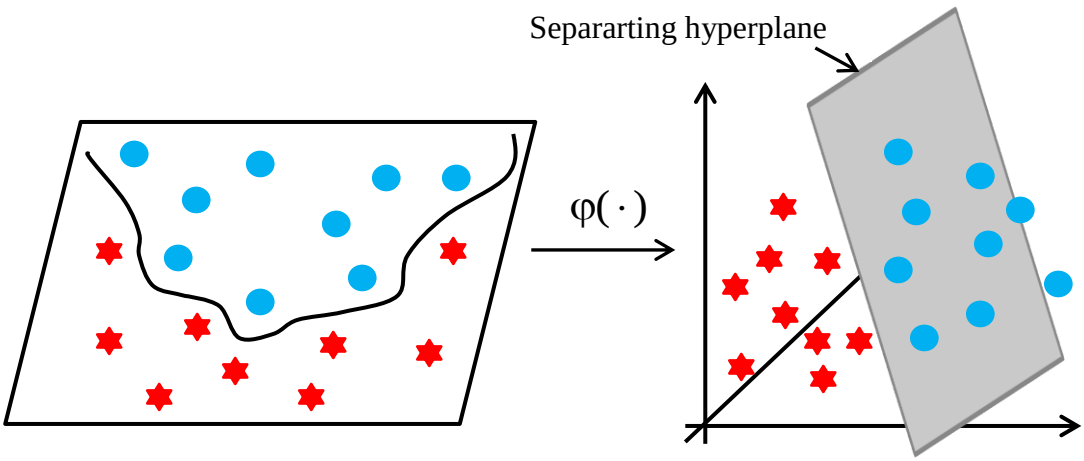

Fig. 4 LS-SVM data classification: left diagram shows the complexity of data classification in two dimensions, whereas the right figure represents the classification in higher dimensions.

Thus, the output of LS-SVM is a linear combination of the training data values projected onto a high dimensional space through the use of kernel functions. In this research only the Gaussian Radial Basis Function (RBF) kernel is implemented in LS-SVM classifier because of its high accuracy in data set classification, and is given by,

$$H(x,x_i)=\exp(-\|x-x_i\|^2/\sigma^2), \tag{8}$$

where σ^2 is the bandwidth of the Gaussian RBF kernel.

The generalization performance of the model was done by “Tuning” which estimates two extra parameters of LS-SVM model. One is the regularization parameter which determines the trade-off between the fitting error minimization and smoothness, and the other is the bandwidth of the Gaussian RBF kernel. Both with- and without BH corrected images (Fig. 3 b & d) were exposed to the LS-SVM classification. The image is grouped (classified) among three different classes of fracture (I), anhydride (II), and clay mineral (III). From these images, certain regions were manually chosen for training as shown in Fig 6a. This is done carefully to that the regions selection of the corresponding class do not contain overlapping boundaries with another class.

The proposed methodology of employing LS-SVM is shown in Fig. 5

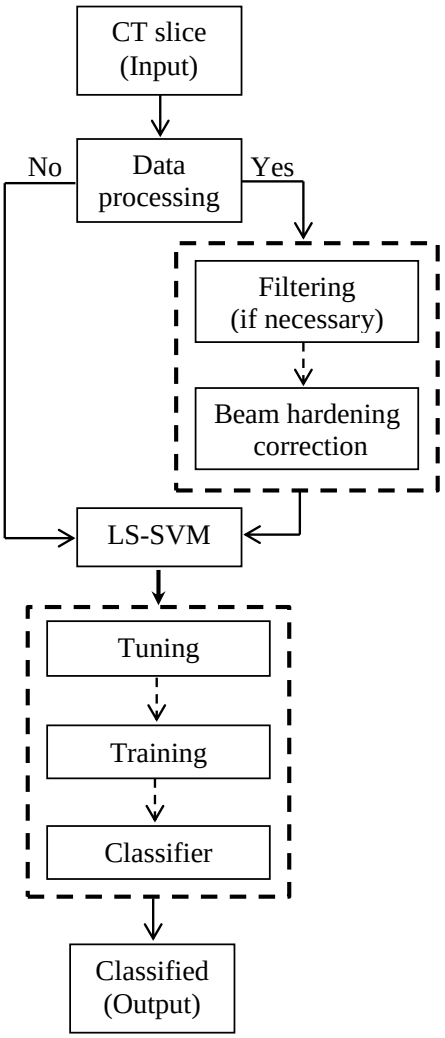

Fig. 5 The flow chart of our proposed method using LS-SVM

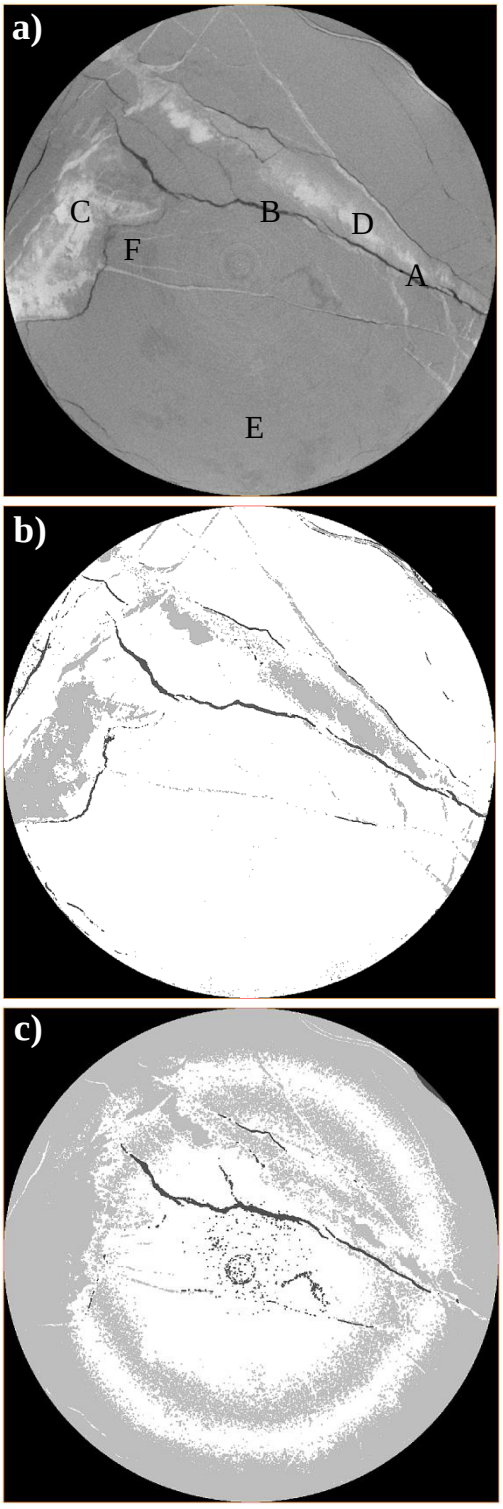

Fig. 6 Image pixel-based classification using LS-SVM. (a) Selection of pixels for training in original 3D median filtered image, (b) multi-classified of BH corrected image, (c) multi-classification of image without BH correction. Light dark color is fracture, grey color is anhydride, and white color shows clay minerals.

The number of data trained for all classes was 1755 pixels which is 0.1 % of the total pixels in the image. The remaining pixels were treated as a new data set (test data). The output classified image in which each distinguishes entity (or phase) was labelled by a single integer value (Fig. 6 b & c). All classification results could have an error rate and the classification results which can be evaluated by the performance measure i.e., Receiver Operating Characteristic (ROC). The ROC is a statistical measure of the performance of a binary classification test. It provides tools to select possibly optimal models in the analysis of decision making. ROC plots relationship between the true positive rate (sensitivity) and the false positive rate (specificity). The multi-component sample is grouped into two classes of anhydrite, and fractures and clay minerals to measure binary ROC for both with, and without BH artefact image (Fig. 6b). For the ROC parameters, the area under the curve (AUC), Sensitivity, Specificity, and Accuracy were calculated under certain threshold values. It is noted that ROC is implemented only on the training set data.

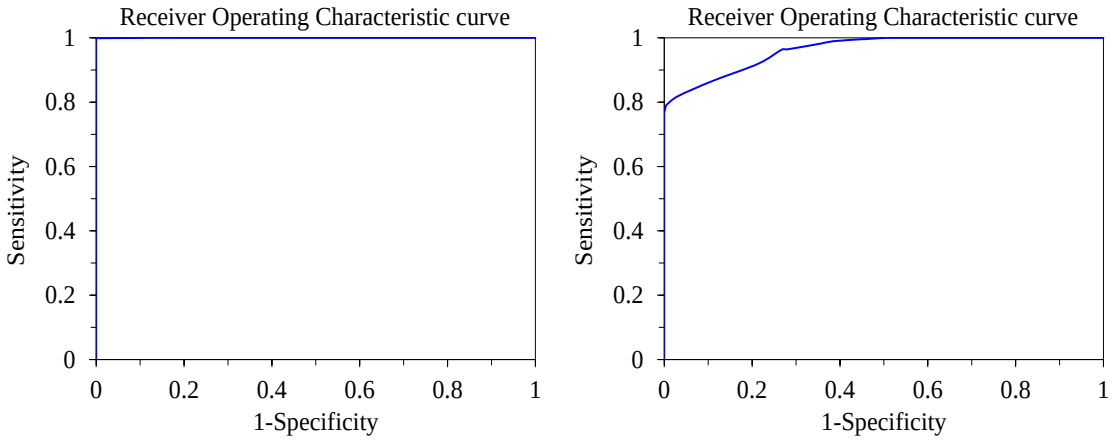

Fig. 7 Receiver-Operating Characteristic curve analysis of LS-SVM classifier on the BH corrected image (left), and without BH corrected image (right).

The ROC parameters of AUC, Sensitivity, Specificity, and Accuracy for the beam-hardening corrected image were 0.998, 99.98%, 99.75% and 99.82%, and for the without beam-hardening corrected image were 0.963, 81.88%, 96.88%, and 88.71%. The performance measure results on the pixel-based grey-value training set data showed that the probabilistic error rate is higher in the beam-hardening effected images, and consequently, misclassified the testing data (Fig. 6c & Fig. 7). It is observed that the variability of output classification results may vary with the total amount of training data set, and the selection of pixel positions for each phases in sample. Therefore, for the optimal classification result, it is always desirable to choose the sufficient training data set that includes pixel information for each phase at all positions in a sample.

3 Pore scale fluid flow and transport modeling

The porous media, here soil peds used in this research was collected from the "Ap" horizon, from Scheyern near Munich (Germany), and classified as a Luvisol that had developed from weathered loess. The soil textural components are 40 wt. % sand, 45 wt. % silt and 15 wt. % clay, and dry bulk density of 1.50 ± 0.04 g cm^{-3}. A synchrotron nano-CT is used to extract 3D images (2048^3 voxels) of soil aggregate at the spatial resolution of 0.74μm. At the pore-scale, the pore-water velocity is influenced by the hydraulic gradient, the porosity, and the permeability distribution. It is also well-known that the dynamics of fluid flow is directly linked to the pore space geometry and connectivity of the pores structure in a porous media. The transport of biogenic colloid , Escherichia coli (E. coli), as indicator organisms, is investigated in soil aggregate, and is of vital interest for the assessment of risk from pathogens in groundwater and waste water.

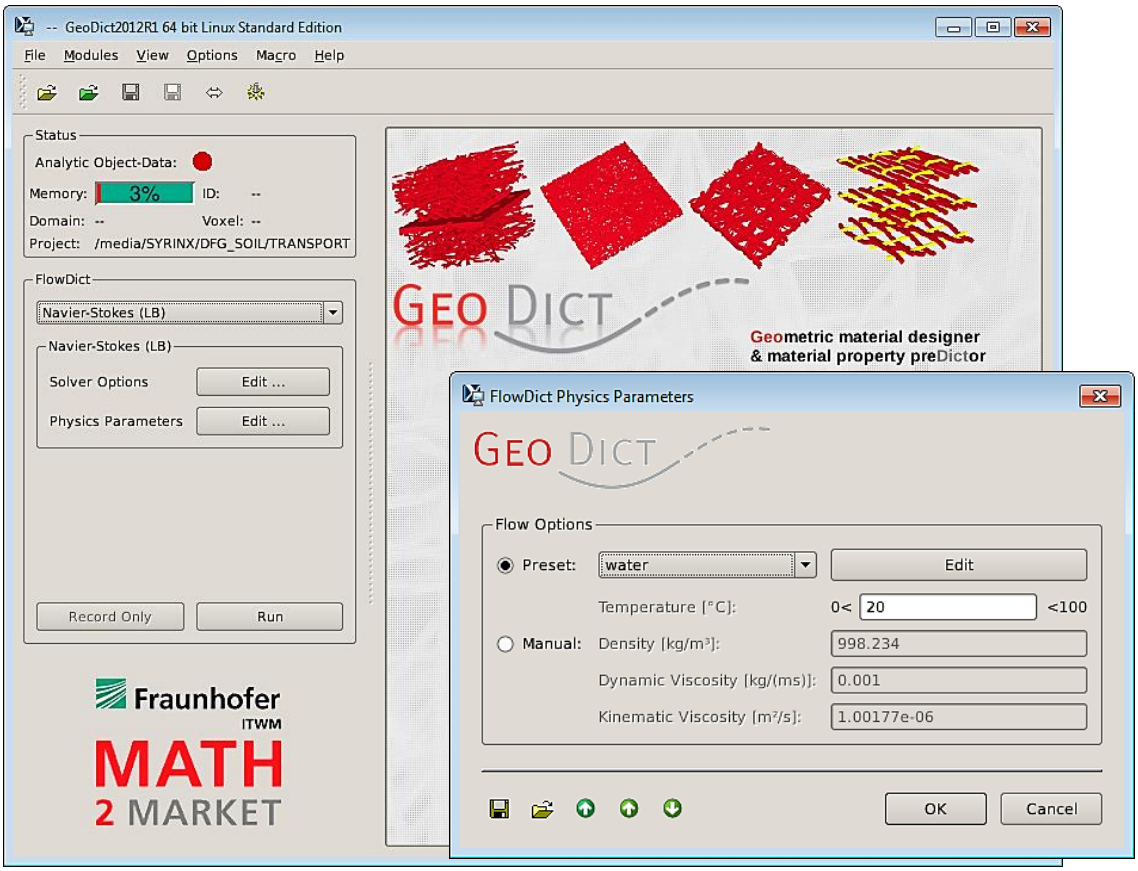

Fig. 8 Graphical User Interface of GeoDict software for fluid flow simulation

The numerical simulations (fluid flow and transport) were performed using the commercial software program package GeoDict (http://www.geodict.com), which was developed by Fraunhofer ITWM and distributed by Math2Market GmbH, Kaiserslautern, Germany (Fig. 8). A high-performance computer (HPC) comprising four Interlagos processors (64 cores), and a total RAM capacity of 512 GB was utilized.

3.1 3D simulation of the permeability tensor in a soil aggregate on basis of nanotomographic imaging and LBE solver.

Before μCT technology, 3D pore characterization was done by reconstructing 3D porous media through statistical models. The recent technological evolution in CT, complex pore-networks in 3D down to nano-scale can be imaged. Due to the restricted High Performance Computing (HPC) capacity, it is always desirable to extract region-of-interest (ROI) as the representative of the whole sample. We selected three ROI's (500×500×1000 voxels) in different locations of the soil aggregate to evaluate the geometrical variability and also that in flow simulation results. For the characterization of the pore structure, we estimated pore size distribution (PSD), porosity (open connected), and specific surface area which are some of the most important material properties for the investigation of water-pore velocity i.e., 3D flow velocity field. The estimation of spatial pore size correlations and pore connectivity enables us to determine the percolation pathways (dual porosity). After the geometrical quantification and imaging of 3D pore structure, the heterogeneous fluid velocity field (permeability tensor) in the pore space (fully water saturated) of soil aggregate is simulated by applying the lattice Boltzmann (LB) solver with the no-slip boundary condition. To achieve a unique LB solution, a fluid density of 998 kg m^{-3} and fluid viscosity of 1 g $m^{-1}s^{-1}$ are applied as input water flow parameters in the model domain. The model specifications and flow boundary conditions can be found in Paper **I**. The fluid velocity vector field at the local pores is determined by the difference in pressure gradients (Fig. 8). Consequently, gross parameter (coefficient) of Darcy's law such as the effective saturated hydraulic conductivity (K_s) is determined for all ROI's. Later, the results were compared with the prediction of empirical model which is based on the standard soil textural information, and bulk density. The simulation result of K_s confirms that our soil aggregate sample has more connected macro- and mesopores network in the *z*-direction than *x*, & *y*- directions. Also, the differences in the results of three ROI's selection indicate the impact of structural pattern on the soil characteristic property.

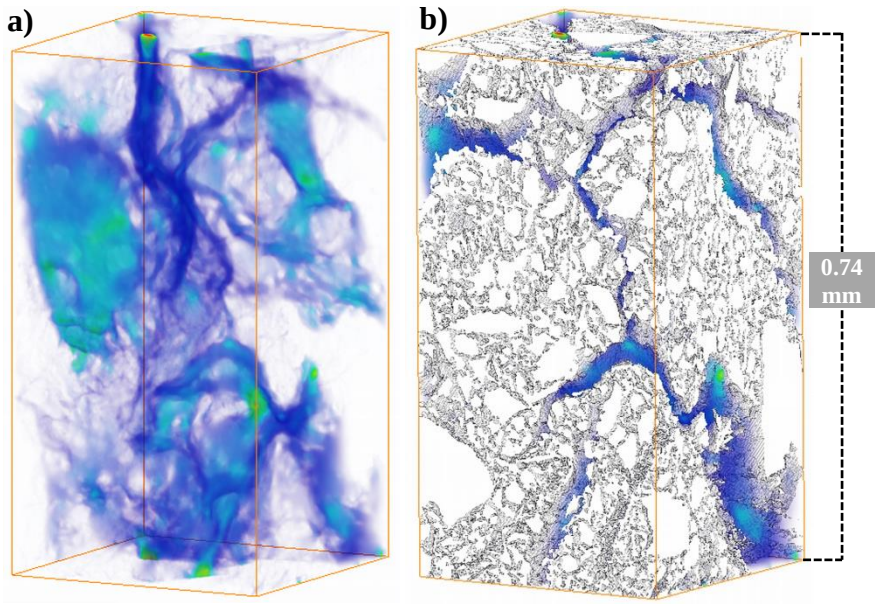

Fig. 9 3D visualization of LB simulation of velocity vector field along z-direction at (a) shows the distribution magnitude in the pore geometry, and (b) the same magnitude distribution imaged with solid matrix. The blue to red colors depict the lower to higher fluid velocities at local pores. The moderate fluid velocity is 2×10^{-3} ms^{-1} (green color).

The much lower value of K_s predicted by one of our empirical model shows the lack of its capability of predicting K_s in a heterogeneous anisotropic porous medium. Moreover, the LB solver has proven numerically accurate and stable dealing the 3D image boundary conditions and the structure complexity of the porous medium.

3.2 Pore morphology and lattice Boltzmann approach to modeling unsaturated soil capillary hysteresis and permeability tensor

The soil properties that relate to the movement of fluid flow in the unsaturated zone are the pore-size distribution, soil-water retention, and hydraulic conductivity. The water retention relationships emerge as the result of the dynamics of the immiscible air-water phase interface. A well-known macroscopic effect of this relation is the hysteresis observed during cycles of wetting and drainage. Also, it is determined that air-water interfacial area (A_{awi}) is a vital parameter for investigation of flow processes in porous media. Therefore, the primal focuses of this study is to incorporate a linkage between spatial pore network and the macroscopic constitutive relationships between the

capillary pressure, water saturation level, and interfacial area (P_c–S_w–A_{awi}) in a variably saturated porous soil medium. Secondly, we investigated the effects of the spatial distribution of air on water movement as a function of the water saturation i.e., a relationship between hydraulic conductivity (K) and water saturation (S_w) for both drainage and imbibition cycles.

In this study, the same material properties (texture, density) of soil aggregate but of different pore structure was utilized to perform pore-scale modeling. The 3D image dimensions were 500 × 500 × 1000 voxels, with a spatial resolution of 0.74 μm. The P_c–S_w–A_{awi} curves were obtained by the simulation of static two-phase (air-water) distribution for both drainage and imbibition process employing pore morphology based (PMB) approach. The PMB approach operates with several morphological processes by fitting structural element (spheres) into an accessible pore space assigned by a characteristic pore radius parameter. It is noted that PMB algorithm for drainage simulation begins with a maximum pore radius, and for imbibition simulation it starts from the minimum accessible pore radius. A hysteresis was observed between drainage and imbibition cycles in the P_c–S_w curves because of the pore-size distribution and the connected-pore geometry. Moreover, the P_c–S_w were also investigated with fluid trapping i.e., by the integration of residual water saturation in the drainage simulation and residual air saturation in the imbibition simulation. Afterwards, for each drainage and imbibition cycles, the 3D images of air-water distribution by PMB approach were used to investigate the fluid/fluid interfacial area. The A_{awi}–S_w curves suggested that the air-water interfacial area increased as the water saturation decreased and attained the maximum value at the moderate water saturation. A_{awi} was much higher for imbibition than for drainage, especially at moderate water saturation. To exemplify these results, 3D imaging of fluid phase distribution during drainage at S_w = 0.55 and during imbibition at S_w = 0.53 are shown in Fig. 8. The difference of air distribution between two cyclic processes was caused by the connected-pore network and the available pore size distribution for each pore radius simulation step.

After the investigation of P_c–S_w–A_{awi} curves and obtaining 3D images of fluid-fluid distribution for both drainage and imbibition cycles, we simulated the water permeability tensor (hydraulic conductivity (K)) as a function of water saturation levels. The aim of this part of work was to establish a relationship of K–S_w curve in order to determine the overall effect on the water movement constrained by the pore space occupied by air. A numerical LB model scheme was used which solved the incompressible Newtonian water flow through the pore space. The simulations were done along the axial x-, y-, & z-directions. The K values exponentially increased with the increased S_w for both drainage and imbibition cycles. This indicated a strong non-linear relationship mainly caused by the inter-connected pore-water network on the main pore structure.

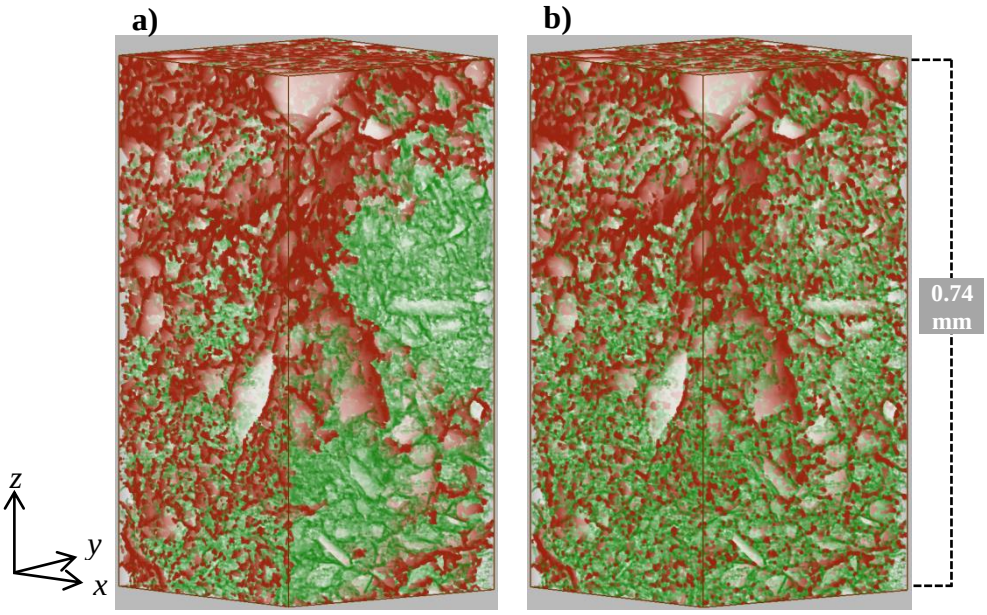

Fig. 10 3D visualization of a water saturation (S_w) sample, showing (a) the drainage process at S_w = 0.55, and (b) the imbibition process at S_w = 0.53. Air is shown in red and water in green, and areas occupied by the solid matrix are white.

The K values along the x-, y-directions were a little higher for the drainage process than for the imbibition process which showed a minimal hysteresis. Surprisingly, no such effect was seen along z-direction. The highest average axial velocity in all of the simulations along the x-, y-, and z-directions was $4.2 \cdot 10^{-7}$ m s^{-1} at S_w = 1.0, which is an evidence of a creeping flow throughout the porous model domain. Later, the results were compared with the well-known empirical predictions models of Brooks and Corey–Burdine, and Van Genuchten–Mualem. Both the models showed a good prediction with the simulation results, especially at higher water saturation level.

3.3 Biocolloid transport and retention in a variably saturated soil aggregate

The transport mechanisms of biocolloid (Escherichia coli) was studied in a saturated and unsaturated soil aggregate. Basically, the mass transport of solute or colloid is generally controlled by advection , and hydrodynamic dispersion which is the net result of diffusion and mechanical mixing in pore geometries. Advection which is the motion of the particles along the trajectories of the fluid streamlines whose velocity is governed by the hydraulic pressure gradient, porosity, and permeability

distribution. The mechanical dispersion refers to the spreading of a solute or colloid caused by differential fluid flow velocity field at the local pores. The difference in pressure gradients have minimal influence on the fluid flow streamlines in the complex pore network, but certainly affect the mass fluxes of colloid transport. Moreover, It is well-known that the trapping of air bubbles as a function of pore(s) radius effect the overall movement of water flow (see Section 3.2). The pore space occupied by air can deviate the colloid movement which affects transport parameters. Therefore, the main focus of this work was to analyze the overall effect of different pressure gradients, and the spatial distribution of air on the transport of E.coli determined by breakthrough curve (BTC) and retention time. Also, the transport of different biocolloidal sizes was also studied.

For pore scale fluid flow and transport modeling, the same material properties (texture, density) of soil aggregate was employed as discussed in Section 3.1 & 3.2. Due to the limited HPC capacity, 3D image of dimensions 500^3 voxels were extracted from the original image of 2048^3 voxels. A purely geometrical approach was adopted to intrude air (fitting spheres) into the pore volumes as the function of pore radius (image voxels). The geometrical approach considered both open and closed porosity. As a result, 3D image of two-phase (air-water) distribution was obtained. First, we established the water permeability (flow field distribution) at saturated and unsaturated water flow condition by imposing a pressure gradient of 1, 50, and 100 Pa. To do this job, lattice Boltzmann (LB) method was used to obtain flow parameter (permeability tensor) of porous media at varying flow conditions. A relationship between permeability tensor and water saturation, and the 3D visualization of flow simulation are depicted in Fig. 11. A non-linear relationship between water saturation and permeability tensor was observed (Fig. 11 d). For more details of water permeability in a variably saturated porous media, we refer to Section 3.2.After we established the velocity vector field at local pore scale, the E.coli was transported under saturated and unsaturated flow conditions. We utilized GeoDict software special module of "AddiDict" for transport modeling. The transport simulation time steps were set to 0.04, 0.09 and 5 seconds for the pressure gradient of 1, 50, and 100 Pascal, respectively. For all model simulations, the total particles transported per batch were 100,000. It is noted that the particles were injected at the center half plane of inlet boundary to observe hydrodynamic dispersion (Fig. 15 & 16).

The equation of mass transport of E.coli includes advective transport coupled with diffusivity is:

$$\frac{\partial C_s}{\partial t} = D_s \nabla^2 C_s - \mathbf{u} \nabla^2 C_s \qquad (9)$$

where C_s is the local mass distribution of the E.coli, $\mathbf{u}$ is the the local velocity vector, and D_s is the diffusivity due to Brownian motion.

In our transport modeling, the D_s is calculated as,

$$D_s = \frac{C\,k\,T}{3\pi\,\eta\,\rho\,r}, \tag{10}$$

where,

$$C = 1 + \frac{\lambda}{r}.\left(A_1 + A_2\, e^{\frac{-A_3\,2r}{\lambda}}\right) \tag{11}$$

with k, the Boltzmann constant ($1.38e^{-23}$ JK^{-1}), T is the temperature, η is the kinematic viscosity, ρ is the fluid density, r is the particle radius, λ is the mean free path, and C is the cunningham correction factor.

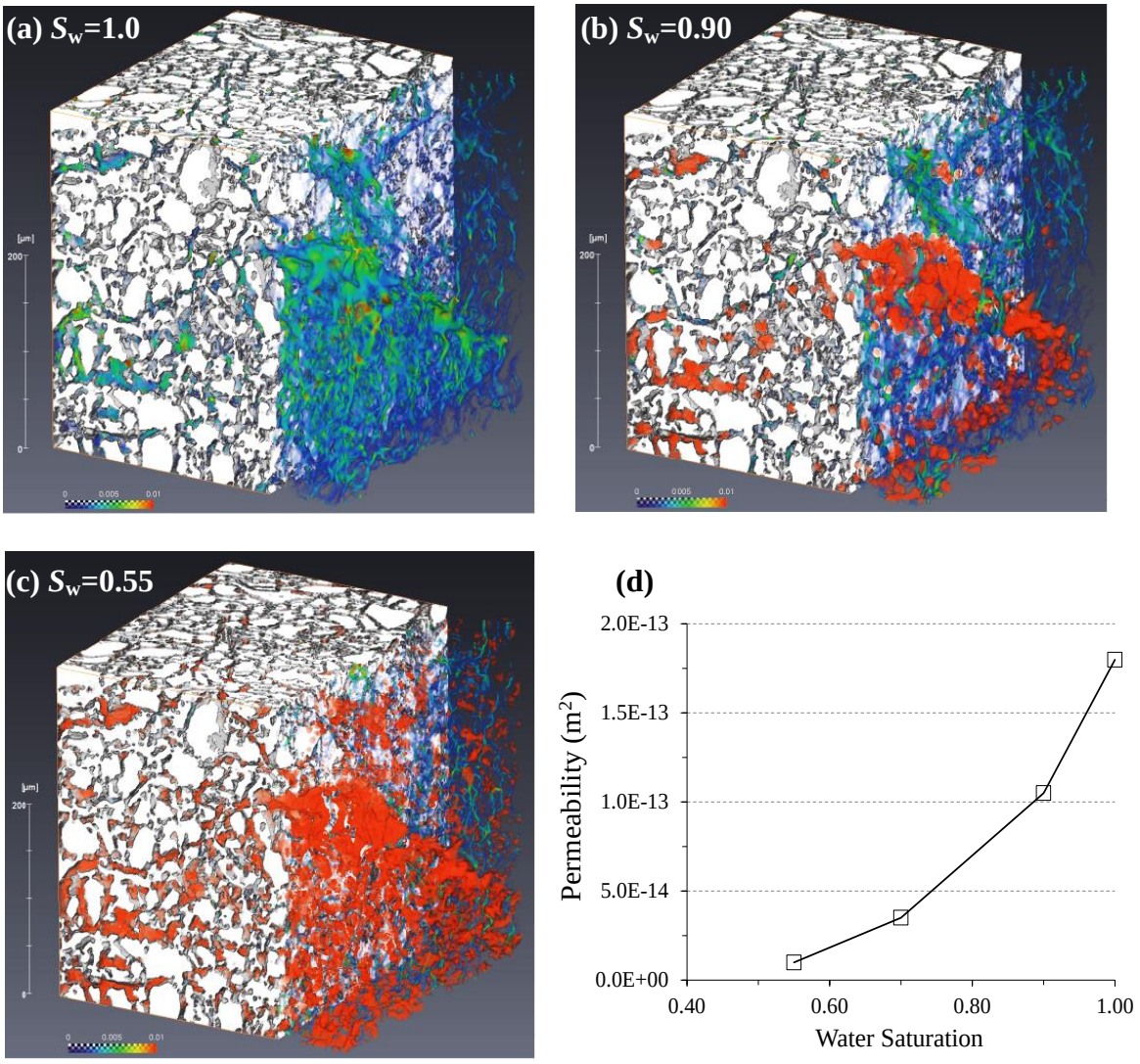

Fig. 11 3D imaging of a water saturation (S_w) sample . (a-c) Water simulation at S_w = 1.0, 0.90, and 0.55. Air is shown in red and water in green/blue, and areas occupied by the solid matrix are white. (d) Showing a simulated permeability value as a function of water saturation.

In the literature, the recommended E.coli particle diameters of 0.50μm and 1.2μm with particle density of 1080 kg m^{-3} were chosen for both saturated and unsaturated porous media. The particle transport is determined by breakthrough and retention curves. For the unsaturated water conditions, we presented the results only under pressure gradient of 100 Pa. We observed that the E.coli transport at moderate water saturation (S_w=0.55) had earlier breakthrough (BTC) as compared to higher water saturation (S_w=0.90, and 1.0) (Fig. 11a). This reflects the water flow movement and streamlines paths i.e., tortuosity constrained by air distribution at local pores. At S_w=1.0, the BTC was more asymmetrical and broader caused by dispersive flow mainly due to interconnected pore geometry and heterogeneity of the fluid velocity vector field.

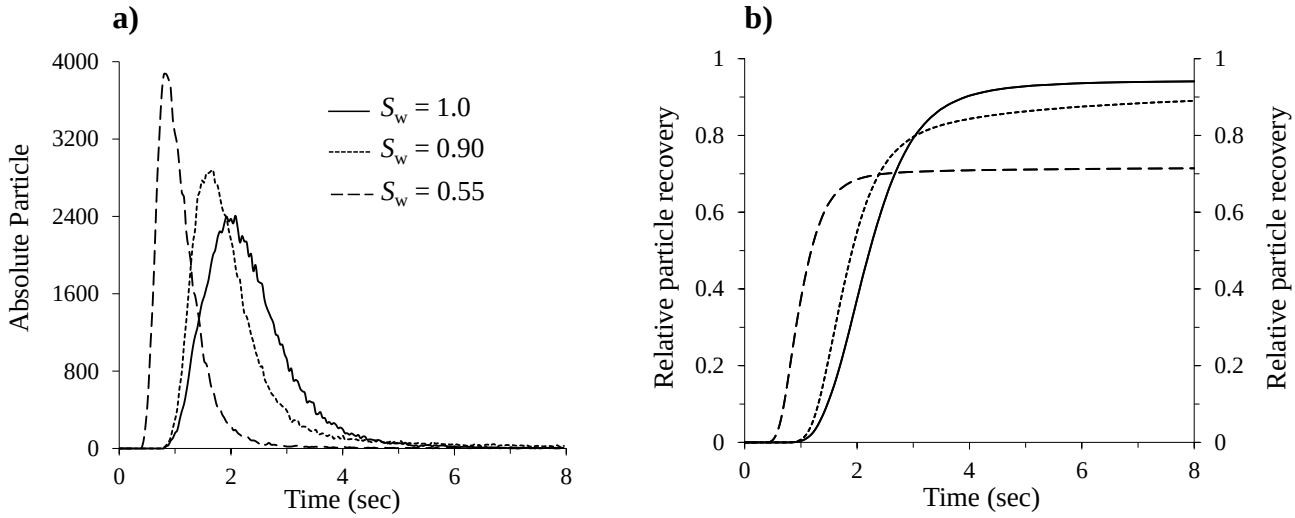

Fig. 12 Breakthrough curves at variably water saturation S_w imposing pressure gradient of 100 Pa. (a) Absolute particle distribution, (b) relative particle distribution. The solid lines, dot lines, and dash lines are at S_w=1.0, 0.90, and 0.55, respectively.

At the end of the simulation time of 8 seconds, the 95% of the total number of particles were recovered for S_w=1.0. The total particle recovery has decreased with the decreasing water saturation. The less particle recovery and long tailing of BTC at lower saturation i.e., S_w=0.55 indicated the air spatial distribution increased the particle residence time possibly due to dead-end pores. We, also evaluated the combined effect of E.coli colloidal sizes and pressure gradients (pore water velocities) on the transport at full water saturated condition. The transport of E.coli of diameter 0.50μm was compared to a diameter of 1.2μm under pressure gradient of 1, 50, and 100 Pa. At high gradients, small size particle had broader BTC distribution as compared to relatively large particle size (Fig. 12)

indicating that the transport of particles were not only due to flow dispersion at local flow velocity field, but also dominated by diffusion due to Brownian motion. Consequently, the flow dispersivity may agitate the particles into the region especially at solid boundaries where the water velocities are relatively very small. The diffusion due to Brownian motion increases the probability of transferring into the streamlines dominated by advection. The thus, the simulation results showed that the small particle size at high pressure gradients (50 Pa, 100 Pa) had less residence time but no big difference was observed at low pressure gradient (1 Pa). To understand and interpret the simulation results, the movements of two different biocolloidal sizes under full water saturation were tracked at pressure gradient of 100 Pa (see Fig. 13 & 14).

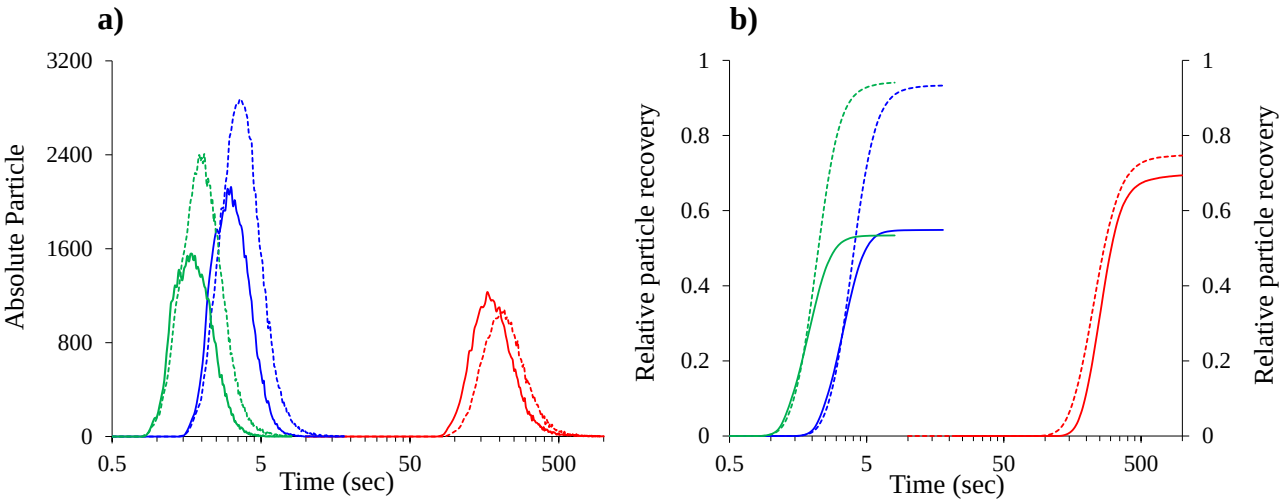

Fig. 13 Breakthrough and retention curves at full water saturation (a) Absolute particle distribution, (b) relative particle distribution. The red, blue, and green curves show the pressure gradients of 1 Pa, 50 Pa, and 100 Pa, respectively. The solid lines represent large colloid of diameter 1.2μm and dash lines represent small colloid of diameter 0.5μm.

3D visualization of E. coli particle tracking

A) Particle diameter =1.2 μm, Pressure gradient = 100 Pa

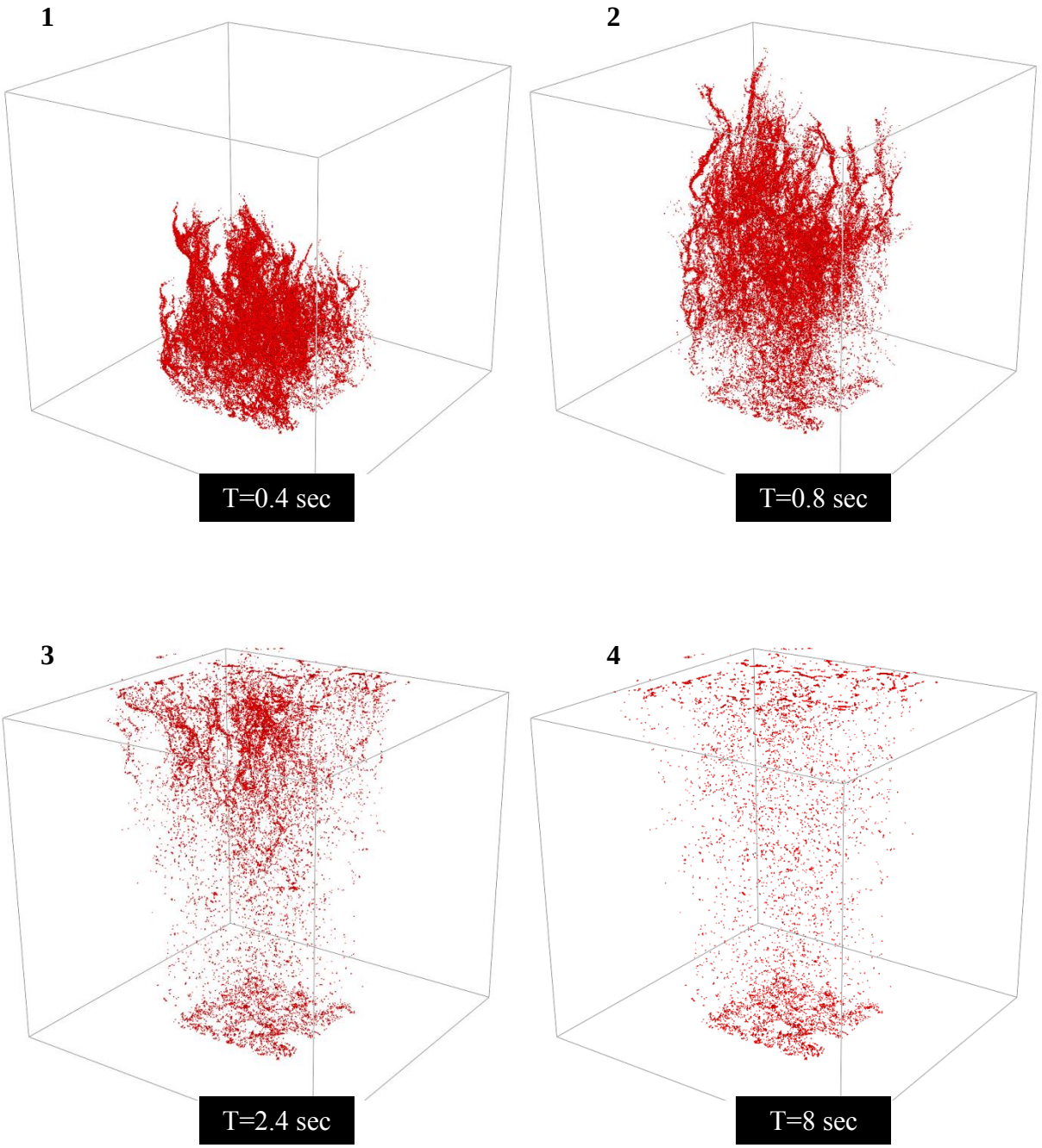

Fig. 14 3D visualization of biocolloid particle tracking and recovery at different simulation time steps. The particle diameter is 1.2 μm. The total numbers of particle injected in the system were 100,000.

B) Particle diameter =0.50 μm, Pressure gradient = 100 Pa

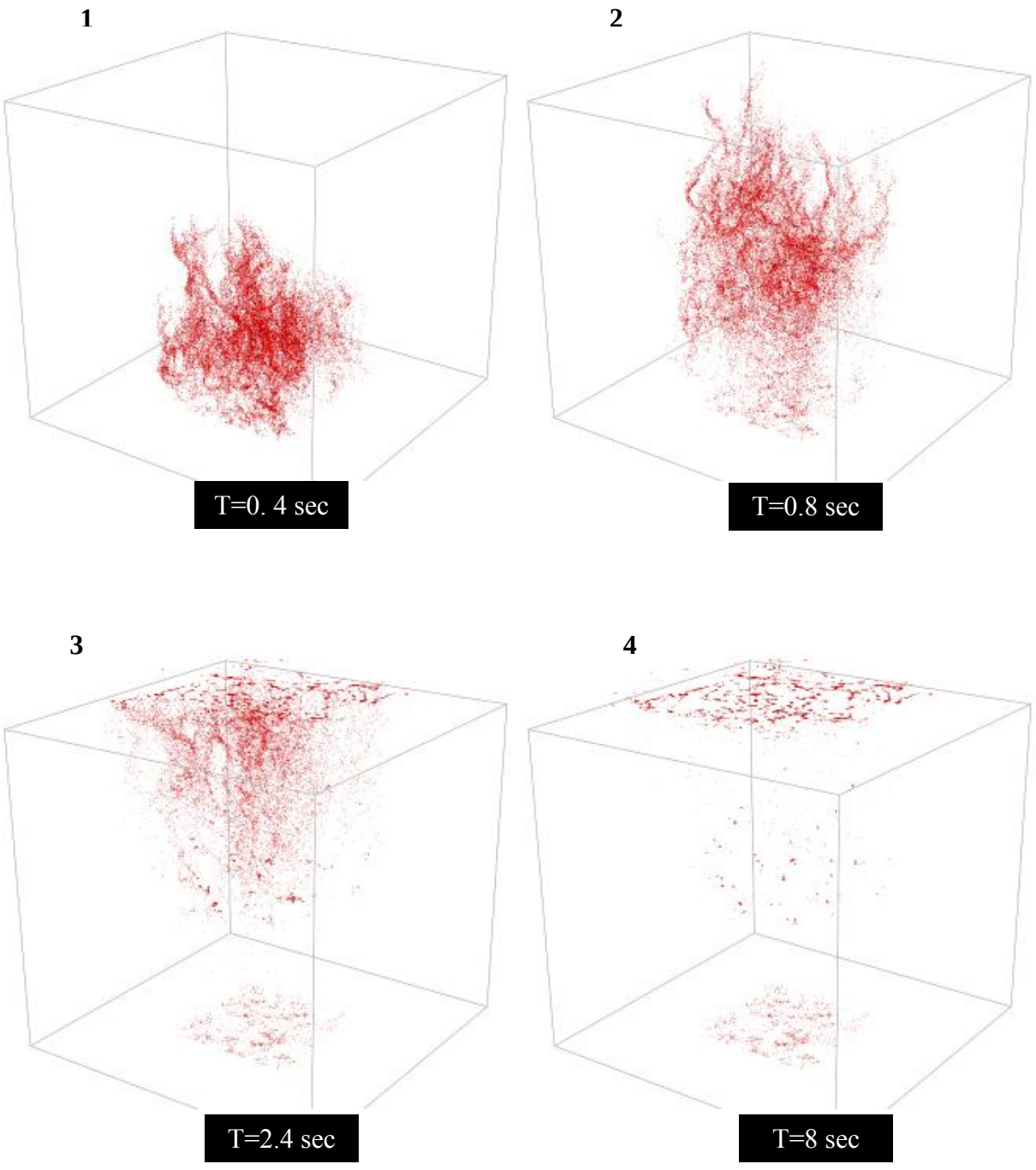

Fig. 15 3D visualization of biocolloid particle tracking and recovery at different simulation time steps. The particle diameter is 0.5 μm. The total numbers of particle injected in the system were 100,000

.

4 Conclusions

The main conclusions of the study are:

- In cylindrically shaped samples there is a simple correlation of beam-hardening of each phase on its position with its distance from the center of a rock core cylinder. This concludes that beam-hardening artefact is a radial function. Based on this relationship, each phase position in a sample can be extracted which allows a rigorous segmentation of the image. This method is more applicable to those samples in which one phase is particularly dominant, and uniformly distributed. In the case of heterogeneously distributed phases it is important to acquire several profiles of each phase to ensure that the values at all positions are extracted. However, the manual extraction of BH curves requires human judgment and experience.

- Due to the nature of the BH artefact, the same solid phases have lower attenuation values at the center of the sample than at the periphery. Consequently, the data values across the reconstructed grey values of image show a non-linear (parabolic) trend. Therefore, 2D polynomial of 2^{nd} order i.e., quadratic surface is fitted to the image in order to approximate the data. This polynomial approximation approach is constructing a surface that will best fit to the cloud of data points subject to the coefficient (parameters). A surface fitting to a low and high density multi-component geologic material may over, or underestimate the range of grey scale value of each individual phase, and subsequently will affect the segmentation outcomes.

- As an advanced classification technique, the least square support vector machine (kernel based learning method) is utilized to segment the data, with- and without beam-hardening correction, as a pixel-based classification task. Without dimensionality reduction or need of prior knowledge, the radial basis function kernel yields a good classification results on the beam-hardening corrected image showing a high performance accuracy rate but fails to classify the image with beam-hardening artefacts. It is important to extract all the possible range of grey scale value of each individual phase available for the training data set. The selection of each phase positions in a sample is also crucial to avoid overlapping phase's boundaries. Thus, the presence of noise and artefacts, data value selection, and the low amount of data of specific interest complicate the classification.

- The pore morphology based method is employed to simulate two immiscible fluids i.e., air and water displacements under drainage and imbibition processes in a complex soil pore volume structure. The method is also extended to incorporate residual water saturation and residual air saturation in drainage and imbibition cycles, respectively. The establishment of non-linear curves of capillary pressure as a function of water saturation shows the hysteresis which has been ascribed to the irregularity of the pore space geometry, and pore size distribution. In a pore-morphology based method the very complex P_c function is calculated from the direct quantification of saturation distribution alone using the Young–Laplace equation. It is well argued in the literature that the non-uniqueness in the relationship of capillary pressure and water saturation is also related to the absence of important variable fluid-fluid interfacial area.

- Fluid-fluid interfacial plays a vital role in many subsurface multiphase flow and transport processes. Therefore, air-water interfacial area as a function of water saturation from static distributions of fluids is quantified for both drainage and imbibition simulations. By visual inspection of both simulated images, the air-water phases were uniformly distributed in the imbibition process more so than in the drainage process, especially at moderate water saturation levels. The difference in the interfacial area were caused by the available pore size distribution and pore geometry, where connectivity is taken into account for each pore radius simulation step induced by a pore morphology based method. Because of the simple pore morphology approach of fitting spheres in a pore space to quantify the fluids distribution, the higher interfacial area of imbibition curves than drainage curves do not agree with the experimental studies following the fundamental fluid physics of the receding and advancing phenomena (contact angle) and local capillarity surface tension.

- A fully parallelized lattice Boltzmann solver is employed to simulate water permeability tensor (hydraulic conductivity) in both saturated and unsaturated complex soil structure. The variation in the obtained saturated hydraulic conductivity values of three independent region-of-interests is rather in moderate range. We also observed that the presence of macrospore (preferential) flow overestimate the simulated results. In an unsaturated medium, the visualization of the simulation results showed that spatial distribution of air blobs hampered the movement of water at different water saturation levels. The non-linear curve of hydraulic conductivity which is increased with the increasing water saturation levels for both drainage and imbibition cycles are observed, but have the minimal hysteresis. This non-linearity is mainly caused by the dependency of the inter-

connected pore-water structure (pore throat) on the main pore network. We observed that at the same water saturation levels of drainage and imbibition process, the water flow velocity at the pore scale associated with the available pore size distribution has a minor influence on the macro-scale constitutive parameter of hydraulic conductivity.

- Breakthrough curves are extensively used to characterize the physicochemical processes involved in the transport of solutes in porous media, here soil aggregate. In the previous studies it is well-determined that the trapping of air bubbles as a function of pore(s) radius effect the overall movement of water flow, and consequently affect the transport parameters. In an unsaturated porous media, the biocolloid (E.coli) transport at moderate water saturation had earlier breakthrough as compared to higher or full water saturation levels. Also, the particle residence time has increased with the decreased in water saturation. This reflects the particle transport driven by water flow along the streamlines paths (tortuosity) constrained by air distribution at local pores. The breakthrough curves were more asymmetrical and broad, caused by dispersive flow mainly due to interconnected pore geometry and heterogeneity. We observed that the particle residence time is also a function of pressure gradient; larger gradients (flow velocities at local pore scale) result in wider differences in residence time between particle of different sizes. Moreover, we observed that the particle velocities were 2-3 times higher than the average water flow velocities.

5 Future perspectives

For objects of non-cylindrical shape, the beam-hardening is no more a radial function and changes for each angle. Therefore, an efficient mathematical calculation is required to extract beam-hardening information regardless of sample shape and X-ray beam geometry i.e., cone beam. The Least square support vector machine is capable of dealing with complex nonlinear classification problems. The feature extraction which include both shape-related features (texture) and window-based features (statistical) is the important process of locating information of interest to detect for instance pore space in soil images. The performance of a classifier based on other kernel functions like linear, polynomial, multilayer perceptron, results will be compared with other techniques i.e., K-Nearest Neighbor classifier and artificial neural approaches.

The phase distribution at the pore-scale is controlled by the capillary forces depending on pore size, pores connectivity, surface tension, and wettability. The latter, is of great importance in defining the flow characteristics. Therefore, for the analysis macroscopic properties of capillary pressure and permeability tensor in drainage and imbibition processes, the future work requires to integrate local capillarity surface tension, and the advancing and receding contact angles phenomena. In this research, the LB simulations of single phase flow in an unsaturated medium, fluid-fluid and fluid-solid interactions were treated as “no-slip” boundary conditions. In case of fluid-fluid density difference, the integration of the slip boundary condition is of major importance which may lead to significant errors, especially at lower water saturation levels.

Biocolloid are affected by random particles interactions result in Brownian movements. The biocolloid can attach to fluid-solid interface and the fluid-fluid interface. The attachment is considered the main controlling factor to understand the mechanisms of the colloid retention. Therefore, it is important to integrate van der Waals force and the electrostatic effects of surface charge and particle charge in biocolloid transport modeling.

Paper I

J Soils Sediments (2012) 12:86–96
DOI 10.1007/s11368-011-0435-3

3D simulation of the permeability tensor in a soil aggregate on basis of nanotomographic imaging and LBE solver

Faisal Khan · Frieder Enzmann · Michael Kersten · Andreas Wiegmann · Konrad Steiner

Received: 11 May 2011 / Accepted: 28 September 2011 / Published online: 15 October 2011

Abstract
Purpose The purpose of this hydropedological work is to investigate the feasibility of a method to calculate permeability of soil peds on the matrix pore scale resolution. This paper focuses on imaging of the intra-aggregate microstructure and, based on the three-dimensional (3D) images, quantification of the pore network connectivity and permeability tensor. Finally, lattice Boltzmann equation (LBE) simulations of Navier–Stokes flow in the thus derived pore network allow to compute the heterogeneous 3D flow velocity field.
Materials and methods Nanotomographic X-ray absorption mode imaging of a single soil ped has been performed at the TOMCAT beamline of the Swiss Light Source synchrotron facility with 0.74 μm spatial resolution. Segmentation of the 3D Nano-CT images into solid phase and pore space allowed to study the statistical properties of the connected pore network. The thus derived pore network data were used as direct input for the software package GeoDict integrated with a LBE algorithm to perform saturated water flow modeling.
Results and discussion The soil ped features quantified from the tomographic images were pore and grain size distributions (PSD, GSD), porosity, percolation tensor in *x*, *y*, *z*-direction and percolation pathways (macropores). The PSD frequency has a peak in the range 3–8 μm (mesopores) contributing 50% of the total. In general, the matrix pore structure and, hence, saturated flow field velocity of our sample is highly anisotropic. LBE-simulated pore scale fluid flow is used to ultimately determine gross parameters (coefficients) of Darcy's law such as the saturated hydraulic conductivity, K_s. The thus simulated $K_s = 105 \pm 24$ cm day^{-1} of a single soil ped (mean of three ROIs and directions) is one order of magnitude higher than the value of $K_s = 12 \pm 2$ cm day^{-1} predicted by a classical pedotranfer function approach. This K_s underestimation by PTF is typical for macropore flow.
Conclusions Integration of 3D image evaluation with the LBE approach as an essential step toward understanding the highly heterogeneous intra-aggregate microstructure is now possible on the submicron scale. Modeling the resulting anisotropic fluid advection field is, however, just a first step for 3D models of biogeochemical reactions at soil interfaces on this pore scale.

Keywords Lattice Boltzmann · Pedotransfer functions · Permeability tensor · Pore-scale modeling · Pore size distributions · Synchrotron tomography

Abbreviations

FFT	Fast Fourier transform
HPC	High-performance computing
LBE	Lattice Boltzmann equation
nano-CT	X-ray computed nano-tomography
PSD	Pore size distribution
PTF	Pedotransfer functions

1 Introduction

Transport of soil water affects solute dissipation, defines rates of microbiological processes in the rhizosphere and water supply to plants, governs transpiration and groundwater replenishment, and has many other important

F. Khan · F. Enzmann · M. Kersten (✉)
Earth Systems Research Center, Institute of Geosciences,
Johannes Gutenberg University,
55099 Mainz, Germany
e-mail: kersten@uni-mainz.de

A. Wiegmann · K. Steiner
Fraunhofer-ITWM,
Fraunhofer-Platz 1,
67663 Kaiserslautern, Germany

functions in the soil environment. The dynamics of fluid flow and transport processes is associated directly to the microstructure and pore space geometry of soils. Therefore, quantitative geometric information of the microstructure, such as pore size distribution (PSD), total porosity, pore network connectivity, and interfacial properties, is imperative to understand and model the complex fluid flow in soil. Kutilek and Nielsen (2007) recommended a combination of advanced hydrological and micropedological approaches which could lead to a better understanding of the real pore and water properties in soil. Water retention curves are commonly calculated on the basis of pedotransfer functions (PTFs), e.g., for soil composed of different aggregate size fractions (Guber et al. 2004). Development of reliable fluid flow models became possible only in the last decade by introduction of computer-assisted, nondestructive imaging techniques such as computer microtomography (μCT). In the μCT technique, the three-dimensional (3D) spatial distribution of X-ray absorption coefficient is measured, which closely correlates with the local density distribution. Due to recent advancements in high-performance computing (HPC) technology, this μCT imaging technique has made a major breakthrough in micropedology providing for a more advance microstructure analysis by numerical simulation (Peth 2010). Due to the complex heterogeneous and anisotropic distribution of water in porous media like soils at field capacity, the importance of 3D high-resolution imaging and image processing cannot be underestimated (Tippkötter et al. 2009; San José Martínez et al. 2010).

Synchrotron-based μCT has been introduced for an effective visualization of the morphological features of the pore-space network at a voxel resolution down to microns (Carminati et al. 2007; Kaestner et al. 2008; Peth et al. 2008). Recent developments in the experimental and analytical techniques in synchrotron radiation μCT have greatly facilitated quantitative description of the geometrical features of even the non-matrix pore space (Peth 2010). Moreover, pore-scale modeling provides a way for the better understanding and effective parameterization of macroscopic fluid flow for a success with simulation tools. Using μCT geometrical datasets, an increasing number of investigations of (multi-phase) fluid flow at the (yet non-matrix) pore scale level have been published in the last few years (Wildenschild et al. 2005; Culligan et al. 2006; Fourie et al. 2007; Pfrang et al. 2007; Porter and Wildenschild 2010; Silin et al. 2011). Meanwhile, spatial resolution in synchrotron-based tomography has improved to submicron voxel resolution (nano-CT). This capability opens up imaging of the full complexity of even the matrix pore-scale geometry, but demands also for more effective numerical methods that are crucial for a reliable quantitative evaluation of the capillary flow and transport processes. For modeling of flow and transport from first principles on the matrix pore-scale, the novel powerful lattice Boltzmann equation (LBE) simulation technique have received most attention in recent years. The popularity of the LBE method is due to its simple formulation and application to flow problems (both single- and multi-phase flow) in complex pore geometries, but is challenging in terms of sample space which may demand for expensive parallel processing HPC systems. Validity of this method has been shown for different investigation purposes involving soil and aquifer samples to quantify, e.g., non-aqueous phase liquid (NAPL) dispersion (Knutson et al. 2001), 3D isothermal flow (Inamuro et al. 1999), solute transport in variably saturated porous media (Zhang et al. 2002), and 3D simulations of biofilm growth in porous media (Graf von der Schulenburg et al. 2009).

The purpose of this work is to image and simulate the heterogeneous fluid velocity field in the matrix pore space of a (at first approximation water saturated) soil aggregate by applying the LBE solver to its X-ray computed nano-CT image as geometrical data input. Advanced 3D image analysis to quantify the pore nanostructure is an essential first processing step. We will show how this may lead to the 3D physical parameter space, such as the permeability tensor in the matrix pore space of soil peds.

2 Materials and methods

2.1 Materials

The soil was sampled from the 28 cm deep Ap horizon (sample "Ap18," middle topsoil 10–18 cm) of a Luvisol at experimental research farm Scheyern in July 2010 after rainfall followed by drainage. This farm is located to the north of Munich, Germany (48°30′N, 11°21′E). The soil is characterized as a Luvisol according to the World Reference Base for Soil Resources 2006 that developed from weathered loess and is under agricultural use. The soil structure is friable and consists of strong and approximately spherical fine and medium (1–5 mm sized) granular peds. The fine earth (mineral content <2 mm, only 1.5 wt.-% rock fragments) is characterized as medium-textured loam (FAO class "Medium", UK soil type "SaSiLo," USDA and ISSS soil type "SiLo," German soil type "Slu"), with 40 wt.-% sand, 45 wt.-% silt, and 15 wt.-% clay fraction. The soil color (Munsell notation) is characterized as 10YR 4/4 (non-reducing), with a soil dry bulk density ρ_t=1.50±0.04 g cm^{-3}, a pH_{CaCl2}=5.3, a total C_{org}=13.6 mg g^{-1}, and a total N=1.32 mg g^{-1} (C/N=10.3). The soil sample was in a moderately moist state and chilled by dropping into liquid nitrogen to avoid soil structure disturbance by faunal activity and kept frozen (−20°C) until analysis. The gravimetric water content of medium-sized ped subsamples (n=5) was determined upon

drying in an oven at 105°C overnight which gave a water mass of 21±2 wt.-%.

2.2 Synchrotron-based nano-CT experiment

The synchrotron-based nano-CT was performed at the Tomographic Microscopy and Coherent Radiology Experiments (TOMCAT) beamline of the Swiss Light Source (SLS) at the Paul-Scherrer-Institute in Villigen, Switzerland. Tremendous efforts have been made at this beamline in recent years to apply X-ray absorption based tomography on low-contrast environmental samples by "edge-enhanced" (Stampanoni et al. 2006) and "phase-contrast" (Bronnikov 2002) techniques. These new techniques enable the user community to fully apply this unique beamline on samples full of organic matter and other biogenic materials low in X-ray attenuation (McDonald et al. 2011). Details of the beamline setup have been published by Marone et al. (2009) and will not be repeated here. Prior to the measurements, all tools and instruments were fixed by help of the beamline technical staff. A single soil ped of about 2 mm in diameter was trapped in the center of the conical sample holder boring (Murshed et al. 2008). It was cooled at freezing temperature (200 K) by cryojet equipment (Cyrojet-XL, Oxford, UK) to keep the sample structure fixed during rotating at projection angles between 0 and 180°. The angle viewing step size was set at 0.12° degree intervals yielding in a total of 1,501 projections, and the sample was imaged using an X-ray beam at energy of 20 keV. After penetration of the sample, the X-rays were converted into visible light by a Ce-doped YAG scintillator screen (Crismatec, France). Projection images were further magnified optically (20×) and digitized by a high-resolution (2,048×2,048 pixels) ultra-fast read-out CCD camera (PCO 2000, Germany) with exposure times of 140 ms. This set-up resulted in a field-of-view of 1.5×1.5 mm^2 and an original resolution of 0.37 μm. The latter was binned 2× "on-chip" to improve the signal-to-noise ratio yielding in an effective spatial resolution of 0.74 μm. An important prerequisite for reliable data quality control is the option of fast acquisition and reconstruction of data "on the fly", which enables adopting the desired resolution, number of projections, sample exposure time at the beamline and the total processed file size within the rather limited beam time acquired for the experiments. The reconstruction of the complete dataset of >1 TB was performed by a fast combined wavelet-fast Fourier transform (FFT) decomposition and gridding procedure on a 16-node Linux cluster within few minutes after data collection. An ad hoc padding of the sinograms prior to reconstruction significantly reduces typical artifacts related to data incompleteness, making local tomography a valuable acquisition mode when small volumes in relatively large samples are of interest (Marone et al. 2010). After raw data collection, the AMIRA/AVIZO software package is applied to render immediately the result and evaluate the image quality.

2.3 Image processing

After the 3D reconstruction of sample raw data ($2{,}048^3$ voxels) and data conversion to 16-bit images, further processing steps include noise filtering, discontinuity detection, and thresholding. Filtering is warranted because grey-scale images from CT comprise a certain level of noise, the reduction of which has an immense effect on the quality of the subsequent segmentation. Edge-preserving filters are of particular help for such smoothing of the raw data (Sheppard et al. 2004). The median filter technique used is a nonlinear anisotropic digital filter specified by different kernel window sizes and dimensions (1D, 2D, and 3D; Gallagher and Wise 1981). The median filter replaces a pixel by the median of all defined window size pixels in the neighborhood. We applied the 3D median filter technique with window size masking (3×3×3 in 3D) to smooth the volume voxel dataset. For any 3D imaging and modeling on such high-resolution dataset with limited computing resources, it is always desirable to select a region-of-interest (ROI) spatial domain that can at best be representative of the whole sample as shown in Fig. 1. Since

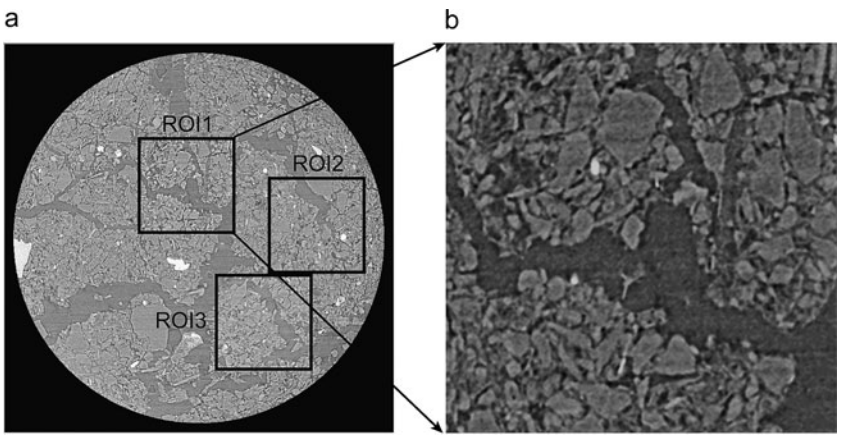

Fig. 1 Example of ROI #1 extraction, with **a** the original image ($2{,}048^3$ voxels) with different ROIs location, and **b** the ROI #1 image ultimately selected (500×500×1,000 voxels). Note that one voxel has an edge length of 0.74 μm

variability of the ROIs is not a priori known, three different ROIs of size 500×500×1,000 voxels each were extracted from the original sample by the AMIRA software to evaluate reproducibility of the approach.

Once image filtering and the extraction of a representative ROI is accomplished, the image segmentation process is the next step that is required to select features of interest in the X-ray radiographs. Segmentation involves in the present case the conversion of each voxel grey scale value into a binary image that classify between void and solid. Baveye et al. (2010) presented recently a thorough study on the bias introduced by the variability of different segmentation approaches. In grey level thresholding, the most commonly applied method is to choose a global (single) threshold value for the entire image (Pal and Pal 1993). This segmentation technique is well suited in case of a bimodal distribution where the histogram of the grey level range is separated by one local minimum. Unfortunately, in our case, the minimum is just above the height of half-maximum of both signal peaks for solid and void (Fig. 2) which is due to a considerable number of voxels overlapping boundary edges. However, based on the local minimum threshold value by visually defining the minimum of the image intensity value for the entire 3D dataset (see Fig. 2), the boundary voxels are equally partitioned into full void or solid voxels. This is justified because of the use of monochromatic synchrotron radiation, where the absorption coefficient for each voxel remains the same independent of the projection angle and hence propagation pathway to that voxel through the sample (Rennert et al. 2011). This simple approach enabled us to convert the whole raw grey-scale image into a reliable binary black-and-white image representing voids and solids as shown in Fig. 3b. In such segmented images, pore space is ultimately represented by white pixels, and the solid matrix is represented by black pixels. Clearly, in nano-CT soil imaging without phase contrast enhancement (Bronnikov 2002), the contrast between the various solid phases is too low and cannot be segregated. Moreover, the mineral and organic phases are to a degree intertwined, which cannot be resolved at the current tomographic resolution. However, based on only the edge enhancement effect, binarizing between solid and voids was quite feasible.

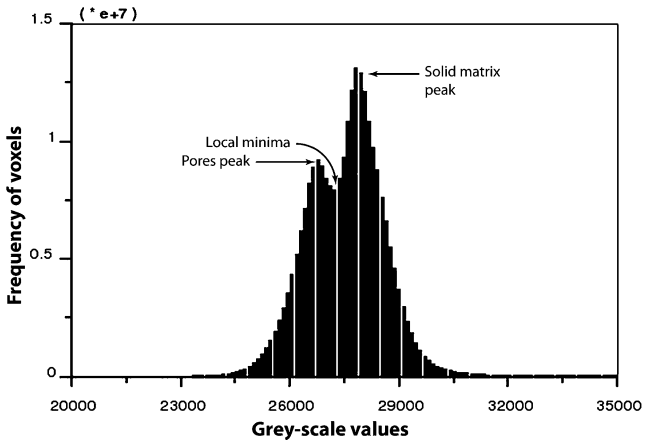

Fig. 2 Sample grey-scale values histogram for the entire 3D dataset

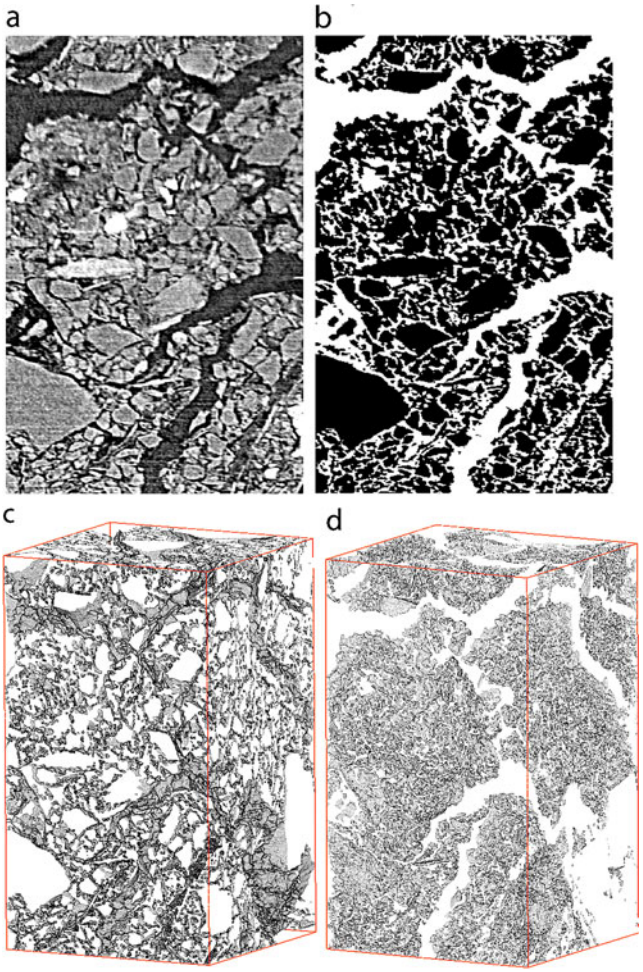

Fig. 3 Segmentation process and volume rendering, with **a** the original image 2D slice (*xz* plane), **b** the resulting segmented 2D image, **c** the 3D volume rendering of all 2D images where light voxels represent the solid matrix distribution in the ROI #1 (500×500×1,000 voxels), and **d** an inversed 3D image where the light pixels represent now the pore network as an ultimate result of segmentation. Soil sample height is 0.74 mm (=1,000 voxels)

For the next step, volume rendering is the method used for visualizing 3D volume data from the two-dimensional (2D) slices. The entire image volume, or a portion of which defined as ROIs, can be used to create a volume rendering. This data output method is based on several visualization techniques as has been extensively discussed by Calboun et al. (1999). In the volume-rendering process, several rendering parameters including window width and level, color map, opacity, brightness, percentage classification, and image display

are optimized. Figure 3c, d shows the volumetric rendering results for the soil aggregate sample.

3 Results and discussions

3.1 Estimation of 3D pore-scale geometry

With the 3D images accomplished, the crucial step is to determine pore network physical properties of the soil ROI sample. To perform this job, we applied the GeoDict software package on the 16-bit segmented 3D image, which allows us to directly map the pore structure and provide us for a more detailed analysis of the microstructure. The GeoDict software package computes, in general, predictions of physical material properties on basis of real (i.e., tomographic) microstructures (Pfrang et al. 2007; http://www.geodict.com/). The bin size chosen corresponds to the effective image resolution (0.74 μm) which means all voxels along all three x, y, z-directions of the chosen ROI (2.5×10^8 in total) are brought into account for the calculation. The PoroDict module of GeoDict was used to determine various geometrical gross parameters from the CT data such as pore diameter frequency distribution, open porosity (connected), specific surface area, and percolation paths. Geometrical PSDs were determined by fitting spheres into the pore volumes. While the purely geometrical approach considers both open and closed porosity, mercury intrusion porosimetry (MIP) is simulated by the virtual intrusion of a non-wetting liquid (mercury) into the open porosity only. The mercury is forced into the porous media while applying pressure that is related to the diameter of the pores accessible to the non-wetting liquid. Bartoli et al. (1999) explain how this can be determined in relation with the liquid surface tension and contact angle. They compared MIP with other methods of soil structural characterization and ascertained that mercury intrusion is mainly controlled by the connectivity of the pore space distribution (i.e., the pores only contribute to the pore volume fraction if connected to the non-wetting phase reservoir). Figure 4 depicts the trend lines of cumulative and volume fraction percentages for the ROI #1 as an example for both MIP and geometrical approaches. Clearly, any pores <0.74 μm are not accounted for, because the simulation is set to iterate by voxel size (0.74 μm). For both the geometrical and MIP approaches, the output results are slightly different but yet yield the same maximum diameter (ϕ) at the 100% cumulative amounts to 85 μm, while the pore volume fraction distribution, has a peak in the range of 2–8 μm in diameter. This indicates that 50% of cumulative pore size, the median pore diameter D50, is less than 8 μm (mesopores size range), i.e., 10% of the maximum diameter only. The volume fraction frequency sharply drops to less

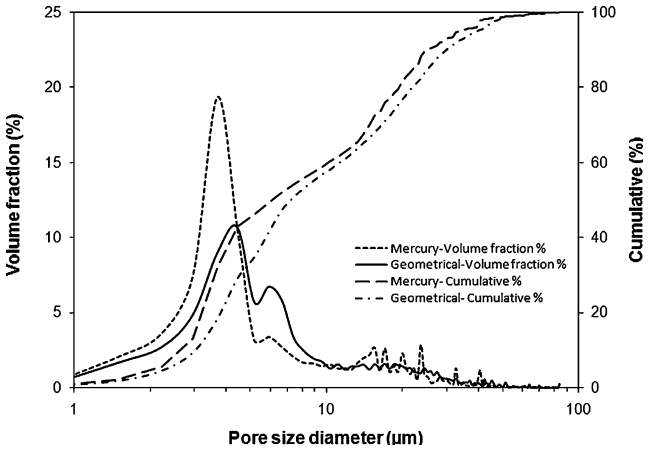

Fig. 4 PSD of sample ROI #1 on a log10 scale: the pore volume and cumulative fraction (%) are plotted for both MIP and geometrical simulation represented by different trend lines

than 3% at pore diameters larger than 8 μm, albeit 50% of the pores have diameters ranging from 8 to 85 μm. Likewise, to recognize the micro- and macropore contribution to the total pore volume, the median pore diameters of D10 and D90 are computed by geometrical simulation approach, which represent 10% and 90% of the pores diameter cumulative, respectively, and establishes the PSDs ranging from finer to coarser. Table 1 summarizes the porous media properties for the soil aggregate. The 3D images of the volume PSD (D10, D50, and D90 of ROI #1) determined by MIP simulation are shown in Fig. 5a–d. Similarly, the inverted image data structure gives a solid particle grain size distribution (GSD) of L10, L50, and L90 in the whole ROI volume (see Table 1). Estimation of the specific surface area, however, is not based on simply adding up the voxel surfaces but on a Poisson line process, i.e, the count of surface crossings along rays in all directions (Pfrang et al. 2007). This algorithm is convergent and consistent for isotropic media (i.e., no preferred surface orientation), but is slightly biased in case of highly anisotropic media like pure clay.

All pores in the whole network are well interconnected, because for both total and open porosity, the PoroDict code yields in nearly the same value. The average porosity Φ=0.40± 0.01 cm^3 cm^{-3} is typical for a soil characterized as loam. Percolation path modeling is used to determine connectivity in the pore microstructure. Figure 6 depicts a bundle of ten such percolating capillary pathways along z-direction connecting open pores with diameter sizes ranging from 4 to 9 μm in the ROI #1. This feature is a clear indication of an anisotropic soil aggregate media and can be extended to understand the fluid flow movement in our soil sample as detailed in the next section. From the geometrical characterization including the inner specific surface (see Table 1), it appears that our ped sample is highly porous, heterogeneous,

Table 1 Estimation of 3D geometrical parameters of the soil aggregate sample (mean ± SD for 3 ROIs)

ROI #	Pore size distribution (PSD), µm			Total porosity, cm^3 cm^{-3}	Grain size distribution (GSD), µm			Specific surface area (*S*), m^2 g^{-1}
	D10	D50	D90		L10	L50	L90	
1	3.0	7.3	30.0	0.390	4.4	10.7	59.1	0.11
2	3.0	8.6	32.8	0.406	4.4	9.0	17.5	0.11
3	3.0	6.5	33.6	0.408	4.1	9.2	31.8	0.12
Mean±SD	3.0±0.0	7.6±0.9	32.2±1.5	0.401±0.008	4.3±0.1	9.7±0.8	44±17	0.11±0.01

and anisotropic as expected of a natural soil aggregate. From these geometrical data, some gross parameters may be calculated characterizing the state of the soil water in the peds. This is of interest since the water regime cannot be defined by suction tests with single soil peds.

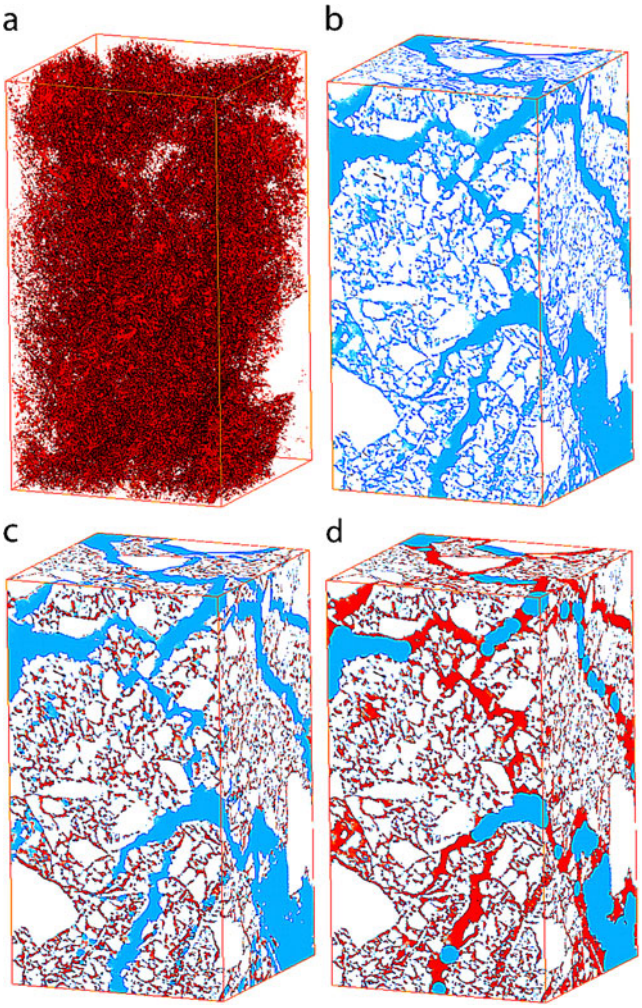

Fig. 5 3D imaging of soil sample ROI #1 porosimetry, with **a** pore size of D10 (without solid matrix which is not clearly discernible when integrated with the void network), **b** same with solid matrix representation. *Blue color* represents mercury distribution in pores, while *red color* depicts pores size; **c** and **d** represent the same images for D50 and D90 PSD, respectively. Soil sample height is 0.74 mm (=1,000 voxels)

3.2 Evaluation of matrix fluid flow in soil aggregates at the pore scale

In the next step, permeability is to be simulated by numerically solving incompressible creeping Newtonian flow through the 3D pore space obtained by nano-CT. In the present work, this simulation is based on solving the discrete Boltzmann equation instead of the standard continuum flow equations. Lattice Boltzmann models (LBM) can be used on a number of different lattices shapes, both cubic and triangular. Standard LBMs involves an explicit time iteration scheme with a constant time step, uniform grid, and local data dependencies, and are ideal for parallel computing (Succi 2001). The most straightforward method for numerical grid generation is a regular cubic lattice based on the tomographic image itself. The unit cell of the LBM grid thus equals the cubic voxel of the digital nano-CT image. In the present work, the "D3Q15" implementation of LBM with the multiple relaxation time (MRT) approximation of the Boltzmann equation is used, which represents a 15 vector of velocity space around the center points of the cubic unit cells. Humières et al. (2002) demonstrated the benefits of using such a MRT–LB approach and its numerical stability over the classical lattice Bhatnagar–Gross–Krook (BGK) equation. A simple and straightforward "no-slip" velocity boundary condition on the fluid–solid interface is applied which obeys a multi-

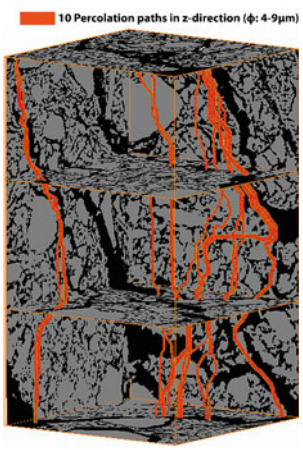

Fig. 6 3D image of main percolation pathway traces (macropores) along *z*-direction of ROI #1. Soil sample height is 0.74 mm (=1,000 voxels)

reflection bounce-back rule (Ginzburg and d'Humiéres 2003). The quality and accuracy of this widely used approach has been discussed previously in the related literature (e.g., Pan et al. 2006). For the flow simulations, the fully parallelized single-phase LBE solver in GeoDict was used, which was developed for both single- and multi-phase flow (Ginzburg and Steiner 2003, Thoemmes et al. 2009). The simulations were run on a 16-core, 64-bit SUN workstation with 64 GB of RAM. With this HPC workstation, it took less than 2 h to compute four unknowns for our model space, which are the three velocity components and the pressure gradient in the space spanned by all 2.5×10^8 individual nano-voxels of 0.74 μm^3 size. Clearly, the boundary of the flow domain (i.e., the pore space) is in this case known only to the accuracy of the tomographic image. Numerical accuracy and maximum number of iterations for our model are set to 0.0005 and 10,000, respectively. To regulate a flow regime, a constant pressure drop of 35 Pa is imposed between inlet and outlet boundaries of the model system. To achieve a unique LBE solution, a fluid density of ρ=998 kg m^{-3} and viscous friction with a fluid viscosity of μ=1 $g m^{-1} s^{-1}$ are applied as input flow parameters in the model space assumed as fully saturated (i.e., all pores filled with water). Note that for all simulated results, the boundary conditions are dealt as periodic in all computational dimensions, i.e., all six grid faces. This implies, with a periodic boundary condition for each streamwise directions, that the outgoing particle populations at one end of the lattice become incoming populations at the other end with no constraint on macroscopic velocity or density. As depicted in Fig. 7, the flow is driven by a linear pressure gradient which results in the mean flow direction of the pressure field from bottom to top along *z*-direction. A pressure gradient at local porosity determines ultimately the fluid velocity vector field. In principle, it is feasible to make animations of the fluid velocity field developing upon injection of a tracer. For this paper, Figure 8 shows a velocity field blueprint along *z*-direction resulting from a steady-state velocity vector field. The latter condition is reached when a pressure gradient at local porosity remains unchanged, at which the numerical simulation is converged and the model iteration run terminates to proceed further on.

Figure 9 presents the velocity field stream fluxes along *z*-direction. The variation of different colors with an arrow point indicates the flow velocity magnitude in the 3D porous soil aggregate media. The color code depicts that the majority of the velocity field is in range from very low (blue color, ≈0 m/s) to moderate (green color, $\approx2\times10^{-3}$ m/s) magnitude. This is to be expected as the soil is a heterogeneous anisotropic medium. In an anisotropic medium, a hydrodynamic parameter matrix calculated in a 3D Cartesian coordinate system (i.e., permeability tensor of 3×3) is needed, which can be calculated from the velocity vector field and pressure difference. Permeability is the measure of understanding the ability of porous media to conduct flow which is in effect the coefficient in Darcy's law for porous media. The flow permeability coefficient, *k*, is generally a tensor-valued measure of the ability of a porous medium to transmit fluids. It is defined for relatively slow, steady-state, isothermal, Newtonian fluid flow through porous media by Darcy's law. The permeability tensor is therefore determined at the scale

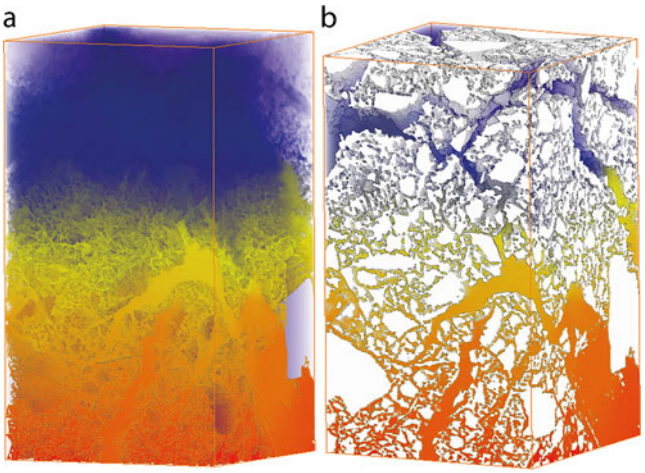

Fig. 7 3D imaging of the pressure field exerted from bottom to top along *z*-direction of ROI #1, where part **a** represents the distribution in the pore geometry, and **b** the same image pattern along with solid matrix. The *red* to *blue colors* represent the maximum (35 Pa) to minimum (≈0 Pa) pressure gradient. Soil sample height is 0.74 mm (=1,000 voxels)

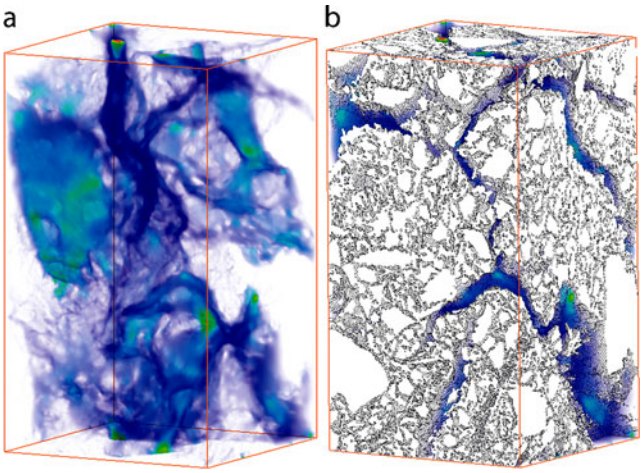

Fig. 8 Velocity vector field in 3D along *z*-direction of ROI #1, where part **a** shows the distribution magnitude in the pore geometry, and **b** the same magnitude distribution imaged with solid matrix. The *blue* to *red colors* depict the lower to higher local fluid velocities with moderate velocity of 2×10^{-3} m/s (*green color*). Soil sample height is 0.74 mm (=1,000 voxels)

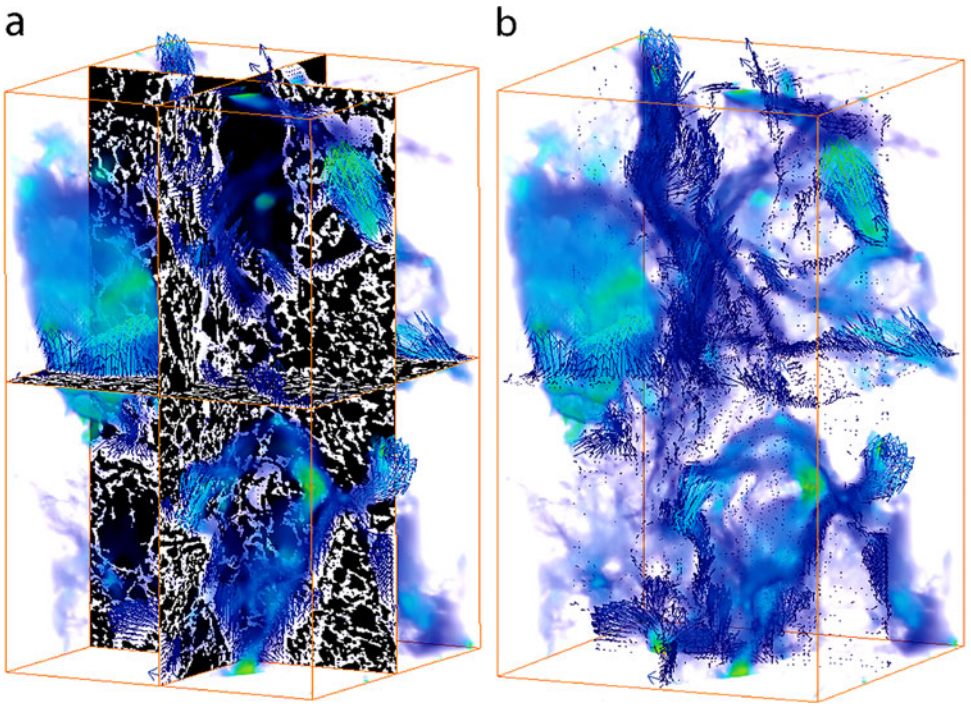

Fig. 9 3D image of the velocity magnitude with directional streamlines. Both images display the possible velocity vector magnitude with 3D arrow directions. The *blue* to *red colors* depict the lower to higher local fluid velocities with moderate velocity of 2×10^{-3} m/s (*green color*). Soil sample height is 0.74 mm (=1,000 voxels)

of 1 Darcy ($=10^{-12}$ m^2). Table 2 shows the resultant output parameters of the LBE fluid flow model for the soil aggregate ROI #1. As a main result of the model, the permeability tensor normal to *z*-direction is much higher (nearly 60%) than both the other permeability tensors normal to *x*, *y*-directions. This result confirms that our sample has a highly connected macro- and mesopores network in the *z*-direction. Estimations of mean flow velocity and permeability are an important prerequisite to understand the movement of water in the soil aggregate system that has great impact on the overall solute transport and biogeochemical activities along the soil interface network. Once the physical permeability tensor, k, is established, it can be recalculated into the effective saturated hydraulic conductivity, $K_s=k\rho g\mu^{-1}$ (cm day^{-1}), for the respective physical boundary conditions. In Table 3, the respective K_s values for all three ROIs and directions are listed. Nonetheless, the variation of geometrical parameters and hydraulic conductivity values thus obtained for the three independent subsample ROI volumes is rather moderate (see Tables 1 and 3).

The volume-averaged permeability can now be compared with predictions based on empirical formula such as the well-known Kozeny–Carmen equation, $k = \Phi^3/2S^2$ which relates the permeability, k, with the porosity, Φ, and the specific surface, S, of the porous medium. The common physical interpretation of this equation is that $1/S$ is in principle an intrinsic length scale associated with a typical pore size, and the power-law portion is accounting for the tortuosity and connectedness of the pore space. The average saturated hydraulic conductivity thus predicted for our ped samples is $K_s=$ 90 cm day^{-1}, which agrees with our LBM-simulated volume-averaged $K_s=105\pm24$ cm day^{-1} (mean of all ROIs and directions, see Table 3). However, this agreement happened merely by chance because of the scaling effect. The main factor contributing to the variation in permeability for a given porosity is the specific surface. The rescaling of a porous medium by a factor of n will preserve its porosity but drastically change the permeability by a factor of n^2 (i.e., the specific surface decreases by a factor of n). This scaling effect is the reason why in literature many modifications exist of the original Kozeny–Carmen relation in case adapted by additional factors to the individual sample scale, in particular, in the high (sand) and low (clay) porosity regimes. Other empirical predictions more common in soil science are

Table 2 Evaluation of LBE simulation run results for ROI #1

Simulation direction	Running time on 16-node HPC, h	Mean flow velocity (v), m s^{-1}	Permeability tensor (k), m^2		
x	1.08	8.38×10^{-5}	8.86×10^{-13}	5.08×10^{-14}	1.69×10^{-13}
y	1.71	8.12×10^{-5}	4.76×10^{-14}	8.59×10^{-13}	-5.31×10^{-13}
z	1.95	6.92×10^{-5}	1.62×10^{-13}	-5.04×10^{-13}	1.46×10^{-12}

Table 3 Evaluation of reproducibility and comparability for saturated hydraulic conductivity predictions

Simulation direction	LBE model (K_s), cm day^{-1}	GMPS, mm	GSD (−)	PTF predicted (K_s), cm day^{-1}
ROI #1		0.050	2.58	14.1
x	75			
y	73			
z	123			
ROI #2		0.017	2.44	10.4
x	71			
y	109			
z	135			
ROI #3		0.036	2.54	13.1
x	72			
y	126			
z	105			

statistical regression equations involving the GSD instead of the specific surface and bulk density instead of the porosity, the so-called "PTFs." Therefore, PTFs use only standard soil textural information and bulk density and are a common simple empirical way to estimate hydraulic parameters (Pachepsky and Van Genuchten 2011). Clearly, the PTF input parameters do not describe the structure of pore space per se like the Kozeny–Carmen relation and therefore do not represent hydropedological relationships between structure and hydrologic functions on the pore scale. Tietje and Hennings (1996) recommend for German soils of textural class Slu using the Campbell equation (Campbell 1985):

$$K_s = 339(1.3/\rho_b)^{1.3b}\exp(-6.9f_c - 3.7f_s) \quad (1)$$

where the predictor variables are the dry bulk density, ρ_b (1.5 gcm^{-3}), the clay fraction, f_c (0.15), the silt fraction, f_s (0.45), and b=GMPS$^{-0.5}$+0.2GSD, with the geometric mean of the particle size GMPS (mm) and the geometric standard deviation of the particle size distribution GSD. The latter two parameters can be precisely calculated from the tomographic data (see Table 3). However, the thus predicted moderate saturated hydraulic conductivity K_s=12±2 cm day^{-1} deviates by one order of magnitude from our LBM-simulated volume-averaged K_s value. Results of PTF applications are always uncertain, and the accuracy of PTFs outside of its development dataset is generally to be tested. It is well known that PTFs are underestimating the saturated hydraulic conductivity compared to field-measured values due to preferential flow effects (Fox et al. 2005). This possible explanation appears to be justified even on the spatial domain of a single loamy soil aggregate with macropore flow paths as shown in Fig. 6. The presence of macropores can cause an error in the estimation of the saturated conductivities even with most sophisticated PTFs based on the Mualem–van Genuchten equation, such as used by the software CalcPTF based on a multi-model PTF ensemble prediction technique (Guber and Pachepsky 2010).

4 Conclusions and perspectives

The implementation of a three-dimensional real void geometry image of a soil aggregate using synchrotron-based nano-CT provides us with the essential input to calculate, at the pore nano-scale, both geometrical network parameters and fluid flow properties. In our study, we presented a pore-level modeling of incompressible fluid flow on the basis of the LBE for soil media, i.e., heterogeneous velocity field vector while applying straightforward simple boundary conditions. The results indicate that the porous media within the image domain is highly heterogeneous and anisotropic. For the fluid flow simulation, the LBE model combines with three virtual elements: (i) the reliable description of the pore space, (ii) solutions of incompressible Navier–Stokes equations, and (iii) utilization of boundary conditions to acquire fluid properties. We found GeoDict software to run quite smooth and stable on a parallelized high-performance cluster computing environment. Thus, the established model can be used as a tool to study flow and solute transport under different hydraulic conditions in soil. With respect to the reproducibility of our fluid flow simulation approach, the most important single source of uncertainty in the numerical results is the rather poor statistics obtained due to the low number and small ROI size. This work has shown, however, that even at this limited subsample size, the percolation tensor calculation yields in reproducible results. The overall statistical precision of the values of permeability computed for three subsamples is moderate for the flow conditions applied and not essentially larger than the typical uncertainty of corresponding results from whole soil column experiments. Large enough samples are warranted in order to obtain statistically meaningful results. In practice, however, the restricted HPC capacity necessitates compromising between high resolution and large sample size. Fast advancements in computer capability and performance are a reliable prerequisite for the upscaling of this method ($\geq$2,048^3 voxels) even at the submicron spatial resolution of (currently) 0.37 μm. Nonetheless, technical constrains mainly due to computing capacity currently limits the sample size for pore structure imaging to a factor of 10,000 times the resolution (10^{12} voxels) and for fluid flow modeling to a factor of 1,000 times the resolution (10^9 voxels). Although this variation does not necessarily correspond to the large-scale variation of the entire soil Ap horizon but merely the variation within the yet rather small ROIs scanned, this surprisingly good precision arising from discretization and

image quality should provide an important prerequisite for a reliable upscaling. Saturated condition was chosen as a first approximation for fluid flow modeling, but unsaturated conditions may be represented by a multi-phase model with water and air as two separate void-filling phases. With this high resolution, the next step is to extend the simulations to water retention curves of unsaturated soil samples and compare with those predicted by PTFs. Moreover, accurate values of the macroscopic parameter (e.g., permeability, capillary pressure), which depend on the pore structure and pore-level physical processes, can be taken into account, while modeling at the continuum (lab) scale where a concept of representative elementary volume (REV) is essential.

Acknowledgements The authors gratefully acknowledge the financial support provided by the Deutsche Forschungsgemeinschaft (DFG) under priority program "Biogeochemical Interfaces in Soil" (SPP 1315). The nanotomography experiments were performed on the TOMCAT beamline at the Swiss Light Source, Paul Scherrer Institut Villigen, Switzerland. Oliver Schwarz helped during tomography data collection at the beamline. We thank Stephan Schulz (Helmholtz Zentrum München) for providing us with the Scheyern reference soil sample and its composition data.

References

Bartoli F, Bird NRA, Gomendy V, Vivier H, Niquet S (1999) The relation between silty soil structures and their mercury porosimetry curve counterparts: fractals and percolation. Eur J Soil Sci 50:9–22

Baveye PC, Laba M, Otten W, Bouckaert L, Sterpaio PD, Goswami RR, Grinev D, Houston A, Hu Y, Liu J, Mooney S, Pajor R, Sleutel S, Tarquis A, Wang W, Wei Q, Sezgin M (2010) Observer-dependent variability of the thresholding step in the quantitative analysis of soil images and X-ray microtomography data. Geoderma 157:51–63

Bronnikov AV (2002) Theory of quantitative phase-contrast computed tomography. J Opt Soc Am A 19:472–480

Calboun PS, Duszyk BS, Heath DG, Carley JC, Fishman EK (1999) Three-dimensional volume rendering of spiral CT data: theory and method. RadioGraphics 19:745–764

Campbell GS (1985) Soil physics with BASIC—transport models for soil–plant systems. Developments in Soil Science, vol 14. Elsevier, Amsterdam, pp 150

Carminati A, Kaestner A, Flühler H, Lehmann P, Or D, Lehmann E, Stampanoni M (2007) Hydraulic contacts controlling water flow across grains. Phys Rev E 76:026311. doi:10.1103/PhysRevE.76.026311

Culligan KA, Wildenschild D, Christensen BSB, Gray WG, Rivers ML (2006) Pore-scale characteristics of multiphase flow in porous media: a synchrotron-based CMT comparison of air-water and oil-water experiments. Adv Water Resour 29:227–238

Fourie W, Said R, Young P, Barnes DL (2007) The simulation of pore scale fluid flow with real world geometries obtained from X-ray computed tomography. Proc COMSOL Conf 2007, Newton, MA, USA, pp 6 (http://www.comsol.com/papers/3039/download/Fourie.pdf)

Fox AL, Eisenhauer DE, Dosskey MG (2005) Modeling water and sediment trapping by vegetated filters using VFSMOD: comparing methods for estimating infiltration parameters. ASAE Pap No. 052118. http://abe.ufl.edu/carpena/files/pdf/software/vfsmod/ModelingWaterAndSedimentTrapping.pdf

Gallagher NC Jr, Wise GL (1981) A theoretical analysis of the properties of median filters. IEEE Trans ASSP 29:1136–1141

Ginzburg I, d'Humiéres D (2003) Multireflection boundary conditions for lattice Boltzmann models. Phys Rev E 68:066614. doi:10.1103/PhysRevE.68.066614

Ginzburg I, Steiner K (2003) Lattice Boltzmann model for free-surface and its applications to filling processes in casting. J Comput Phys 185:61–99

Graf von der Schulenburg DA, Pintelon TRR, Picioreanu C, Van Loosdrecht MCM, Johns ML (2009) Three-dimensional simulations of biofilm growth in porous media. AICHE J 55:494–504

Guber AK, Pachepsky YA (2010) Multimodeling with pedotransfer functions, documentation and user manual for PTF calculator (CalcPTF), version 2.0. Environmental Microbial and Food Safety Laboratory, Hydrology and Remote Sensing Laboratory, Beltsville Agricultural Research Center, USDA-ARS. http://www.ars.usda.gov/Research/docs.htm?docid=21211

Guber AK, Pachepsky YA, Shein E, Rawls WJ (2004) Soil aggregates and water retention. Dev Soil Sci 30:143–151

Humières DD, Ginzburg I, Krafczyk M, Lallemand P, Luo LS (2002) Multiple-relaxation-time lattice Boltzmann models in three dimensions. Philos Trans R Soc Lond A 360:437–451

Inamuro T, Yoshino M, Ogino F (1999) Lattice Boltzmann simulation of flows in a three-dimensional porous structure. Int J Numer Meth Fluids 29:737–748

Kaestner A, Lehmann E, Stampanoni M (2008) Imaging and image processing in porous media research. Adv Wat Resour 31:1174–1187

Knutson CE, Werth CJ, Valocchi AJ (2001) Pore-scale modeling of dissolution from variably distributed nonaqueous phase liquid blobs. Water Resour Res 37:2951–2963

Kutilek M, Nielsen DR (2007) Interdisciplinary of hydropedology. Geoderma 138:252–260

Marone F, Hintermüller C, McDonald S, Abela R, Mikuljan G, Stampanoni M (2009) X-ray tomographic microscopy at TOMCAT. J Phys Conf Ser 186:012042. doi:10.1088/1742-6596/186/1/012042

Marone F, Münch B, Stampanoni M (2010) Fast reconstruction algorithm dealing with tomography artifacts. In Stock SR (ed) Developments in X-ray tomography VII. SPIE Proc 7804. doi:10.1117/12.859703

McDonald SA, Marone F, Hintermüller C, Mikuljan G, David C, Stampanoni M (2011) Phase contrast X-ray tomographic microscopy for biological and materials science applications. Adv Eng Mater 13:116–121

Murshed MM, Klapp SA, Szeder T, Huthwelker T, Stampanoni M, Marone F, Hintermüller C, Bohrmann G, Kuhs WF, Kersten M (2008) Natural gas hydrate investigations by synchrotron radiation X-ray cryo-tomographic microscopy (SRXCTM). Geophys Res Lett 35:L23612. doi:10.1029/2008GL035460

Pachepsky Y, Van Genuchten M (2011) Pedotransfer functions. In: Glinski J, Horabik J, Lipiec J (eds) Encyclopedia of agrophysics. Springer, Berlin

Pal NR, Pal SK (1993) A review of image segmentation techniques. Pattern Recogn 29:1277–1294

Pan C, Luo LS, Miller CT (2006) An evaluation of lattice Boltzmann schemes for porous medium flow simulation. Comput Fluids 35:898–909

Peth S (2010) Chapter 3—Applications of microtomography in soils and sediments. Developments in Soil Science, vol. 34. Elsevier, Amsterdam, pp 73–101

Peth S, Horn R, Beckmann F, Donath T, Fischer J, Smucker AJM (2008) Three-dimensional quantification of intra-aggregate pore-space features using synchrotron-radiation-based microtomography. Soil Sci Soc Am J 72:897–907

Pfrang A, Schladitz K, Wiegmann A, Schimmel TH (2007) Calculation of the evolution of surface area and free volume during the infiltration of fiber felts. Chem Vap Deposition 13:705–715

Porter ML, Wildenschild D (2010) Image analysis algorithms for estimating porous media multiphase flow variables from computed microtomography data: a validation study. Comput Geosci 14:15–30

Rennert T, Totsche KU, Heister K, Kersten M, Thieme J (2011) Advanced spectroscopic, microscopic and tomographic characterization techniques to study biogeochemical interfaces in soil. J Soils Sediments. doi:10.1007/s11368-011-0417-5

San José Martínez F, Martín MA, Caniego FJ, Tuller M, Guber A, Pachepsky Y, García-Gutiérrez C (2010) Multifractal statistics of discretized X-ray CT visualizations for the characterization of soil macropore structures. Geoderma 156:32–42

Sheppard AP, Sok RM, Averdunk H (2004) Techniques for image enhancement and segmentation of tomographic images of porous materials. Phys A Stat Mech Appl 339:145–151

Silin D, Tomutsa L, Benson SM, Patzek TW (2011) Microtomography and pore-scale modeling of two-phase fluid distribution. Transp Porous Med 86:495–515

Stampanoni M, Grošo A, Isenegger A, Mikuljan G, Chen Q, Bertrand A, Henein S, Betemps R, Frommherz U, Böhler P, Meister D, Lange M, Abela R (2006) Developments in X-ray tomography V. Proc SPIE 638:63180M1-14

Succi S (2001) The lattice Boltzmann equation: for fluid dynamics and beyond. Clarendon, Gloucestershire

Thoemmes G, Becker J, Junk M, Vaikuntam AK, Kehrwald D, Klar A, Steiner K, Wiegmann A (2009) A lattice Boltzmann method for immiscible multiphase flow simulations using the level set method. J Comput Phys 228:1139–1156

Tietje O, Hennings V (1996) Accuracy of the saturated hydraulic conductivity prediction by pedo-transfer functions compared to the variability within FAO textural classes. Geoderma 69:71–84

Tippkötter R, Eickhorst T, Taubner H, Greder B, Rademaker G (2009) Detection of soil water in macropores of undistrurbed soil using microfocus X-ray tube computerized tomography (mCT). Soil Tillage Res 105:12–20

Wildenschild D, Hopmans JW, Rivers ML, Kent AJR (2005) Quantitative analysis of flow processes in a sand using synchrotron-based X-ray microtomography. Vadose Zone J 4:112–126

Zhang X, Bengough AG, Deeks LK, Crawford JW, Young IM (2002) A novel three-dimensional lattice Boltzmann model for solute transport in variably saturated porous media. Water Resour Res 38:1167. doi:10.1029/2001WR000982

Paper II

Computers & Geosciences 56 (2013) 142–150

Contents lists available at SciVerse ScienceDirect

Computers & Geosciences

journal homepage: www.elsevier.com/locate/cageo

Simultaneous segmentation and beam-hardening correction in computed microtomography of rock cores

Zoran Jovanović *, Faisal Khan, Frieder Enzmann, Michael Kersten

Geoscience Institute, Johannes Gutenberg-University, Mainz 55099, Germany

ARTICLE INFO

Article history:
Received 9 October 2012
Received in revised form
13 March 2013
Accepted 14 March 2013
Available online 23 March 2013

Keywords:
Computed tomography
Beam hardening
Geologic samples
Image segmentation
Image analysis

ABSTRACT

We propose a post-reconstruction correction procedure for the beam-hardening artifact that neither requires knowledge of the X-ray spectrum nor of the attenuation coefficients in multi-mineral geologic samples. The beam-hardening artifact in polychromatic X-ray computer tomography (CT) hampers segmentation of the phase assemblage in geologic samples. We show that in cylindrically shaped samples like rock cores, the X-ray attenuation value for a single phase depends mainly on the distance from the center of the cylinder. This relationship could be easily extracted from the CT data for every phase and used to infer the presence of these phases at all positions in the sample. Our new approach enables simple segmentation of the phases for further analysis. Additionally, we propose a simple mathematical exercise for parallel beam geometry to show how recent experimentally observed deviations from Beer's law could be incorporated to model the beam-hardening artifact and simultaneously be used for its removal.

1. Introduction

X-ray computed tomography (CT) is a well-established diagnostic tool in life sciences. A quarter century ago, a medical CT scanner was for the first time adopted for work with geological samples (Vinegar and Wellington, 1987). Computer tomography has since matured gradually and has reached micrometer resolution (μCT) suitable for the imaging of bulk phase distribution and microstructure, and even temporal resolution for *in-situ* multiphase fluid transport studies (Berg et al., 2013). Recent hard- and software developments in the areas of high-resolution detector technology and user-friendly image reconstruction tools have given a tremendous boost to the use of desktop-based μCT instruments and techniques to address geologic problems. However, the reconstructed three-dimensional (3D) image quality is affected by several artifacts (Ketcham and Carlson, 2001; Krimmel et al., 2005). For heavy matrices such as geologic samples, the so-called beam-hardening artifact (BHA) derived from the X-ray spectrum is the most severe (Ketcham and Carlson, 2001). Although μCT provides 3D images of objects composed of multiphase assemblages, and it is possible to distinguish these phases with the naked eye, BHA hampers automatic image processing to separate these phases. This is a common problem in computer science today, where tasks that are very simple for the human brain (like the recognition of a simple object in an image) are still problematic for computers (Hawkins and Blakeslee, 2004). The use of μCT data in a quantitative manner, e.g. to infer the modal abundances of the minerals present or automatic estimation of their 3D shape parameters, is thus more severely hampered by artifacts than classical destructive microscopic techniques.

The main consequence of the BHA is that in μCT imaging, there is a range of attenuation values (hypo- or hyper-density effects like cupping and streak artifacts) rather than a single value for each single solid phase. The same solid phases seem to have generally higher attenuation values at the periphery than in the central regions of rock cores (Fig. 1b). This makes it quite difficult to quantitatively separate the different minerals, or to identify complex mineral relationships such as exsolution and zonation effects within a sample. The BHA effect originates in the use of polychromatic X-ray sources. All μCT reconstruction procedures are based on the assumption that attenuation coefficients with monochromatic X-rays do not change during passage through the bulk material in accordance with Beer's law. This is true only for synchrotron-based X-ray sources, but not for polychromatic X-ray beams common for desktop instruments. Since the low-energy part of the spectra is absorbed more during its passage through the sample, there is a continuous change in energy spectra, and consequently a non-linear change of attenuation on the X-ray propagation through the sample. The low-energy part of the spectrum is gradually removed and the X-ray beam becomes "harder" as a function of travel distance, which is why the artifact is called beam-hardening. In the resulting image, a single solid

* Corresponding author. Tel.: +49 6131 392 4780; fax: +49 6131 392 3070.
E-mail address: jovanovi@uni-mainz.de (Z. Jovanović).

0098-3004/$ - see front matter © 2013 Published by Elsevier Ltd.
http://dx.doi.org/10.1016/j.cageo.2013.03.015

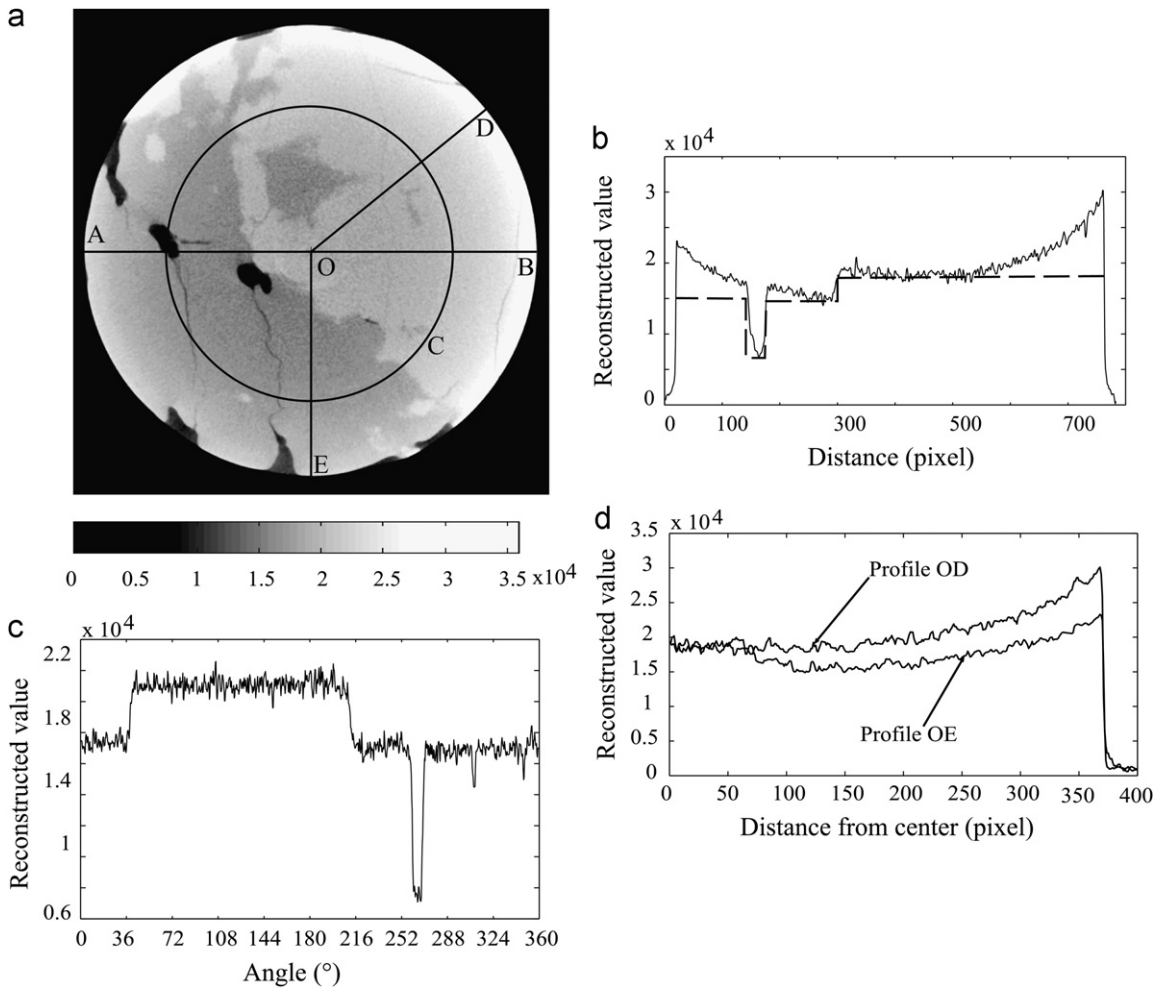

Fig. 1. (a) Horizontal cross section through an evaporite rock core. Solid lines represent profiles plotted on following figures: (b) profile AB (in a) shows a typical example of the beam-hardening artifact (BHA): instead of a single attenuation coefficient for a particular phase (dashed line), attenuation coefficients systematically decrease from the periphery to the center of the cylindrical rock core, (c) reconstructed attenuation coefficients at identical distance from the center (along circle C, 250 pixels away from the center, taken at every 0.36°) of the rock core. In this example, a single attenuation coefficient (within error) allows a simple segmentation of the phases and (d) profile OD shows the fortuitous example where the whole beam-hardening curve for the brighter material was extracted from a single profile. The darker phase in this slice does not occur in the central region, so values on profile OE are not giving the whole BHA curve and for central positions it is necessary to obtain the values from other slices.

phase is then represented by a range of reconstructed attenuation coefficients (or CT numbers) and consequently, the reconstructed image of a homogeneous mono-phasic sample seems to have changing densities depending on the voxel location.

A number of correction approaches have been proposed to resolve the BHA problem, but so far no general solution has been found. These methods are pre-filtering, linearization, post-reconstruction and dual energy methods. They are described in the following chapter. All of these methods, however, fail to remove the BHA in complex geological samples, since their application is limited to specific cases. For example, the pre-filtering method works well with light materials but complications arise when dealing with dense materials; the linearization method works very well but only for objects built only of one material; post-reconstruction methods work well only if segmentation of the materials is possible despite BHA; the dual energy method works well for medical purposes since it deals with materials of fairly known composition (e.g., brain tissue, water, fat, bone) but fails in the case when unknown materials are studied.

In this paper, we present an intriguing observation that the BHA in the reconstructed image is not only specific to each material but it also a radial function, i.e. it depends for each material only on the distance from the center of cylinder. This observation leads to a straightforward and simple method which uses the BHA to distinguish different materials and in this process can be applied to produce an image without beam-hardening. Additionally, some observations made by Van de Casteele et al. (2002, 2004) provide a possibility to describe the beam-hardening process in much simpler mathematical terms and explain our observations.

2. Overview of existing beam-hardening correction methods and their limitations

2.1. Pre-filtering

Hardware pre-filtering is the simplest and most widely used technique for reducing BHA by placing a filter, usually made of aluminum, copper, brass or other metal foils, between the X-ray source and the object, (Jennings, 1988). In this way, the low energy X-rays are already removed before the beam reaches the sample and the spectrum of the X-ray beam becomes pseudo-monochromatic. This is based on the fact that for the higher energy part of the spectrum the absorption coefficient is lower and, as a consequence, higher energies are harder to remove from the spectrum. This pseudo-monochromatization approach may reduce the extent of the artifact, but in most cases cannot

completely remove it. Although the samples built of the light materials require a smaller filter thickness than heavier materials, it is necessary to do separate study with multiple measurements of a single sample of unknown composition with the different filters, or different filter thickness of particular filter, to conclude what is the necessary thickness of the specific filter to remove the lower part of the spectra. Without that it can turn out that the filter thickness was not sufficient enough and that the BHA is still present. Furthermore, using filters reduces the intensity of the measured signal for all present phases and increases the noise. As a consequence, it reduces the contrast resulting in a final image of lower quality (Van Geet et al., 2000, 2001; Ketcham and Carlson, 2001; Van de Casteele et al., 2004).

2.2. Dual energy method

The dual energy approach is primarily based on a fact that the absorption coefficient depends not only on the energy but also on the chemical composition (effective atomic number) and density of the phase as a consequence of both photoelectric absorption and Compton scattering. Based on measurements at a single X-ray tube voltage, it is not possible to differentiate materials on basis of their density and chemistry. However, with measurement at two different tube voltages (different source spectra), this dual information can be derived (Alvarez and Macovski, 1976; Macovski et al., 1976; Lehmann et al., 1981; Remeysen and Swennen, 2006; Ivakhnenko, 2010). In this way the materials which are of similar attenuation coefficient but different chemistry or density could be differentiated. However, use of this approach also for beam hardening correction requires accurate *a-priori* knowledge about chemical composition and density of the materials present in sample (Macovski et al., 1976). This can be achieved in routine medical examination but not with unknown materials (Van Geet et al., 2000, 2001).

2.3. Linearization

The linearization method is simple and straightforward for specimen build only of a single material. The nonlinear relationship between attenuation and the distance X-rays travel though a sample could be acquired through reference measurement and can be fitted with polynomials. Using this polynomial approach the beam hardening can be corrected, i.e. every value on the polynomial is corrected towards the linear trend line which is expected in the monochromatic beam case (Brooks and Dichiro, 1976; Herman, 1979; Hammersberg and Mångård, 1998; Kachelriess et al., 2006).

The reference measurements are usually done on a step wedge shaped object. This step wedge shaped object has to be composed of the same material as the specimen, this could be in many occasions difficult to achieve. Furthermore, the reference measurement has to be performed under the same conditions (voltage, current, material, etc.) like for the specimen itself. Alternatively, the deviation from the Beers law determined out of the reconstructed CT image itself, since the specimens are build only out of one material.

Whatever the mechanism of learning about the deviation from Beers law is, through reconstructed image or through reference measurements, this information itself is not enough for the BHA correction of multi-material specimens. Namely, for correction of the deviation from Beers law in projections, it is required to know not only the deviation from Beers law of every material present but also the X-ray travel path (distance) through each material in each projection. Since the linearization method is limited to single material objects, it has no applicability in removing BHA in multi-component materials, which dominate geological samples.

2.4. Post-reconstruction methods

There are also a couple of post-reconstruction algorithms that basically change the raw sinogram data from a polychromatic-nonlinear towards a monochromatic-linear relationship between attenuation and distance of X-rays passing through an object at different distances to the phase of interest (Van de Casteele et al., 2002, 2004; Krumm et al., 2008). For this method it is necessary to know how attenuation at the given measurement condition is changing with thickness for each single phase. This relationship can be acquired either through measurements of wedge-shaped material standards (Van de Casteele et al., 2002, 2004) or by inferring it from projection data using beam tracing algorithms (Krumm et al., 2008). This is basically the same as linearization method but in following step based on first reconstruction, the segmentation of the phases is performed so that the travel paths or distances traveled by X-ray could be inferred for each projection. In some earlier papers (e.g. Ruegsegger et al., 1978) segmentation was not necessary since the spatial distribution of the phases in a samples was known. But only with this information, the projection data in the sinogram could be finally linearized and the attenuation values can be corrected towards a monochromatic linear trend line. This yields a new BHA-corrected sinogram, which is then reconstructed for a final BHA-free image. The limitation of these methods is that they are able to remove BHA in multi-material samples only if the materials can be segmented in the first reconstruction image, which for most geologic samples is not possible. BHA in most geological samples hinders segmentation of the phases and precludes quantitative use of μCT. Post-reconstruction correction methods (Van de Casteele et al., 2002, 2004; Krumm et al., 2008) were limited to samples for which the material absorption coefficients deviate so much that BHA does not preclude segmentation. Segmentation thus presents the major difficulty for accurate removal of the BHA problem.

3. Mathematical analysis of the BHA problem

The reconstruction procedure assumes a linear relationship between the attenuation and the absorption of the object according to Beer's law. However, in the polychromatic case each energy fraction is attenuated with a different attenuation coefficient for the same material, and attenuation generally increases for decreasing photon energy. The attenuation coefficient is changing non-linearly with distance, which causes the non-linear deviation from Beer's law even for homogeneous material. Van de Casteele et al. (2002, 2004) examined a number of phantom samples and found that the signal spectra can be described by a bimodal energy distribution, i.e. can be decomposed linearly into two basic functions, of which one is characteristic for low propagation distances and a second one for large distances. The relationship between attenuation and absorption coefficient with distance is then also bimodal, such that at small distances it is equal to Beer's law, while at large distances it is following Beer's law but shifted by some constant depending on material and measurement conditions (acceleration voltage of X-ray tube, etc.). This observation was subsequently used to suggest a correction method of the sinogram data for the beam hardening before reconstruction (Van de Casteele et al., 2002, 2004). The method works well for mono-phasic materials and could be used also to correct for the BHA in objects built of multi-component samples, but in the latter case it is necessary to segment the reconstruction image first. However, for the majority of geologic samples this is not possible due to beam hardening. Although the method could not favorably be applied in these cases, these observations provide a fundamental understanding of the beam-hardening process and could

be used to develop another approach for the solution of this problem. Moreover, these observations enable us to quantify the bias in the sinogram and to calculate and predict how this bias will propagate during the reconstruction calculations and result in the beam-hardening artifact on the final reconstruction image.

In fact, the non-linear relationship between the attenuation and absorption coefficients with distance can be represented by two linear relationships to predict how this will affect calculation during reconstruction. First, the attenuation for small distances is equal to Beer's law, $-\ln(I/I_0)=\mu_1 d$, while for large distances it becomes $-\ln(I/I_0)=K+\mu_2 d$. This is a simplified version of the equation (7) by Van de Casteele et al. (2004), where K denotes the intercept of the term $\mu_2 d$. Since for small distances there is no deviation from Beer's law, this region should produce a region with μ_1 during reconstruction but for large distances the constant K represents the bias from Beer's law. We will show below how this simple translation may lead to the beam-hardening artifact during reconstruction. In the case of a mono-phasic cylindrical object without the use of hardware filters, two regions may be separated depending on distances in sinograms, one region with relatively small distances where there is no beam hardening artifact, and another region with relatively large distances where the attenuation values are increased by the K constant. Consequently, after reconstruction there must be a small region at the periphery of the cylinder without beam hardening. However, this is not observed. Apparently, the critical distance where Beer's law is still valid is very small, and in cases with large samples and relatively small resolution the distances by which X-rays pass through the sample are always greater than this critical distance. For a rock-core cylinder of 15 mm diameter and a spatial resolution of 50 μm per pixel in a slice projection, the smallest distance X-rays pass through a sample is 0.5 mm (calculated using simple trigonometry) which is larger than the maximum critical distance where Beer's law applies (Van de Casteele et al., 2002, 2004). Under such conditions there is only one biased region in the whole sinogram. In this simplest case, every attenuation value in the sinogram is enhanced by the constant K, and the sinogram can be represented as a function $f(\xi,\Phi)$. The parameters ξ and Φ are coordinates in Radon space, where Φ is the projection angle, and ξ represents a position on the projection line. The constant K is represented by a rectangular function $\Pi(R/2\xi)$ for every projection angle Φ (The rectangle function is usually designated by Greek letter Π since its graph has the similar shape). For the case of a parallel beam geometry, the distribution of absorption coefficients in a slice projection $\mu(x,y)$, including the bias introduced in the poly-chromatic case, involves solving the inverse radon of sinogram $f(\xi,\Phi)$ according to the central slice theorem. This corresponds to a one-dimensional Fourier transformation of the sinogram for each angle Φ, then changing the coordinate system in Fourier space and at the end taking a two dimensional inverse Fourier transformation. The one-dimensional Fourier transformation of a rectangular function $\Pi(R/2\xi)$ is a scaled sinc-function

$$P(\rho,\Phi)=\int_{-\infty}^{\infty} e^{-2\pi i(\rho\xi)} K\prod\left(\frac{R}{2\xi}\right)d_\xi = 2KR\frac{\sin(2\pi R\rho)}{2\pi R\rho}=KR\frac{\sin(2\pi R\rho)}{\pi R\rho} \tag{1}$$

upon changing the orthogonal into a polar coordinate system with vectors $V_x=\rho\cos(\varphi)$ and $V_y=\rho\sin(\varphi)$, we get

$$F(V_x,V_y)=F(\rho)=KR\frac{\sin(2\pi R\rho)}{\pi R\rho} \tag{2}$$

and upon taking the inverse Fourier transformation in polar coordinates

$$f(r)=2\pi\int_0^{\infty} F(V_x,V_y)J_0(2\pi r\rho)\rho d\rho \tag{3}$$

where J_0 is a Bessel function of zero order and first kind

$$f(r)=2\pi\int_0^{\infty} KR\frac{\sin(2\pi R\rho)}{\pi R\rho}J_0(2\pi r\rho)\rho d\rho \tag{4}$$

The equation becomes ultimately an integral of a Bessel function which can be solved (Abramowitz and Stegun, 1964)

$$f(r)=\frac{2K}{2\pi\sqrt{(R^2-r^2)}}=\frac{K}{\pi\sqrt{(R^2-r^2)}} \tag{5}$$

A solution for $K=1$ is shown for a simulated mono-phasic cylindrical phantom sample in Fig. 2a. For objects of non-cylindrical shape, the solution will be a non-radial function. For the case of the rectangular object and $K=1$, the final result is depicted in Fig. 2b. The result is yet different from that observed for common laboratory measurements, because the actual beam geometry in desktop machines is not parallel. With a similar calculation for cone beam geometry, however, it is possible to predict the BHA for any shape, but that is out of scope of this paper.

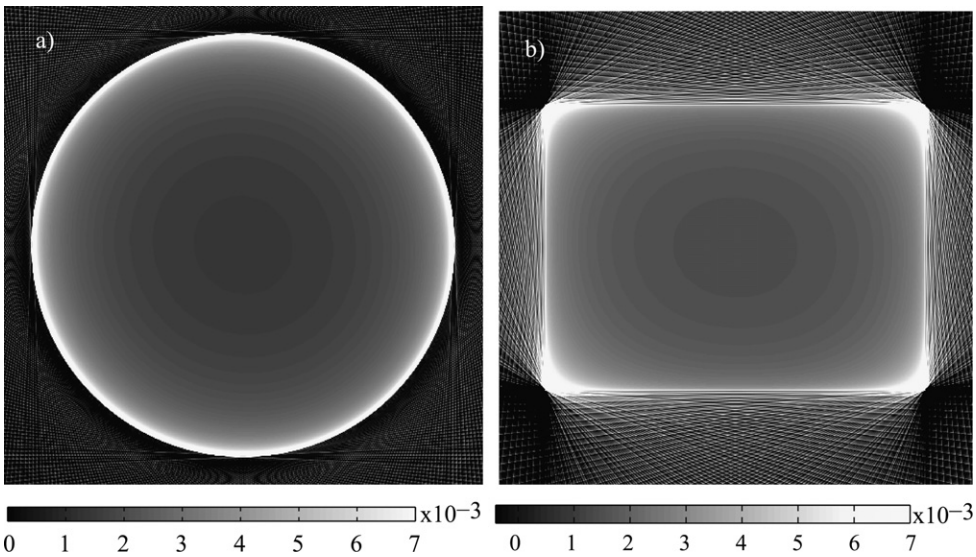

Fig. 2. (a) Simulated BHA for a parallel beam geometry of a cylindrical sample consisting only of one phase. Beam hardening is a radial function that depends only on distance from center and (b) simulated BHA for a rectangular sample in a parallel beam geometry. Note that beam hardening is not a radial function (as for the cylindrical sample), which depends not only on the distance but also on the angle in radial coordinates.

However, once the basic relationship inherent in the BHA is principally understood from a mathematical point of view, a simple correction approach may already be suggested.

4. Samples and experimental conditions

The custom-built μCT scanner used at our laboratory (ProCon CT-Alpha, Germany) is equipped with a microfocus X-ray tube (Feinfocus, Germany) featuring a diamond coated anode target with a focal spot size of a few μm. X-ray data acquisition is performed with a 2048×2048 pixels ("2k") flat panel CCD detector of size $105\,\text{mm} \times 105\,\text{mm}$ (Hamamatsu, Japan). Four cylindrical test objects were measured, two single-phase samples and two real multi-mineral rock core samples. The latter are granite and an evaporite rock composed of anhydrite with halite-sealed fractures. The first mono-phasic reference cylinder was made out of pure aluminum with a diameter of 30 mm; a second one of same dimensions was made out of plastic. Both objects were scanned by the same source voltage of 120 kV and at the same distance to the detector panel for an ultimate resolution of 57.1 μm per pixel. The rotation step was set at 0.45° with 0.5 s exposure time, which corresponds to 800 projections for a full 360° data acquisition. First, for an evaluation of the influence of different filters, these samples were measured once without filters and again with 1.0 mm aluminum, 0.5 mm copper, and 0.15 mm silver foil filters. The evaporite rock cylinder of 30 mm in diameter was measured at a source voltage of 130 kV with a 0.15 mm silver filter at a resolution of 53 μm per pixel. A granite cylinder of 18 mm in diameter was measured at a 100 kV source voltage without a filter at a 20.4 μm per pixel resolution. Exposure time was 1 s, with the same rotation step as for the previous samples, which yields 800 projections. Precise centro-symmetrical alignment of the cylinders along the vertical axis is an important prerequisite for success with the BHA correction procedure. The reconstruction of the 3D dataset was performed by the classical backprojection-type algorithm according to Feldkamp et al. (1984).

5. Segmentation procedure based on observations of beam-hardening artifact

Depending on the shape of the object, isolines of reconstructed attenuation values follow different complex paths. For the special case of axial-symmetrical mounted vertical cylindrical samples, however, there is a simplification in that the isolines approach the shape of circles. On circular sections normal to the axial z-axis in the cylinders, the points at the same distance from center representing the same composition yield the same reconstructed attenuation value (Fig. 1c). In other words, within each slice of the cylinder perpendicular to z-axis, points of same composition on any circular trajectory have the same reconstructed attenuation values within experimental error. The beam-hardening artifact is a radial function, and consequently the reconstructed attenuation value depends on the distance from the center of the cylinder (beam-hardening curve). In addition, values along the z-axis do not change, excluding the small areas at the top and bottom of the cores (smallest and largest z-coordinates, Fig. 3). These areas reside outside the Tam-Danielsson window (Danielsson et al., 1997; Tam et al., 1998), and their reconstruction is therefore problematic. Unfortunately, they cannot be segmented and have to be cut away from the image. The change of attenuation values in the slice plane perpendicular to the z-axis follows an exponential or parabolic beam-hardening curve from the center to periphery, with a bump at the periphery close to the edge (Fig. 4). The exact location and shape of the bump depends on the material used and could become narrow with large magnitude, or wider with lower magnitude. In the case of metal foil filtering, the bump may disappear for some materials.

For our approach it is necessary to extract from the reconstructed data how attenuation values change from the center to

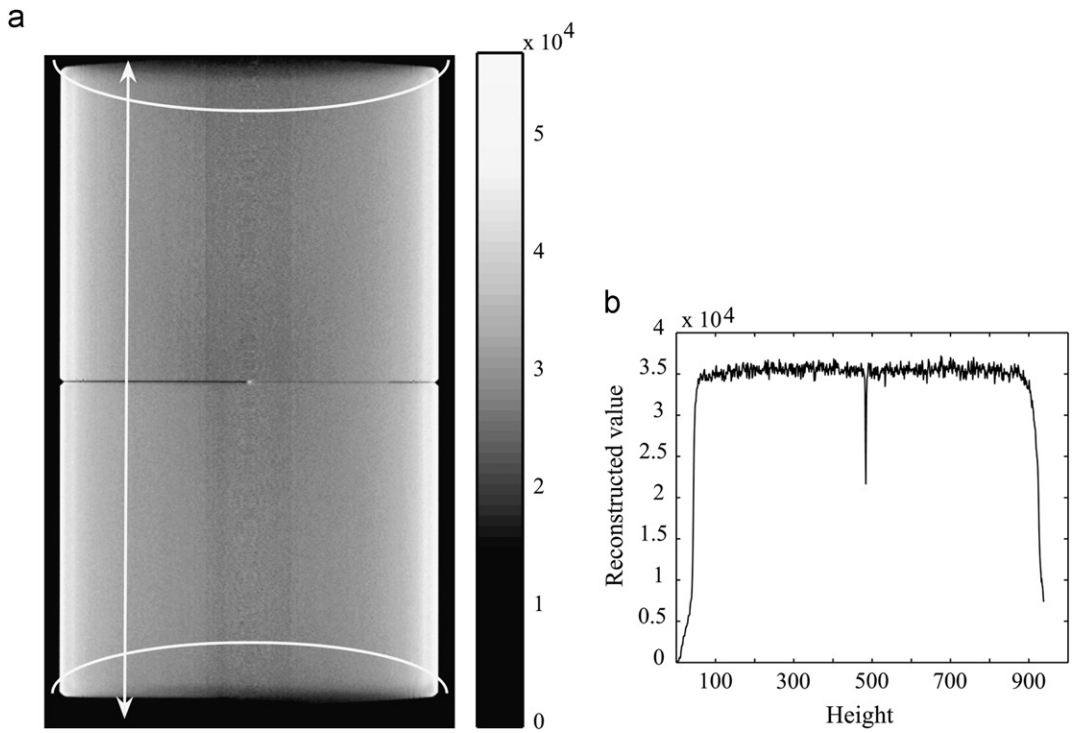

Fig. 3. (a) Vertical cross section of an aluminum cylinder sample. The profile is shown in (b) and the white curved lines are marking the Tam–Danielson window and (b) values at the identical distance from the cylinder center are constant along the vertical axis, except for very low and very high Z (outside of Tam–Danielson window).

the periphery for each material, i.e., the first step is extraction of BHA curves. Unfortunately, extraction of beam-hardening curves cannot be done automatically. Rather, it is necessary to extract the data of each material from the center to the periphery manually. In the simplest case, it is sufficient to search for a profile where only one material appears to yield a BHA curve (profile OD on Fig. 1a). However, this case occurs rarely in geologic materials. The approach may be applicable to samples in which one phase is particularly abundant and uniformly distributed. For less abundant and/or heterogeneously distributed phases, it is necessary to acquire several profiles from a single slice, or different slices, to ensure that the values at all positions are extracted.

A single beam-hardening curve may still suffice, but because of a relatively weak signal-to-noise ratio, precision could be increased significantly by bundling a larger number of such beam-hardening curves and calculating their mean (Figs. 4c and 5). This manual procedure could thereby become tedious and demanding, especially in cases of relatively small grain size domains. In principle, a number of algorithms may be used for an automatic recognition of such lines and curves in images (Hansen and Toft, 1996; Stanford and Raftery, 2000).

Alternatively, we noticed from the mathematical derivation of the BHA problem discussed above, that the radial profiles could be well approximated with a single curve. We found empirically that an exponential curve of the type $\mu = \mu_0 e^{-k\sqrt{R^2-r^2}}$ (Fig. 4a, b) approximates the data very well, where μ_0 and k are constants, R is the diameter of cylinder, and r is the actual distance of the phase pixel from the center of the cylinder. The recent excellent software solution for automatically finding mathematical dependences from data could also be used to obtain improved approximations (Schmidt and Lipson, 2009).

In a subsequent step, constants can be found by a simple least square fitting procedure. The implementation of this approach first requires information about the distribution of reconstructed attenuation values of a certain phase from the center to the periphery, as discussed above (either by taking a mean of a number of profiles or by approximations). Based on that information, an image of an artificial object consisting exclusively of that phase is constructed. This artificial object has the same attenuation values of the phase concerned in the real rock sample, but differs significantly from other phases. Then, the simple arithmetic difference between the measured data and the artificial object data provides information about the presence of the phase at all positions in the studied sample. It is around zero ($\pm$ error) if the phase is present and smaller or bigger than the error at positions of the object where another phase is present (Fig. 6a). Reiteration of this correction procedure for all different solid phases yields the segmented image.

In summary, the procedure consists of six steps: (i) from the acquired data, the extraction of the beam-hardening curve for one phase, (ii) construction of an artificial object built only of that phase, (iii) calculation of the arithmetic difference between the artificial object and the reconstructed image, (iv) confirmation that the phase is present at positions where the result is around zero ($\pm$ standard deviation), or (v) confirmation that a different phase is present at that position if this difference is larger than the

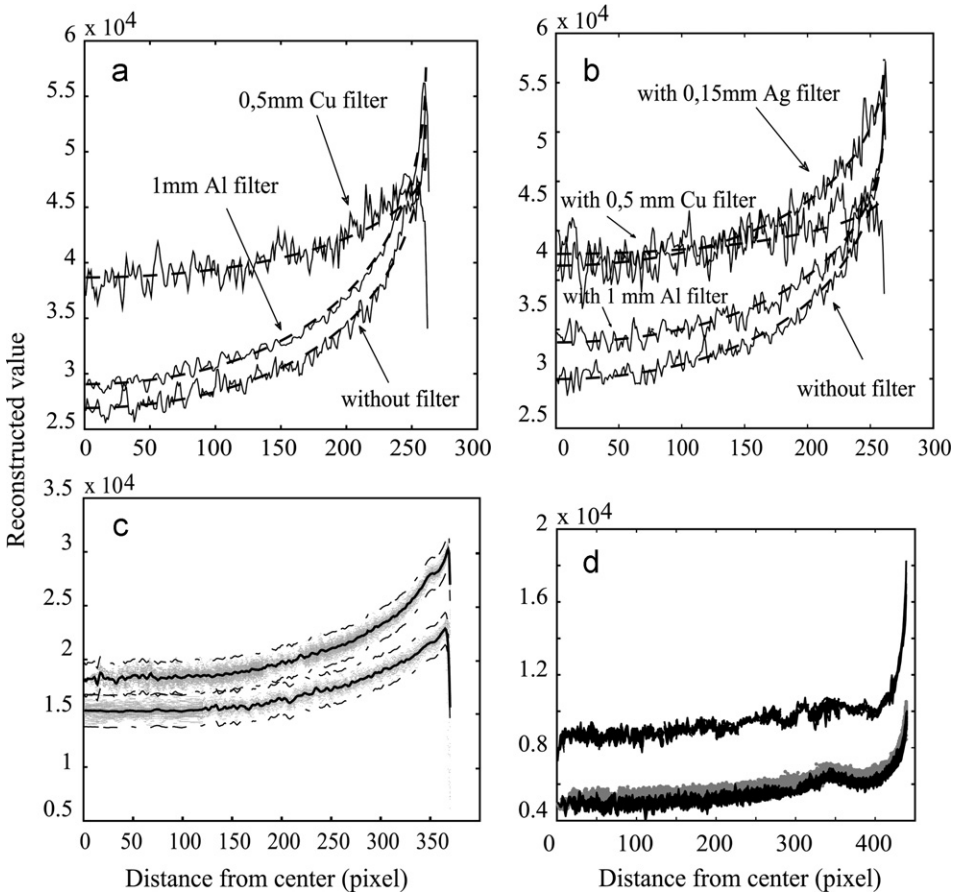

Fig. 4. BHA curves for (a) an aluminum cylinder and (b) plastic cylinder with different filters applied. The applied filters do not remove BHA. The function (dashed lines) $\mu = \mu_0 e^{-k\sqrt{R^2-r^2}}$ approximated the BHA curves, (c) considering the large measurement errors due to noise, precision of the BHA curve is improved by taking the average value (solid lines) of a large number of profiles. Dashed lines represent average value $\pm$ 250 and (d) plot of the data used for the extraction of BHA curves for a granite sample. Note that the darkest phases (quartz, K-feldspar and Na-rich plagioclase) have an overlap within the error with calcic plagioclase (gray).

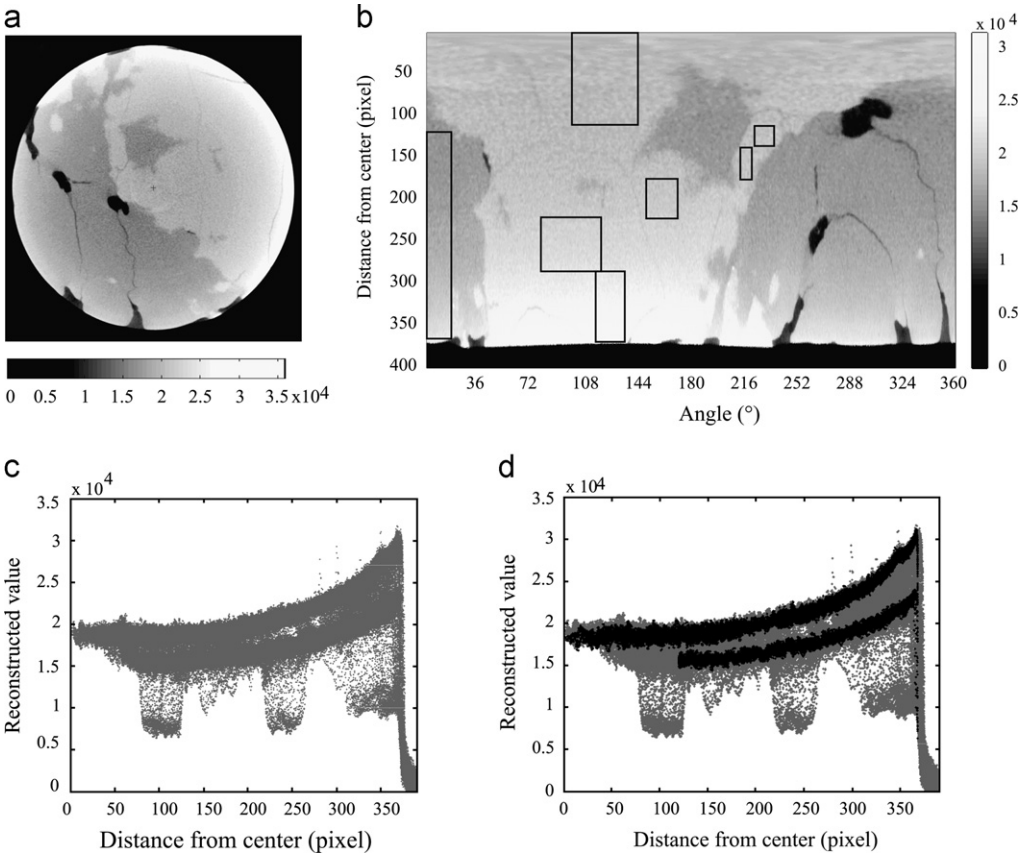

Fig. 5. (a) Horizontal cross section through an evaporite rock core, (b) image created by stacking 1000 profiles from the center to the periphery at an interval of 0.36°. In this way it is easier to extract BHA curves with Cartesian coordinates for each phase. Black boxes are areas from which the data are extracted and shown in (d), (c) plot of all data from a single slice as function of distance and (d) superimposed by two additional phases (darker) extracted from areas shown in (b). Note that the phase with lower values is not present in the central region, requiring that this part of the BHA curve for this phase must be extracted from another slice.

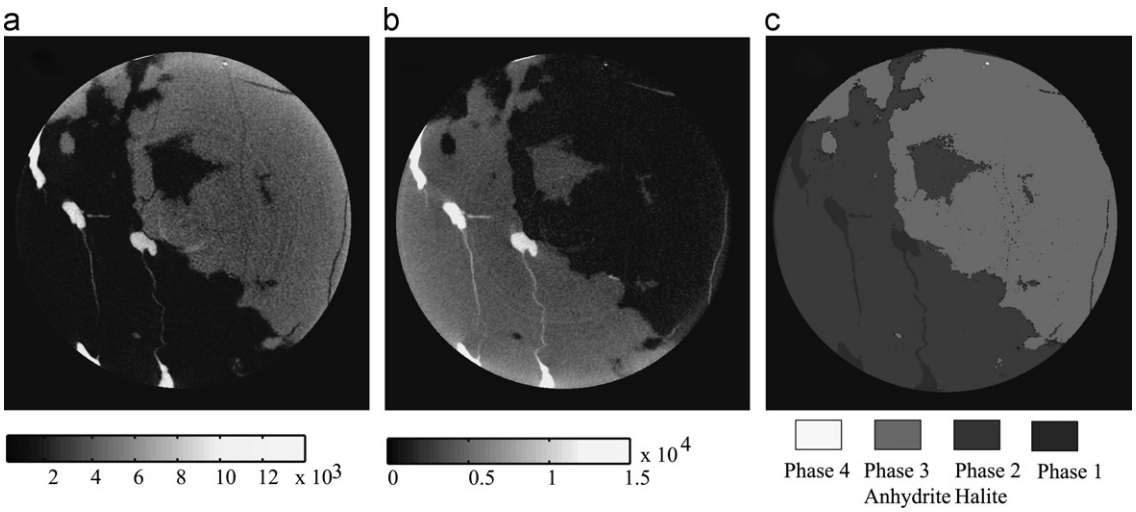

Fig. 6. (a) The original evaporite sample image and (b) the arithmetic difference between the original image and image for a calculated mono-mineral assemblage. A result value around zero means that the targeted mineral is present at that position. (c) Final segmented image for an evaporite sample, following a stepwise arithmetic-difference assignment approach shown in (b).

standard deviation, and ultimately (vi) repetition of this procedure until the distribution of all phases is accounted for. Occasionally, it is not necessary to repeat the procedure for each phase but it suffices to have values for one phase. A differential image between the original dataset and that of this phase could then be applied to segment the image. In the areas where this phase is present, the attenuation values should become around zero but other materials have non-zero and mineral specific values, which could then be used to segment all phases (Fig. 6b). The final result of this correction procedure for the evaporite rock sample is shown in Fig. 6c.

In a multi-component case where several phases have similar attenuation coefficients, phase separation is not possible and eventually these phases have to be treated as a single phase.

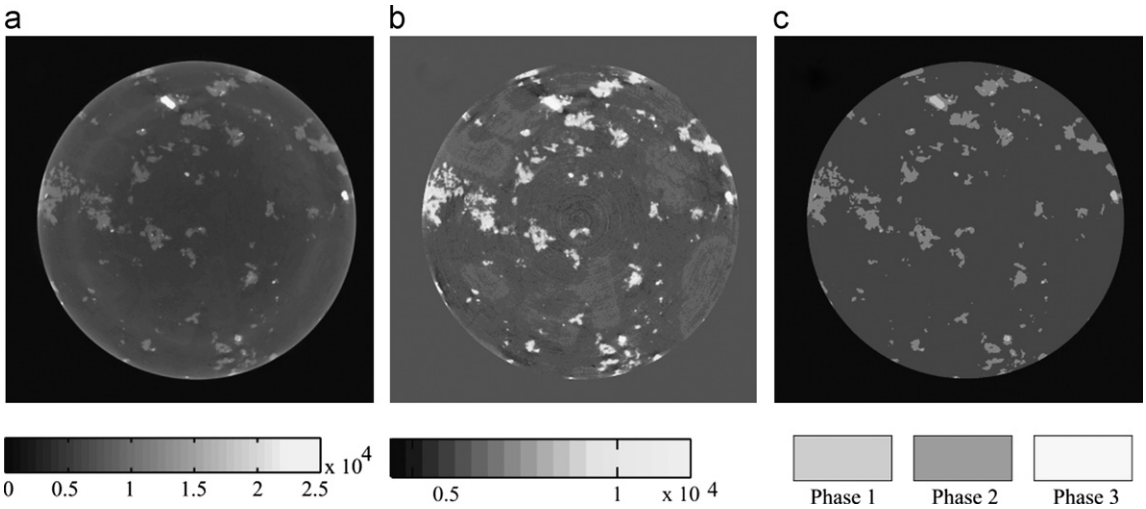

Fig. 7. Horizontal cross section through a granitic rock core: (a) original reconstructed image, (b) image of absolute difference between original image and darkest phase object. Notice that the grain boundaries of the minerals that are not separable are more clearly visible and (c) segmented image of the granitic sample.

For example, in a granite sample, the silicates quartz and feldspar (albitic plagioclase and orthoclase) have quite similar attenuation coefficients (lowest values in Fig. 4d), while plagioclases with higher anorthite content have slightly higher values, but still have large overlap with lowest phases within error (Fig. 4d) and therefore cannot be separated from quartz and other feldspars. However, even if it is impossible to separate these phases using our segmentation method, the resulting image (original image minus values of darkest phase) is of better quality and more clearly shows the grain boundaries of these phases (Fig. 7b). The final segmented image for granite is depicted in Fig. 7c.

6. Conclusions

In cylindrically shaped samples there is a simple dependence of beam-hardening of each phase on its position in a sample (here distance from center of a rock core cylinder). This relationship can be extracted from the first reconstructed image and is used to infer its positions in each slice, allowing a rigorous segmentation of the image. In non-cylindrical samples, beam-hardening is not a radial function and changes along each angle. While image segmentation is possible, this approach may be too complicated and impractical for non-cylindrical samples. Here it is also shown how the model of Van de Casteele et al. (2002, 2004) can be used to calculate BHA in parallel beam geometry. Our main suggestion for further research is that such calculations should be extended for cone beam geometry of desktop μCT machines to enable segmentation and BHA removal regardless of sample shape.

Acknowledgment

We thank Jens-Oliver Schwarz, Martin Wolf, Branimir Šegvić and Eric Hellebrand for helpful discussions. In addition we would like to thank Eric Hellebrand and Helen Clark for greatly improving the quality of English in this manuscript. This work was supported by the BMBF Grant 02C15262.

References

Abramowitz, M., Stegun, I.A., 1964. Handbook of Mathematical Functions with Formulas, Graphs, and Mathematical Tables. U.S. Government Printing Office, Washington 1046 pp.

Alvarez, R.E., Macovski, A., 1976. Energy-selective reconstructions in X-ray tomography. Physics in Medicine and Biology 21, 733–744.

Berg, S., Ott, H., Klapp, S.A., Schwing, A., Neiteler, R., Brussee, N., Makurat, A., Leu, L., Enzmann, F., Schwarz, J.-O., Kersten, M., Irvine, I., Stampanoni, M., 2013. Real-time 3D imaging of Haines jumps in porous media flow. Proceedings of the National Academy of Sciences of the United States of America 110, 3755–3759.

Brooks, R.A., Dichiro, G., 1976. Beam hardening in X-ray reconstructive. Physics in Medicine and Biology 21, 390–398.

Danielsson, P.E., Edholm, P., Eriksson, J., Magnusson, S.M., 1997. Towards exact reconstruction for helical cone-beam scanning of long objects, In: Townsend, D.W., Kinahan, P.E. (Eds.), Proceedings of 1997 Meeting on Fully 3D Image Reconstruction in Radiology and Nuclear Medicine, Pittsburgh, PA, pp. 141–144.

Feldkamp, L.A., Davis, L.C., Kress, J.W., 1984. Practical cone-beam algorithm. Journal of the Optical Society of America A: Optics Image Science and Vision 1, 612–619.

Hammersberg, P., Mångård, M., 1998. Correction for beam hardening artefacts in computerised tomography. Journal of X-Ray Science and Technology 8, 75–93.

Hansen, K.V., Toft, P.A., 1996. Fast curve estimation using preconditioned generalized radon transform. IEEE Transactions on Image Processing 5, 1651–1661.

Hawkins, J., Blakeslee, S., 2004. On Intelligence, 1st ed. Times Books, New York 261 pp.

Herman, G.T., 1979. Corrections for beam-hardening in computed-tomography. Physics in Medicine and Biology 24, 81–106.

Ivakhnenko, V.I., 2010. A novel quasi-linearization method for CT image reconstruction in scanners with a multi-energy detector system. IEEE Transactions on Nuclear Science 57, 870–879.

Jennings, R.J., 1988. A method for comparing beam-hardening filter materials for diagnostic-radiology. Medical Physics 15, 588–599.

Kachelriess, M., Sourbelle, K., Kalender, W.A., 2006. Empirical cupping correction: a first-order raw data precorrection for cone-beam computed tomography. Medical Physics 33, 1269–1274.

Ketcham, R.A., Carlson, W.D., 2001. Acquisition, optimization and interpretation of X-ray computed tomographic imagery: applications to the geosciences. Computers and Geosciences 27, 381–400.

Krimmel, S., Stephan, J., Baumann, J., 2005. 3D computed tomography using a microfocus X-ray source: analysis of artifact formation in the reconstructed images using simulated as well as experimental projection data. Nuclear Instruments and Methods in Physics Research Section A: Accelerators, Spectrometers, Detectors and Associated Equipment 542, 399–407.

Krumm, M., Kasperl, S., Franz, M., 2008. Reducing non-linear artifacts of multi-material objects in industrial 3D computed tomography. Nondestructive Testing and Evaluation International 41, 242–251.

Lehmann, L.A., Alvarez, R.E., Macovski, A., Brody, W.R., Pelc, N.J., Riederer, S.J., Hall, A.L., 1981. Generalized image combinations in dual KVP digital radiography. Medical Physics 8, 659–667.

Macovski, A., Alvarez, R.E., Chan, J.L., Stonestrom, J.P., Zatz, L.M., 1976. Energy dependent reconstruction in X-ray computerized tomography. Computers in Biology and Medicine 6, 325–336.

Remeysen, K., Swennen, R., 2006. Beam hardening artifact reduction in microfocus computed tomography for improved quantitative coal characterization. International Journal of Coal Geology 67, 101–111.

Ruegsegger, P., Hangartner, T., Keller, H.U., Hinderlint, T., 1978. Standardization of computed tomography images by means of material-selection beam hardening correction. Journal of Computer Assisted Tomography 2, 184–188.

Schmidt, M., Lipson, H., 2009. Distilling free-form natural laws from experimental data. Science 324, 81–85.

Stanford, D.C., Raftery, A.E., 2000. Finding curvilinear features in spatial point patterns: principal curve clustering with noise. IEEE Transactions on Pattern Analysis and Machine Intelligence 22, 601–609.
Tam, K.C., Samarasekera, S., Sauer, F., 1998. Exact cone beam CT with a spiral scan. Physics in Medicine and Biology 43, 1015–1024.
Van de Casteele, E., Van Dyck, D., Sijbers, J., Raman, E., 2002. An energy-based beam hardening model in tomography. Physics in Medicine and Biology 47, 4181–4190.
Van de Casteele, E., Van Dyck, D., Sijbers, J., Raman, E., 2004. A model-based correction method for beam hardening artefacts in X-ray microtomography. Journal of X-Ray Science and Technology 12, 43–57.
Van Geet, M., Swennen, R., Wevers, M., 2000. Quantitative analysis of reservoir rocks by microfocus X-ray computerised tomography. Sedimentary Geology 132, 25–36.
Van Geet, M., Swennen, R., Wevers, M., 2001. Towards 3-D petrography: application of microfocus computer tomography in geological science. Computers and Geosciences 27, 1091–1099.
Vinegar, H.J., Wellington, S.L., 1987. Tomographic imaging of three-phase flow experiments. Reviews in Scientific Instruments 58, 96–107.

Paper III

Pore morphology and lattice Boltzmann approach to modeling unsaturated soil capillary hysteresis and permeability tensor

Faisal Khan, Frieder Enzmann, and Michael Kersten

Institute of Geosciences, Johannes Gutenberg University, Mainz 55099, Germany

Submitted to Soil Science Society of America Journal

Abstract

Water retention relationships between capillary pressure, fluid/fluid interfacial area, and hydraulic conductivity were studied as functions of water saturation in a soil aggregate using numerical methods. The soil pore structure was investigated using synchrotron-based tomography, at 0.74 μm spatial resolution, and a pore-morphology approach was then used, fitting spheres into the pore space image according to the pore radii. The air and water phase distributions were quantified at the pore scale during simulated drainage and imbibition cycles, and the capillary pressure was calculated using the Young–Laplace equation. The air–water interfacial area reached a maximum at moderate water saturation in both drainage and imbibition cycles, the imbibition maximum being higher. The lattice Boltzmann simulation approach showed that uniformly distributed air blobs hampered the movement of water at different water saturation levels. The simulated hydraulic conductivity in the *x*-, *y*-, and *z*-directions reached 13.4 cm d^{-1} for both cycles, at an average flow of $4.2 \cdot 10^{-7}$ m s^{-1}, suggesting creeping flow at the pore scale when the pressure drop was 1 Pa in each direction. The hydraulic conductivity during drainage and imbibition showed relatively small hysteretic effects, caused by the range of pore sizes present affecting the flow simulation. The simulated hydraulic conductivity was compared with the hydraulic conductivities predicted by the Brooks and Corey–Burdine, and Van Genuchten–Mualem, models. Both empirical models proved capable of predicting the relative hydraulic conductivity for the porous medium at higher wetting degree, but the Van Genuchten–Mualem model overestimated the hydraulic conductivity at lower water saturation.

Abbreviations: BC, Brooks–Corey model approach; BCB, Brooks and Corey–Burdine model approach; GSD, grain size distribution; LB, Lattice Boltzmann model approach; NWP, non-wetting phase; PMB, pore morphology based; PSD, pore size distribution; ROI, region of interest; SE, structuring element; VG, Van Genuchten model approach; VGM, Van Genuchten–Mualem model approach; wFFT, wavelet fast Fourier transform; WP, wetting phase; μCT, X-ray computed microtomography;

Parameters (Latin letters): A_{awi} (mm^{-1}), specific interfacial area; *b* (-), empirical constant; *g* (9.8 m s^{-2}), acceleration caused by gravity; $\mathcal{K}$ (m^2), permeability; $\mathcal{K}_r$ (-), relative permeability; *K* (cm d^{-1}), hydraulic conductivity; K_r (-), relative hydraulic conductivity; K_s (cm d^{-1}), saturated hydraulic conductivity; K_{xx}, K_{yy}, K_{zz} (cm d^{-1}), hydraulic conductivity along axial direction; *m*, *n* (-), empirical shape-defining parameters; P_b (kPa), air entry pressure; P_c (kPa), capillary pressure; P_w (kPa), wetting phase pressure; P_{nw} (kPa), non-wetting phase pressure; *r*(m), pore radius; S_w (-), wetting phase (water) saturation; S_{wr} (-), residual water saturation; S_{nw} (-), non-wetting (air) saturation; S_{nwr} (-), residual air saturation; S_e (-), effective water saturation; *t* (s), time

Parameters (Greek letters): α (kPa^{-1}), empirical shape-defining parameter; λ (-), pore size distribution index; ρ_t (g cm^{-3}), bulk density (soil); η (g m^{-1} s^{-1}),

dynamic viscosity; υ (m^2 s^{-1}), kinematic viscosity; ρ (kg m^{-3}), density (water); γ (N m^{-1}), surface tension; θ (°), contact angle.

INTRODUCTION

In partially saturated porous media such as soil, complex water retention relationships emerge as the result of the dynamics of the immiscible air-water phase interface. A well-known macroscopic effect of this relation is the hysteresis observed during cycles of wetting and drainage. The geometric distribution of air-filled pores dynamically alters thereby the connectivity of the pore space, ultimately causing the effective pore volume available for fluid flow to decrease. Clearly, water retention mechanisms in partially saturated soil has important implications in pedohydrology, soil mechanics, nutrient and contaminant flow. Interest in using pore-scale modeling to achieve the reliable parameterization of macro-scale constitutive relationships between capillary pressure (P_c), water saturation (S_w), and relative permeability ($\mathcal{K}_r$) has therefore increased, in particular if the complex pore geometries and topology of the porous media are taken into account (Schaap et al., 2007; Chang et al., 2009; Rezanezhad et al., 2009; Blunt et al., 2013; Wildenschild and Sheppard, 2013). The success of a fluid flow model generally depends on the appropriate quantification of these relationships. The P_c–S_w relationship is used to quantify the degree of saturation (i.e., the water content, by volume) as a function of the capillary pressure in porous domains. The $\mathcal{K}_r$–S_w relationship is used to specify the relative permeability of a porous medium to a particular fluid phase (water in this case) at different saturation levels. Capillary pressure is the result of a two-phase flow in a porous medium, and is defined as the difference between the average non-wetting and wetting phase pressures (P_{nw}–P_w) for a given value of S_w (Bear and Verruijt, 1987; Helmig, 1997). This simple classical concept, however, is only valid under equilibrium conditions (i.e., when $\partial S_w/\partial t = 0$). This implies that all the factors that influence the distribution of two immiscible fluids in a porous medium at equilibrium (e.g., surface tension, particle and pore volume fractions, contact angles, the heterogeneities of the medium, anisotropy) are to be considered. In fact, the P_c–S_w relationship is not unique, and depends not only on the volume fraction of each phase, but also on the change in the degree of saturation over time, i.e., the two-phase flow dynamics are related to variations in saturation (Joekar-Nisar and Hassanizadeh, 2011). The non-uniqueness of the P_c–S_w and $\mathcal{K}_r$–S_w relationships in the drainage and imbibition processes is strongly affected by micro-heterogeneities at the pore scale rather than the inhomogeneous macroscopic flow field (Ataie-Ashtiani et al., 2002; Das et al., 2004).

The specific air–water interfacial area (A_{awi}) per unit volume of the porous structure is commonly considered to be a crucial parameter for understanding and interpreting flow processes in porous media (Hassanizadeh and Gray, 1993; Held and Celia, 2001; Joekar-Niasar et al., 2008, 2010b). This interfacial area plays a significant role in a number of processes, such as colloid transport (Wan and Wilson, 1994; Choi and Corapcioglu, 1997; Sirivithayapakorn and Keller, 2003; Crist et al., 2004; Shi et al., 2010), mass transfer in capillary microreactors (Ghaini et al., 2010), and microbial biocolloid retention (Steenhuis et al., 2006; Torkzaban et al., 2006). Advances in imaging technology, e.g., by using synchrotron-based X-ray computed microtomography (μCT), have made possible a high-resolution three-dimensional (3D) quantification of A_{awi} (Brusseau et al., 2006; Costanza-Robinson et al., 2008). The quantification of the specific surface area, as a function of water saturation, can now be used to investigate the effects of the distributions of two immiscible phases on flow processes at the pore scale. Moreover, high resolution images at a submicron spatial resolution allow matrix

pore-scale geometries to be quantified, allowing root/soil interactions to be examined (Anderson and Hopmans, 2013), and even Haines jumps to be visualized using high-speed tomography (Berg et al., 2013). It is also possible to characterize the distribution of fluid–fluid interfacial areas and measure solid–liquid interactions that lead to transport processes (Pierret et al., 2002; Gregory et al., 2003; Prodanović et al., 2007; Peth, 2010; Elyeznasni et al., 2012; Wildenschild and Sheppard, 2013).

The lattice Boltzmann method allows to directly involving physical-based pore-scale hydro-mechanical properties in complex geometries. When an LB model is used, a permeability tensor (which is an important transport property in inhomogeneous porous materials) can be predicted at the pore-scale, under different soil physical conditions (Nabovati and Sousa, 2007; Schaap et al., 2007; Boek, 2010; Koku et al., 2011; Gao et al., 2012, Galindo-Torres et al., 2013). A recent pore-scale study applying the LB approach has shown that the hysteresis of water retention during cycles of wetting and drainage arises from the dynamics of the solid-liquid contact angles as a function of the change of the local water volumes (Gan et al., 2013). However, this study was still performed on artificial granular media, as many such studies before. As a major benefit, use of a LB approach allows the straightforward incorporation of real soil pore geometry determined directly from μCT measurements (Christensen, 2006; Schaap et al., 2007; Sukop et al., 2008). This study is focused on using a synchrotron-based 3D image of a soil aggregate as a direct input microstructure for simulating and understanding the functional relationships during drainage and imbibition cycles, using a pore morphology based (PMB) modeling approach (Hilpert and Miller, 2001; Ahrenholz et al., 2008; Chan and Govindaraju, 2011). In our micro-scale approach, the PMB approach was extended to incorporate a linkage between the soil structure pore geometry and the macroscopic constitutive relationships between the capillary pressure, water saturation level, and interfacial area (P_c–S_w–A_{awi}) in a variably saturated porous soil medium, and the model was used to investigate subsequent hysteretic effects. In the second part of the study the effects of the geometric distribution of air on water movement was investigated (i.e., changes in hydraulic conductivity (K) as a function of the water saturation level). The simulated results were compared with $P_c(S_w)$ and $K(S_w)$ predictions using common empirical water retention models (e.g., Valiantzas, 2011). To the best of our knowledge, this is the first attempt to simulate $P_c(S_w)$ and $K(S_w)$ using a combination of both PMB and LB models on the basis of a 3D μCT image of a real soil structure at a submicron voxel resolution.

MATERIALS AND METHODS

Materials

The soil sample was collected from the "Ap18" horizon, 18 cm deep, from an experimental research farm at Scheyern, near Munich (Germany) in July 2010. According to the World Reference Base for Soil Resources 2006 and the Food and Agriculture Organization (FAO), the soil was classified as a Luvisol that had developed from weathered loess. The properties of this type of soil, including good nutrient levels and drainage, make it suitable for a wide range of agricultural purposes. The soil was crumbly, with spherical fine and medium (1–5 mm) granular peds, and it was classified as a medium-textured loam (FAO class "Medium", UK soil type "SaSiLo", US Department of Agriculture and International Soil Science Society soil type "SiLo", German soil type "Slu"). The physicochemical parameters of the soil were determined in a previous study, and were: dry bulk density ρ_t = 1.50 ± 0.04 g cm^{-3}; textural components 40 wt. % sand, 45 wt. % silt, and 15 wt. % clay; pH_{CaCl_2} = 5.3; total C_{org} = 13.6 mg g^{-1}; total N =

1.32 mg g^{-1} (C/N = 10.3) (Khan et al., 2012). The soil was chilled immediately after collection by placing it in liquid nitrogen, to avoid microfaunal activity disturbing the soil structure, and it was kept frozen (at −20 °C) until it was analyzed.

Synchrotron-based X-ray computed tomography and image processing

The imaging of the soil ped sample was carried out at the Swiss Light Source Tomographic Microscopy and Coherent Radiology Experiment (TOMCAT) beamline facility at the Paul Scherrer Institute in Villigen, Switzerland. A low X-ray absorption by different phases may lead to difficulties in obtaining good contrast, and this can have a direct impact on the quantitative analysis of the 3D microstructure and the subsequent segmentation. TOMCAT scientists have made remarkable improvements in the technique to overcome this problem, including applying "edge enhanced" (Stampanoni et al., 2006) and "phase contrast" (Bronnikov, 2002) techniques. The complete beam-line specifications were published previously (Marone et al., 2009), together with the experimental setup for measuring soil ped samples (Khan et al., 2012). These details are not repeated here, but the essential experimental details are shown in Table 1.

The original pixel spatial resolution of 0.37 μm was binned at twice that size, to improve the signal-to-noise ratio, resulting in a final spatial resolution of 0.74 μm in the reconstructed images. The fast reconstruction of the complete data set was performed by applying a combined wavelet fast Fourier transform (wFFT) decomposition algorithm. The wFFT approach deals with typical artifacts related to data incompleteness during the padding of the sinograms "on-the-fly", before reconstruction (Marone et al., 2010). After the raw sample data (2.048 × 2.048 × 2.048 voxels) had been reconstructed in 3D and the dataset had been converted into 16-bit images, the images were processed further by filtering out noise to smooth the data. Limited computing resources were available for the 3D imaging and modeling of such a high-resolution dataset, so it was necessary to select a region-of-interest (ROI) spatial domain, as shown in Fig. S1 in the supplementary information. The ROI dimensions were 500 × 500 × 1000 voxels, with a spatial resolution of 0.74 μm. Filtering techniques were used in the image processing and pattern recognition processes, to improve the subsequent segmentation (as described in the supporting information).

Pore-morphology based approach

Porous media have complex microstructures, and the capillary pressure (P_c) at an equilibrium state is determined by the mean curvature radius of the interface between the WP and the NWP. The relationship between P_c and the curvature of the wetting/non-wetting phase (WP–NWP) interface is governed by the Young–Laplace equation,

$$P_c = \gamma\left(\frac{1}{r_1}+\frac{1}{r_2}\right)\cos\theta, \qquad (1)$$

Energy (keV)	View angle / step size (°)	Pixel size (μm)	Mean exposure time (sec)	Field of view (mm × mm)	Imaging objective	No. of projections
20	0.12	0.37	0.14	1.5 × 1.5	20×	1501

Table 1 Experimental parameters used for the X-ray computed microtomography (μCT)

where γ is the surface tension between the WP and the NWP, θ is the contact angle between the WP and the solid matrix, and r_1 and r_2 are the curvature radii along the *x*- and *y*-directions of the air–water interface, respectively. Drainage (de-wetting) and imbibition (re-wetting) were simulated in a 3D image using a pore morphology based (PMB) approach. The mathematical description used for simulating drainage in the PMB approach was based on a method suggested by Hilpert and Miller (2001), while the imbibition simulation was based on the method developed by Ahrenholz et al. (2008). The PMB method first decomposes the 3D image into pore voxels, and each is assigned a characteristic pore radius parameter. The morphological operation, which involves fitting the accessible pore volume opening with spheres of different sizes, as structuring elements (SEs), is then performed. We assumed that the interfaces between WP and NWP in the porous media could be approximated by spherical cap surfaces. The curvature radii for all the WP–NWP interfaces defined in eq. 1 are, therefore, equal to the unique SE radii. In this method, the ratio of the pore space occupied by fitted spheres to the total pore volume is determined and used to define the degree of WP–NWP saturation within the porous medium. The effective hydraulic properties of the porous medium, such as the capillary pressure–saturation relationship, can, therefore, be established by simplifying eq. 1 to

$$P_c = \frac{2\gamma\cos\theta}{r},\ \theta \neq 0, \qquad (2)$$

where *r* is the capillary (pore) radius. The PMB simulation was performed using the commercial software program package GeoDict (http://www.geodict.com), which was developed by Fraunhofer ITWM and distributed by Math2Market GmbH (Kaiserslautern, Germany).

Drainage simulation

The drainage algorithm starts with a completely water-filled pore space, the initial condition being $P_c = 0$. The simulation begins with a maximum pore radius r_{max}, and the procedure is repeated with stepwise decreases in the pore radius. In a 3D image of a square porous body, three planar faces (in each of the *x*-, *y*-, and *z*-directions) are connected to the air-phase reservoir, while the opposite three faces are connected to the water-phase reservoir. Here, we present the simulation of two different drainage process scenarios, A and B. In drainage simulation A, the model simulates and reproduces capillary pressure results in relation to WP and NWP saturation until the entire pore space is filled with air. This implies that the residual level of water saturation is not integrated into the system. In drainage simulation B, water voxels that are isolated (disconnected) from the main WP reservoir are labeled as residual water saturation (S_{wr}) of the porous medium.

Imbibition simulation

The imbibition algorithm starts with full water saturation (S_w) in the soil ROI. The simulation begins with a minimum pore radius, which is increased stepwise until pre-defined criteria are met. Two different imbibition process scenarios A and B are compared. In imbibition simulation A, the simulation ends when the last cluster of air is drained, while in imbibition simulation B, the entrapment of air, rather than water, is integrated and air voxels that are disconnected from the neighboring air reservoir are treated as residual air saturation (S_{nwr}) of the medium. Both simulations were set up to follow only the connected WP, which implies that the growing WP as a function of the pore volume (i.e., the pore radii) is associated with the neighboring or surrounding water voxels. The average contact angle and interfacial surface tension at 25 °C, for all of the cyclic processes, were fixed at 30° and 0.072 N m^{-1}, respectively. Our

algorithm does not, therefore, consider hysteresis caused by differences in the advancing and receding contact angles.

Lattice Boltzmann flow simulation

A numerical LB model scheme was used to solve the incompressible Newtonian water flow through the pore space in the water flow simulation. An elementary method for discretizing a numerical grid was used, taking a regular cubic lattice based on the tomographic image and considering cubic voxels from the digital μCT image. The LB method was used to solve the Boltzmann equation for an ensemble-averaged particle distribution on a discrete and finite lattice connected by fixed paths. D3Q15 velocity–space discretization was used in each of the simulations to achieve 15 possible particle movement directions, including the center point "null vector", in all cubic unit cells. Pioneering work, testing the multiple-relaxation-time lattice Boltzmann (MRT–LB) equation in 3D, was performed by d`Humières et al. (2002), who found a solution for the numerical defects and instability associated with the well known single-relaxation-time of Bhatnagar-Gross-Krook model. A fully parallelized LB solver, integrated in the GeoDict module, was applied using an MRT–LB model, which solved numerical errors using "magic numbers", associated with symmetric and anti-symmetric collision moments (d`Humières et al., 2009). A high-performance computer (HPC), with four Interlagos processors, each comprising 12 CPU cores and 512 GB of RAM, was used for all of the LB flow simulations. The number of iterations and the numerical accuracy were set to 10000 and 0.0001, respectively. The macroscopic boundary conditions were that there was no flow at solid boundaries, a "no slip" velocity, and that the pressures at the inlet and outlet of the flow domain were fixed. A pressure drop of 1 Pa was applied along each axial *x*-, *y*-, and *z*-direction between the inlet and outlet of the porous medium. A unique numerical solution was found at a temperature of 20 °C with a fluid density ρ of 998 kg m^{-3} and a dynamic viscosity η of 1 g m^{-1} s^{-1}. Periodic boundary conditions were imposed at the outlet boundary of the flow domain. The interconnected channel pattern at the outlet boundary is not likely to be the same as the inlet boundary topography, which may lead to flow distortions at the edges or boundaries. The boundaries were treated as symmetrical faces, "reflecting" the characteristics in order to ensure continuity of flow

RESULTS AND DISCUSSION

Geometric phase characterization

The most important part of our procedure is to extract unique characteristic properties from the 3D image microstructure, such as the pore size distribution (PSD), grain size distribution (GSD), porosity (including both open and closed pores), and specific surface area (SSA), and the PoroDict module of the GeoDict software package was used to achieve this using the 16-bit segmented 3D image. This software can generally predict physical properties from direct tomographic microstructural input.

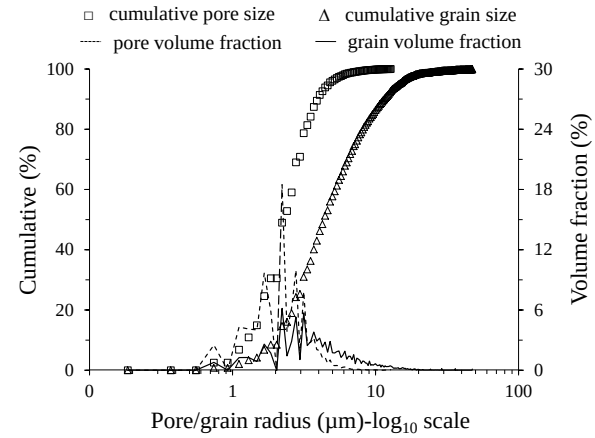

Fig. 1. Pore size distribution and grain size distribution in the sample, on a $\log_{10}$ scale. The cumulative fraction (%) for each distribution is represented as a symbol and the volume fraction (%) is represented as a solid or dashed line

Pore size distribution (radius-μm)			Total porosity $cm^3\ cm^{-3}$	Grain size distribution (radius-μm)			Specific surface area $m^2\ g^{-1}$
P10	P50	P90		G10	G50	G90	
1.25± 0.06	2.27 ± 0.14	3.97 ± 0.08	0.35 ± 0.04	2.03 ± 0.04	4.46 ± 0.13	11.92± 0.40	0.143 ± 0.003

Table 2 3D geometrical estimation of the sample region-of-interest

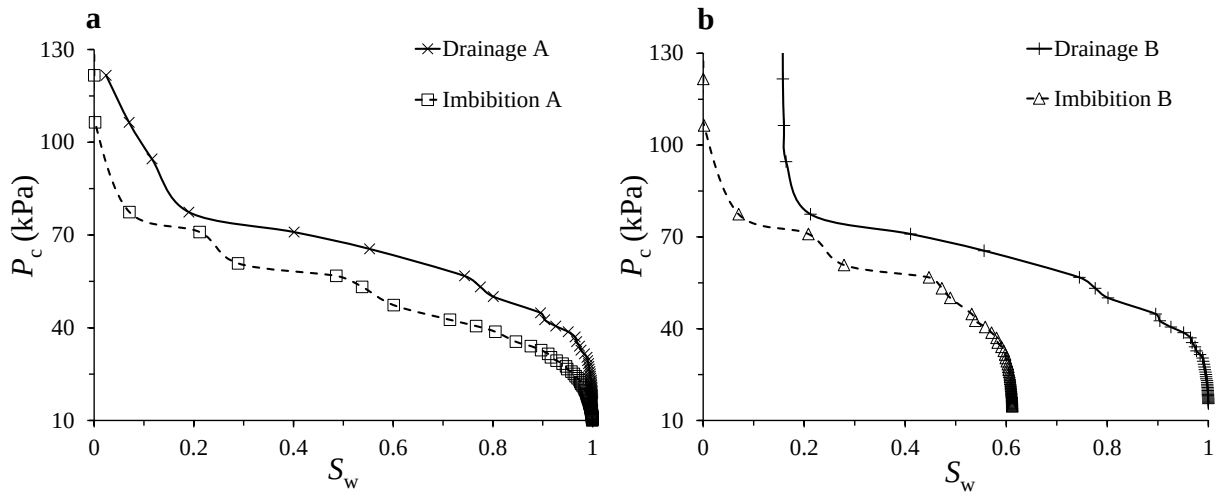

Fig. 2. Simulation results for the water retention curve, i.e., for the relationship between the capillary pressure and water saturation (P_c–S_w). (a) The drainage and imbibition processes in scenario A. (b) The drainage and imbibition processes in scenario B. The symbols represent the data points.

The PSD is a quantitative measure of the range of pore sizes in a given porous medium, and in our model this was determined by fitting the SEs (spheres) into the pore volume and by gradually increasing the size of the spheres, with an output step size (bin size) of radius 0.37 μm. A similar method was used to measure the GSD, by inverting the image structures. The cumulative and volume fraction pore and grain size results are shown in Fig. 1.

The P10, P50, and P90 values (the pore radii at 10%, 50%, and 90% of the cumulative pore results, respectively) were determined to allow the nature of the geometric PSD distribution to be interpreted in terms of the micro- and macro-pore contributions to the total pore volume. Similarly, the G10, G50, and G90 (the grain radii at 10%, 50%, and 90% of the cumulative grain results, respectively) were used to establish the GSD, ranging from finer to coarser grains. The porosity was estimated as a fraction of the bulk soil volume. The porosity of connected pore spaces was determined from the total number of voxels belonging to a cluster with neighboring voxels identified as pore spaces. The pore volume of the largest cluster was defined as the highest volume in a

soil sample that air–water interfaces could potentially occupy. The results from the PoroDict simulation runs are shown in Table 2.

Capillary pressure and water saturation

Water retention P_c–S_w curves were acquired from drainage and imbibition process simulation runs. The simulation of each process was achieved in a 3D image simultaneously in all three, *x*-, *y*-,and *z*-, directions, i.e., all three faces were connected to the air reservoir, while the three opposite faces were permeable to the water. The simulation output result for each pore radius increment, in relation to the image voxels, was set to 0.148 μm (0.2 voxels). For both drainage scenarios A and B, the first major entry of air was found after the accessible open pore radius of 7.8 μm had been intruded, giving a P_c value of 16 kPa (S_w ≈ 0.99). The S_w value dropped quickly, from 0.95 to 0.21 units, resulting in a P_c value of between 38 and 77 kPa, as shown in Fig. 2a,b. This gave an open pore radius of 1.6–3.5 μm, meaning that this pore space contributed 60% of the total pore volume, as shown in Fig. 1, and would be occupied by air or water if drained. In drainage scenario B, the disconnected water voxels were trapped in small pores connected to the main pore body, as shown in Fig. 3a (a 2D *xy*-slice). Stepwise decreases in pore radius led to the gradual increase of S_{wr} and the gradual decrease of S_w, as seen in Fig. 4a (which shows the ratio of the S_{wr} to the total S_w present in the pore volume). The S_{wr} prevailed in the porous medium at lower S_w values. No more water drained at S_w = 0.15, suggesting that only S_{wr} remained in the porous medium (represented by a solid line in Fig. 2b), and the simulation run was terminated. In drainage scenario A, the simulation run continued until a single drop of water was replaced by air, and only S_{nw} remained in the porous medium (represented by a solid line in Fig. 2a).

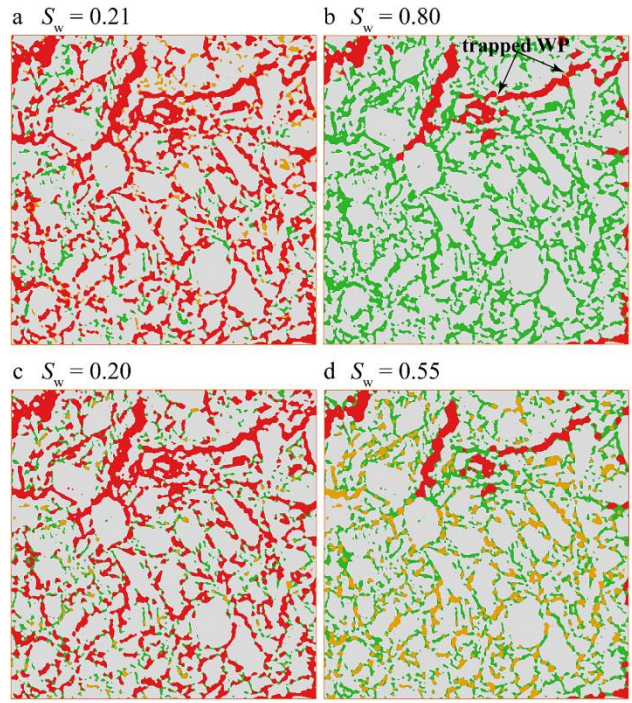

Fig. 3. A 2D (as an *xy* slice) image of the simulation output for the drainage B and imbibition B processes at different water saturation levels (S_w). Air is shown in red, water in green, solids in off-white, and the residual (trapped) fluid saturation in the pore network in orange. The orange areas in parts a and b are the residual water saturation (S_{wr}), and the orange areas in parts c and d are the residual air saturation (S_{nwr}). The edge length is 500 voxels (= 0.37 mm).

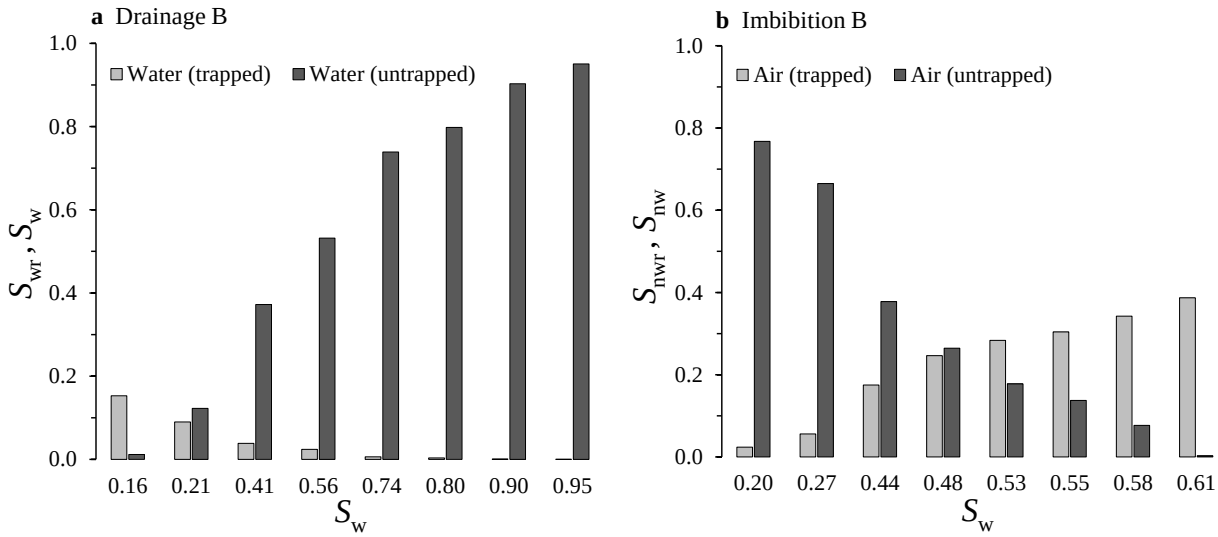

Fig. 4. The fluid–fluid saturation volume fractions at different water saturation (S_w) values. (a)The relationship between the residual and total water saturation (S_{wr}–S_w) in the drainage B cycle. (b)The relationships between the residual air saturation and water saturation (S_{nwr}–S_w) and between the air saturation and water saturation (S_{nw}–S_w) in the imbibition B cycle.

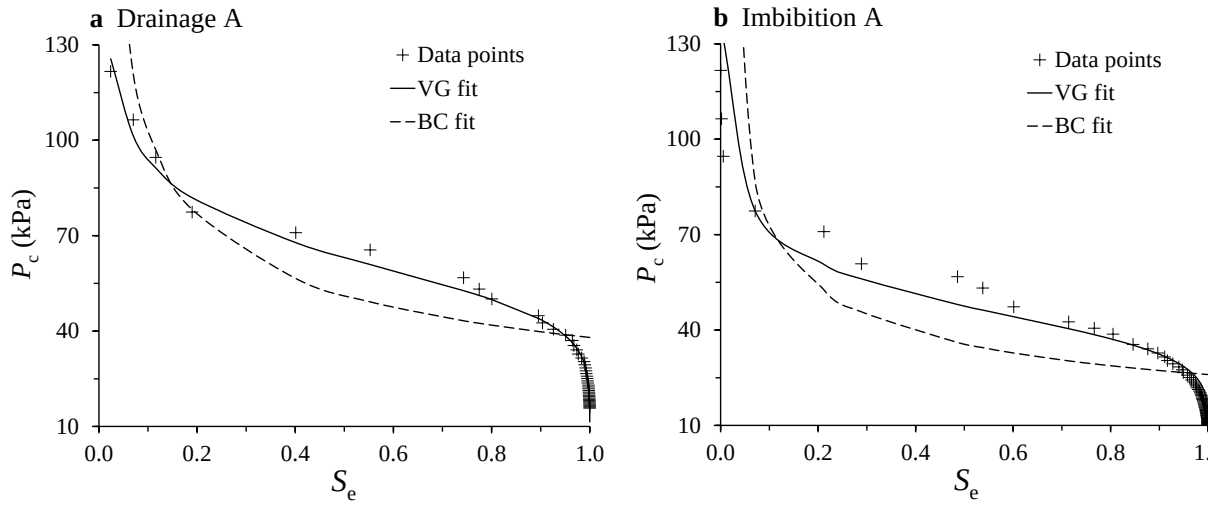

Fig. 5. The predicted capillary pressure (P_c) versus the effective water saturation (S_e) for (a) drainage, and (b) imbibition. The solid lines are the Van Genuchten (VG) model curve fits and the dashed lines are the Brooks–Corey (BC)model curve fits.

The input structure was set for the imbibition A and B scenario simulations so that the pores were completely filled with air, as the initial boundary condition. Therefore, the S_{wr} distribution at an initial water saturation of S_w = 0.15 was not considered in the porous medium. The simulation began with the smallest pores connected to the water reservoir, resulting in the highest P_c value in relation to the smallest starting pore radius (0.148 μm). A hysteresis was observed between drainage and imbibition in the P_c–S_w curves in scenarios A and B, because of the pore-size distribution and the connected-pore geometry (Fig. 2 a and b). In the P_c–S_w curve, imbibition scenario B eventually joined imbibition scenario A at a

lower saturation ($S_w \approx 0.27$), and started diverging when S_{nwr} was dominated by S_{nw}. This is shown in Fig. 4b, which shows the S_{nwr} and S_{nw} contributions to each S_w value. The distribution patterns for both S_{nwr} and S_{nw} are shown in Fig. 3d (a 2D *xy*-slice), to validate the imbibition scenario B curve at $S_w = 0.55$, and the S_{nwr} can be seen at relatively high pore radii. Analyzing the 3D image showed that the S_w reached a maximum slightly above 0.6 units.

A range of empirical and semi-empirical methods has been developed for predicting P_c in variably saturated porous media as a function of effective water saturation (S_e). The widely applied empirical water retention models of Brooks and Corey (1964) (hereafter BC) and Van Genuchten (1980) (VG) define the relationship between P_c and S_e, the relationship using the BC approach being

$$S_e = \left(\frac{P_b}{P_c} \right)^{\lambda} , \qquad (3)$$

where $P_c \geq P_b$. The relationship using the VG approach is

$$S_e = \left[1+(\alpha P_c)^n \right]^{-m} , \qquad (4)$$

where S_e is the normalized saturation of the wetting phase, also called the effective water saturation ($S_w - S_{wr}$)/(1 − S_{wr}), with a dimensionless value of $0 \leq S_e \leq 1$, S_w is the volumetric water content ($cm^3\ cm^{-3}$), S_{wr} is the residual water content ($cm^3\ cm^{-3}$), λ is the pore-size distribution index, P_b is the air entry pressure (which is roughly equal to the lowest capillary pressure at which the non-wetting fluid forms a continuous phase in the porous medium), P_c is the capillary pressure, and α (kPa^{-1}), *n*, and *m* (*m* = 1 − 1/*n*) are empirical shape-defining parameters. These parameters are used later to predict the relative hydraulic conductivity.

The curves fitted using eqs. 3 and 4 were only applied to the simulated drainage and imbibition process results for the no-trapping scenario A cases. These cases imply that there was no residual water saturation, i.e., $S_{wr} = 0$. The two empirical formulae, eqs. 3 and 4, were then rearranged to predict the capillary pressure P_c at different effective saturations. The fitting parameters, λ, α, and *n*, for these equations are shown in Table 3. The correlation coefficients of determination (R^2) and the root mean squared errors (RMSEs) were calculated to test the accuracies of the models. The RMSE is the square root of the mean of the squared difference between the simulated and calculated values, and is most useful when large errors are particularly undesirable (Poulsen et al., 2002). The P_b value for the BC model was set to 36 and 26 kPa for the simulated drainage and imbibition curves, respectively. The predicted data points for the P_c–S_e relationship are shown in Fig. 5. The VG model matched the simulated values well, with $R^2 > 0.99$ and RMSE = 2.11 kPa for drainage, and $R^2 = 0.90$ and RMSE = 5.68 kPa for imbibition. Similarly, the BC model predicted the P_c values well over the whole S_e range, with $R^2 = 0.73$ and RMSE = 17.6 kPa for drainage, and $R^2 = 0.60$ and RMSE = 24.3 kPa for imbibition.

Process cycle	Eq. 3	Eq. 4	
	λ	α (kPa^{-1})	*n*
Drainage	2.3	0.016	6.1
Imbibition	2.2	0.022	5.9

Table 3 The empirical constants used for fitting the P_c–S_e curves using the Brooks and Corey and Van Genuchten approaches

Specific interfacial area and water saturation

The specific area of the air–water interface (A_{awi}) was simulated only for the drainage and imbibition processes without fluid trapping, i.e., scenario A, using the GeoDict software package. The PoroDict module uses two different methods for each input microstructure. One of the methods is based on the statistical algorithm using the concept of the intersection of an object with straight line "segments", corresponding to different directions in space (Ohser and Mücklich, 2000), the estimator counting the surface crossings along the rays, i.e., the total length of the segments corresponding with the direction. However, this method is most consistent for isotropic media (i.e., with no preferred surface orientation). The other method uses a simple approach, counting and adding up the 3D image voxels, the results of which, for the A_{awi}–S_w relationship, are shown in Fig. 6 (the data points (square boxes, □) were calculated using statistical methods, and the other points denoted by crosses (×) were estimated by counting voxels). The highest A_{awi} values obtained using each method were in the ranges $0.20 < S_w < 0.25$ and $75 < P_c < 85$ kPa for drainage, and $0.45 < S_w < 0.60$ and $50 < P_c < 60$ kPa for imbibition. A_{awi} decreased as S_w decreased further. These observations agree well with the experimental data published by Culligan et al. (2004), showing that the simulation results were reliable for quantifying A_{awi}. A_{awi} was underestimated using the statistical method (Ohser and Mücklich, 2000) in both simulations, indicating that the method is biased when highly anisotropic media are studied, as was the case for our soil, which contained a significant proportion of clay particles. A_{awi} was much higher for imbibition than for drainage, especially at moderate water saturation levels. These observations agree well with pore-network modeling results using a high-porosity 2D micromodel (Joekar-Niasar et al., 2009) and LB simulations in a porous glass bead medium (Porter et al., 2009). The fluid phase distribution during drainage at $S_w = 0.55$ and during imbibition at $S_w = 0.53$ are shown in Fig. 7, to illustrate these results. The NWP was more uniformly distributed in the imbibition scenario (Fig. 7b) than in the drainage scenario (Fig. 7a). The different fluid–fluid distribution patterns at the same S_w in the two cycles were caused by the pore geometry and the PSD available for each pore radius simulation step. A review of the published experimental studies of the A_{awi}–S_w relationship suggested that, in general, imbibition curves are lower than drainage curves, but only a few studies have addressed this characteristic. This discrepancy is caused by the simple assumptions used in the simulation runs, such as the use of an average contact angle. These assumptions do not fully agree with the fundamental fluid physics of the receding and advancing phenomena and local capillarity surface tension in the experimental system during fluid displacement.

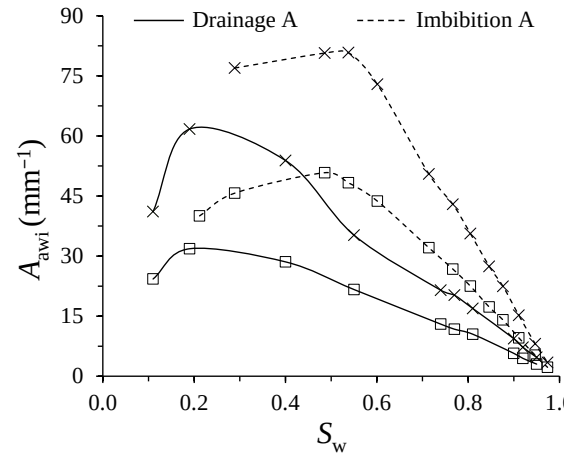

Fig. 6. The interfacial area (A_{awi}) as a function of water saturation (S_w). The symbols □ and × represent data points from statistical and direct counting methods, respectively.

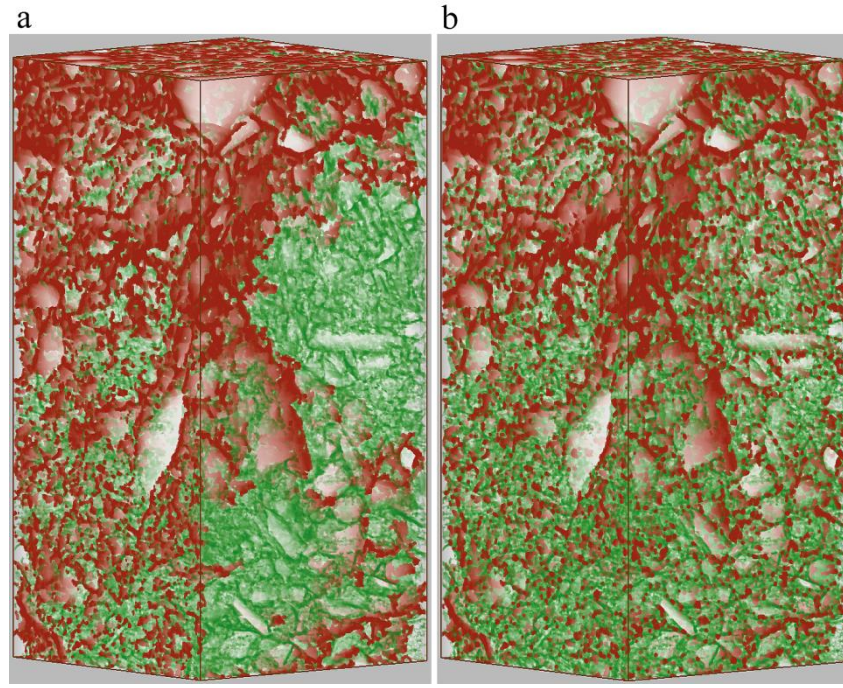

Fig. 7. 3D visualization of a water saturation (S_w) sample, showing (a) the drainage process at S_w = 0.55, and (b) the imbibition process at S_w = 0.53. Air is shown in red and water in green, and areas occupied by the solid matrix are white. The soil sample height is 0.74 mm (= 1000 voxels).

Water permeability tensor

The simulated permeability–water saturation relationship describes the ability of water to flow through the porous material. This relationship was established to determine the overall effect of the NWP distribution resulting from the drainage and imbibition simulation processes on water movement and, consequently, the influence of this relationship on the relative permeability, which is a dimensionless measure of the effective permeability of that phase (Jerauld and Salter, 2009). Only simulated drainage and imbibition scenarios without trapping were considered. The water flow was simulated assuming that the movement of one phase did not change the configurations of the other related phases in the porous medium, i.e., each fluid phase would find its own pathway. In other words, the effect of any momentum transfer across the fluid–fluid interface was ignored and, therefore, the air and solid phases were both considered to be immobile. Before the water flow simulations were performed using the LB approach, the 3D microstructure image was reprocessed by converting the bulk phases into their binary representations, i.e., the pore volumes occupied by the water phase, and the remaining solid and air phases.

In the LB model approach, the numerical simulation converged once the flow reached steady state. The average flow velocity was calculated as the sum of the velocity components in each voxel over the entire ROI pore volume. As an example, the pressure gradient and local velocity distribution in the presence of air are shown for the drainage process at S_w = 0.80 in Fig. 8a,b. Different pressure gradients, indicated using different colors in Fig. 8a, determine the flow velocity at the local pore scale. The velocity vector field was strongly constrained by the pore space occupied by air (Fig. 8b). Forced fluid flow in a complex 3D structure advances not only along the axial directions, but also in directions not parallel to the pressure gradient. A permeability tensor of nine

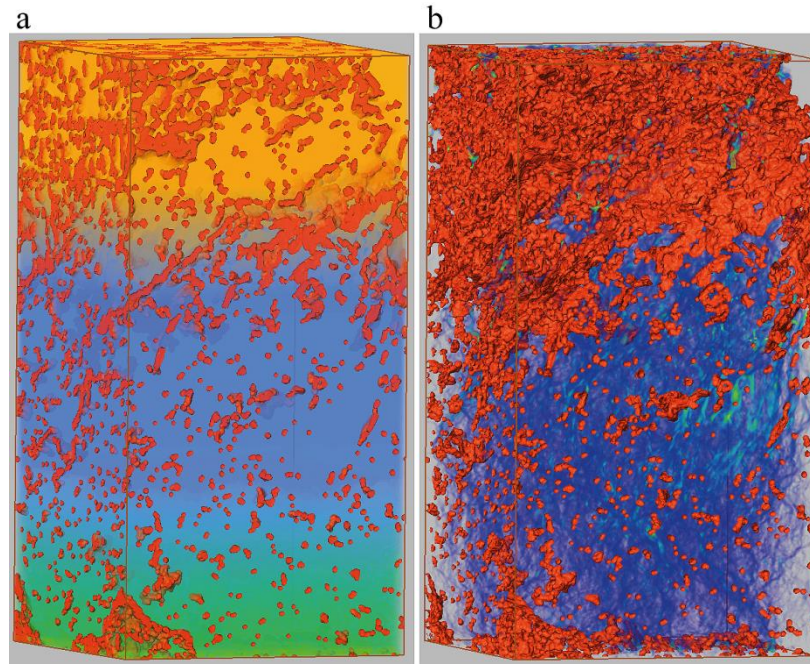

Fig. 8. 3D image of the drainage process at a water saturation of S_w = 0.80. (a) The pressure field in the *z*-direction, from a high value (orange) at the top to a low value (green) at the bottom. (b) The velocity vector in the *z*-direction, with a moderate velocity of $5\cdot\times 10^{-8}$ m s^{-1} shown in blue. Air is shown in red. The soil sample height is 0.74 mm (= 1000 voxels).

components (3 × 3) was, therefore, calculated, at a scale of 1 Darcy (10^{-12} m^2), using Darcy's basic incompressible fluid flow law, which gives the pressure drop per unit length of sample as a linear function of the mobile phase superficial velocity. Subsequently, the permeability ($\mathcal{K}$) values along the principal flow directions were recalculated to give the hydraulic conductivity values, $K = \mathcal{K}g\upsilon^{-1}$ (cm d^{-1}), where g is the acceleration caused by gravity (9.8 m s^{-2}), and υ is the kinematic viscosity (m^2 s^{-1}). A non-linear relationship was seen, the conductivity values exponentially increasing with increasing S_e, as shown in Fig. 9. The results along the axial *x*- and *y*-directions, i.e., the K_{xx} and K_{yy} conductivity values, were slightly higher for the drainage process than for the imbibition process. Unexpectedly, no such effect was seen on the hysteresis of K_{zz}. The highest average axial velocity in all of the simulations along the *x*-, *y*-, and *z*-directions was $4.2\cdot10^{-7}$ m s^{-1} at S_w = 1.0, which reflects a creeping flow throughout the model domain. The average pore velocity fluctuated by almost three orders of magnitude between low and high water saturation levels, but the pressure gradient remained constant. Using the LB approach on a 3D structure with S_w < 0.20 gave a flow problem caused by inadequate numbers of connected pores between the model ROI input and output boundaries under the periodic boundary conditions.

The results of the flow simulation were compared with predictions made using the well known empirical Brooks and Corey–Burdine (BCB) (Burdine, 1953; Brooks and Corey, 1964) and Van Genuchten–Mualem (VGM) (Van Genuchten, 1980; Mualem, 2010) models. The empirical model values shown in Table 3 were used to predict the relative hydraulic conductivity K_r using eq. 5 for the BCB model,

$$K_r = \frac{K(S_e)}{K_s} = S_e^{(2+3\lambda)/\lambda}, \qquad (5)$$

and eq. 6 for the VGM model,

$$K_r = \frac{K(S_e)}{K_s} = S_e^b \left[1 - (1 - S_e^{1/m})^m\right]^2, \quad (6)$$

where $K(S_e)$ and K_s are the unsaturated and saturated hydraulic conductivities, respectively, b is a dimensionless empirical constant (usually taken to be 0.5 (Mualem, 2010)), m is equal to $1 - 1/n$, and S_e is the effective water saturation.

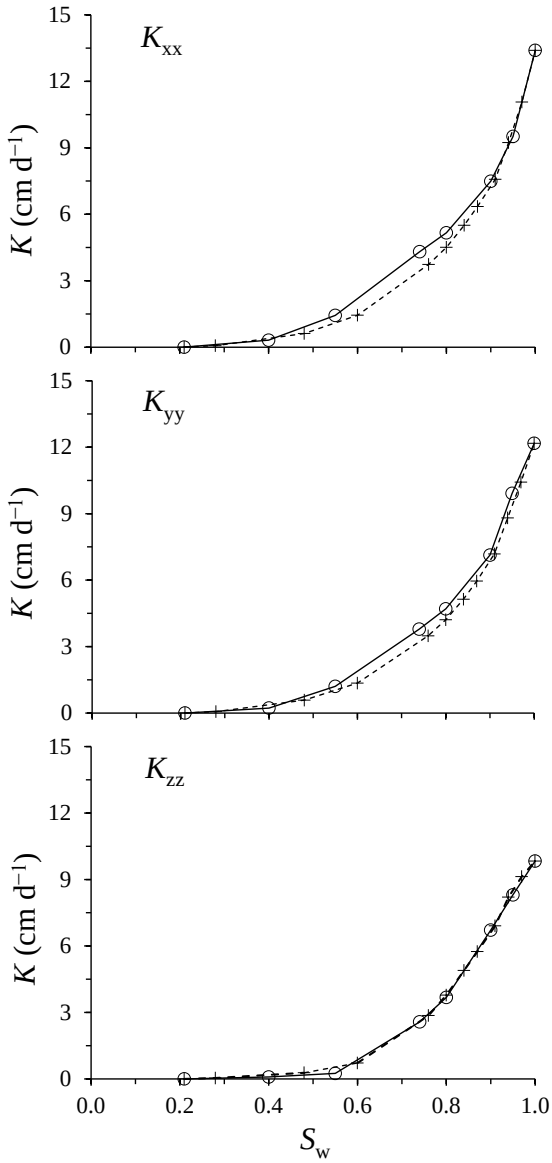

Fig. 9. Hydraulic conductivity along the *x*-, *y*-, and *z*-directions (K_{xx}, K_{yy}, and K_{zz}) versus water saturation (S_w). The solid lines represent the drainage process (with data points marked o) and the dashed lines show the imbibition scenarios A (with data points marked +).

The K_r values over the whole range of S_e of 0.20–1.0, were predicted using the BCB model, giving R^2 = 0.99 and RMSE = 0.02 for drainage, and $R^2 \geq$ 0.99 and RMSE = 0.04 for imbibition. However, the VGM model slightly overestimated the K_r values for both cyclic processes, especially when S_e was lower than moderate ($S_e < 0.60$), as is shown in Fig. 10. Even so, the VGM model results for both drainage and imbibition were not much worse than the BCB model results, giving $R^2 > 0.99$ and RMSE = 0.03 for drainage, and $R^2 \geq 0.99$ and RMSE = 0.05 for imbibition. The VGM model performed well for highly saturated media ($S_e > 0.80$). Statistical analysis showed that the prediction accuracy was slightly better for the BCB model than for the VGM model, especially at lower water saturation.

CONCLUSIONS

Wetting phase (WP) and non-wetting phase (NWP) displacement cycles were modeled using a μCT image of a real porous soil with minimum microstructure property biases, using a pore-morphology based (PMB) method. The aim was to link the classical constitutive relationship between the capillary pressure P_c and the water saturation S_w caused by the drainage and imbibition processes. Drainage was simulated in two scenarios, A and B, as the relative intrusion of the NWP into the largest available connected pore (voxel) spaces, i.e., the main pore network was connected to the air reservoir. In drainage scenario B, the simulated 3D image depicted the entrapment of WP as residual water saturation (S_{wr}) in small connected pores or pore throats (Fig. 3a), leading to the ratio of S_{wr} to the total S_w being dominant only after the wetting phase (S_w) reached 0.41 (Fig. 4a). The imbibition A and B scenario simulations were started with the intrusion of the WP connected to the WP reservoir. Careful examination of the simulated 3D images of imbibition scenario B, starting from small

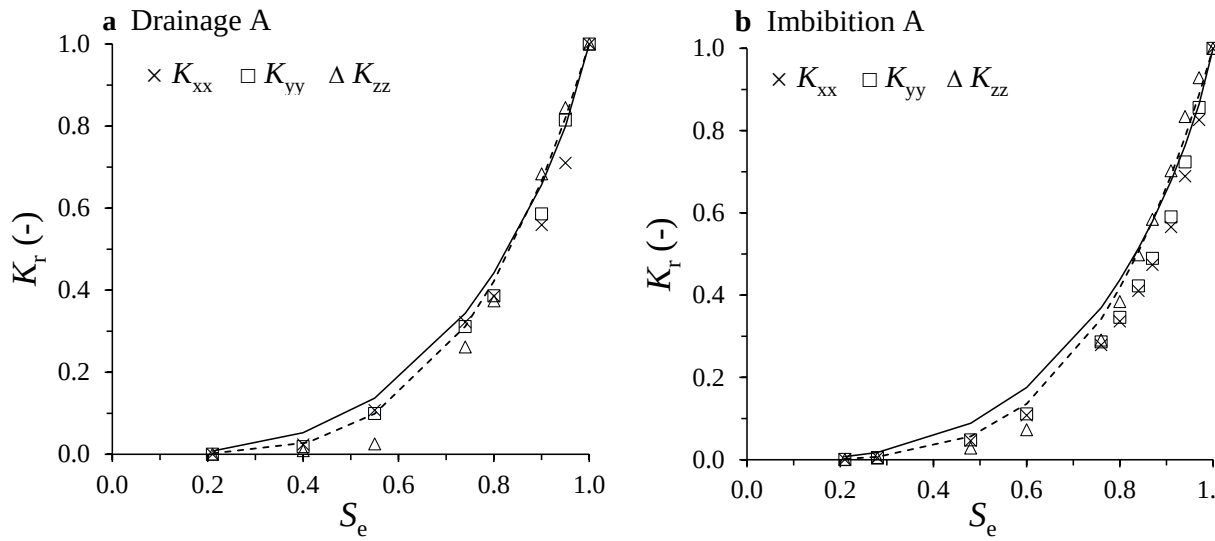

Fig. 10. The relationship between the relative hydraulic conductivity and the effective water saturation (K_r–S_e). The simulated data points are shown as symbols. The Brooks and Corey–Burdine model curves are shown as dashed lines and the Van Genuchten–Mualem model curves are shown as solid lines.

pores and moving to the large connected pores showed that the WP was initiated in small connected open pores, i.e., the SE fitting started at the smallest available pore radius in the porous medium. The main large pores occupied by the NWP are, therefore, surrounded by the WP, as shown in Fig. 3d. As a result, the presence of the total S_{nwr} and S_w (Fig. 4b) showed that S_{nwr} was 0.39 at the end of the simulation (represented by the dashed line in Fig. 2b). Non-linear P_c–S_w curves were established, caused by the connectedness and the pore-size distribution in the porous medium (Fig. 2 a and b).

The A_{awi}–S_w curves suggested that the air–water interfacial area increased as the water saturation decreased. This assumption was only true at higher and moderate saturation, S_w = 0.40–1.00. A hysteresis was established because of the effect of capillarity linked to the available PSD and interpore connectivity. 3D images at S_w = 0.53 showed the more uniform distribution of WP–NWP in the imbibition process than in the drainage process (Fig. 7 a and b), so A_{awi} was higher for the imbibition process than for the drainage process (Fig. 6).

The hydraulic conductivity of the WP was determined in the variably water-saturated porous medium, and the simulation results showed that it had a strong non-linear relationship with S_w, mainly caused by the dependency of the inter-connected pore-water structure on the main pore network. The simulation results for the hydraulic conductivity along the axial *x*- and *y*-directions (K_{xx} and K_{yy}, respectively) were higher for the drainage process than for the imbibition process in the range $0.20 < S_w < 0.80$, but the hysteresis was minimal. This suggests that the pore-size distribution occupied by water had only a minor influence on the hydraulic conductivity. Surprisingly, no such difference was observed in the K_{zz} (i.e., in the *z*-direction). The relative hydraulic conductivity results, as a function of the effective water saturation level, were compared with the results of well-known empirical prediction models (BCB and VGM). The predicted values from both models agreed well with the simulation results, especially at $S_e \geq 0.80$.

Integrating μCT soil images using PMB and LB modeling proved successful, enabling the P_c–S_w, A_{awi}–S_w,

and K–S_w relationships to be determined for the drainage and imbibition processes. The PMB approach was limited by its ability to determine the P_c–S_w curves of WP–NWP under equilibrium conditions by using a fixed contact angle (wettability) in all of the simulations. Thus, the meniscus curvature differences in capillaries induced by interfacial tension and surface roughness were also not considered. Further research is required to develop a more precise description of these complex phenomena.

ACKNOWLEDGMENTS

Financial support, provided by the German Research Foundation under the priority program "Biogeochemical Interfaces in Soil" (DFG-SPP 1315), is gratefully acknowledged. Jürgen Becker, from Fraunhofer-ITWM, helped with the use of the GeoDict software package.

REFERENCES

Ahrenholz, B., J. Tölke, P. Lehmann, A. Peters, A. Kaestner, M. Krafczyk, and W. Durner. 2008. Prediction of capillary hysteresis in a porous material using lattice-Boltzmann methods and comparison to experimental data and a morphological pore network model. Adv. Water Resour. 31:1151-1173.

Anderson, S.H., and J.W. Hopmans. 2013. Soil-Water-Root Processes: Advances in Tomography and Imaging. SSSA Special Publication 61, Madison (WI), USA. p. 285.

Ataie-Ashtiani, B., S.M. Hassanizadeh, and M.A. Celia. 2002. Effects of heterogeneities on capillary pressure-saturation-relative-permeability relationships. J. Contam. Hydrol. 56:175-192.

Bear, J., and A. Verruijt. 1987. Modelling groundwater flow and pollution. Reidel publishers, Doordrecht, Netherlands. p. 414.

Berg, S., S.A. Klapp, A. Schwing, R. Neiteler, N. Brussee, A. Makurat, L. Leu, F. Enzmann, J.-O. Schwarz, M. Kersten, S. Irvine, and M. Stampanoni. 2013. Real-time 3D imaging of Haines jumps in porous media flow. Proc. Natl. Acad. Sci. USA 110:3755-3759.

Blunt, M.J., B. Bijeljic, H. Dong, O. Gharbi, S. Iglauer, P. Mostaghimi, A. Paluszny, and C. Pentland. 2013. Pore-scale imaging and modeling. Adv. Water Resour. 51:197-216.

Boek, E. 2010. Pore scale simulation of flow in porous media using lattice-Boltzmann computer simulations. Soc. Petro. Eng. doi:10.2118/135506-MS.

Bronnikov, A.V. 2002. Theory of quantitative phase-contrast computed tomography. J. Opt. Soc. Am. A 19:472-480.

Brooks, R.H., and A.T. Corey. 1964. Hydraulic properties of porous media. Hydrol. Pap. 3:1-27.

Brusseau, M.L., S. Peng, G. Schnaar, and M.S. Costanza-Robinson. 2006. Relationships among air-water interfacial area, capillary pressure and water saturation for a sandy porous medium. Water Resour. Res. 42:W03501. doi:10.1029/2005WR004058.

Burdine, N.T. 1953. Relative permeability calculations from pore-size distribution data. Petr. Trans. Am. Inst. Mining Metall. Eng. 198:71-77.

Chan, T.P., and R.S. Govindaraju. 2011. Pore-morphology-based simulations of drainage and wetting processes in porous media. Hydrol. Res. 42:128-149.

Chang, L.C., H.H.Chen, H.Y. Shan, and J.P. Tsai. 2009. Effect of connectivity and wettability on the relative permeability of NAPLs. Environ. Geol. 56:1437-47.

Choi, H., and M.Y. Corapcioglu. 1997. Effects of colloids on volatile contaminant transport and air-water partitioning in unsaturated porous media. Water Resour. Res. 33:2447-2457.

Christensen, B.S.B. 2006. Using X-ray tomography and lattice Boltzmann modeling to evaluate pore-scale processes in porous media. Ph.D. diss., Tech. Univ., Denmark.

Costanza-Robinson, M.S., KH. Harrold, and R.M. Lieb-Lappen. 2008. X-ray microtomography determination of air-water interfacial area-water saturation relationships in sandy porous media. Environ. Sci. Technol. 42:2949-2956.

Crist, J.T., J.F. McCarthy, Y. Zevi, P. Baveye, J.A. Throop, and T.S. Steenhuis. 2004. Pore-scale visualization of colloid transport and retention in partly saturated porous media. Vadose Zone J. 3:444-450.

Culligan, K.A., D. Wildenschild, B.S.B. Christensen, W.G. Gray, M.L. Rivers, and A.F.B. Tompson. 2004. Interfacial area measurements for unsaturated flow through a porous medium. Water Resour. Res. 40:W12413.

Das, D.B., S.M. Hassanizadeh, B.E. Rotter, and B. Ataie-Ashtiani. 2004. A numerical study of micro-heterogeneity effects on upscaled properties of two-phase flow in porous media. Transp. Porous Media 56:329-350.

D´Humières, D., and I. Ginzburg. 2009. Viscosity independent numerical errors for Lattice Boltzmann models: From recurrence equations to "magic" collision numbers. Comput. Math. Appl. 58:823-840.

D´Humières, D., I. Ginzburg, M. Krafczyk, P. Lallemand, and L.S. Luo. 2002. Multiple-relaxation-time lattice Boltzmann

models in three dimensions. Philos. Trans. R. Soc. London, Ser. A 360:437-451.

Elyeznasni, N., F. Sellami, V. Pot, P. Benoit, L. Vieuble-Gonod, I, Young, et al. 2012. Exploration of soil micromorphology to identify coarse-sized OM assemblages in X-ray CT images of undisturbed cultivated soil cores. Geoderma 179-180:38-45.

Gao, Y., X. Zhang, P. Rama, Y. Liu, R. Chen, H. Ostadi, and K. Jiang. 2012. Calculating the anisotropic permeability of porous media using the Lattice Boltzmann method and X-ray computed tomography. Transp. Porous Media 92:457-462.

Galindo-Torres, S.A., A. Scheuermann, L. Li, D.M. Pedroso, and D.J. Williams. 2013. A Lattice Boltzmann model for studying transient effects during imbibition-drainage cycles in unsaturated soils. Comp. Phys. Comm. 184:1086-1093.

Gan, Y., F. Maggi, G. Buscarnera, and I. Einav. 2013. A particle-water based model retention hysteresis. Submitted to Geotechnique Letters. http://arxiv.org/abs/1307.5372

Ghaini, A, M.N. Kashid, and D.W. Agar. 2010. Effective interfacial area for mass transfer in the liquid-liquid slug flow capillary microreactors. Chem. Eng. Process. 49:358-366.

Gregory, P.J., D.J. Hutchison, D.B. Read, P.M. Jenneson, W.B. Gilboy, and E.J. Morton. 2003. Non-invasive imaging of roots with high resolution X-ray micro-tomography. Plant Soil 255:351-359.

Hassanizadeh, S.M., and W.G. Gray. 1993. Thermodynamic basis of capillary pressure in porous media. Water Resour. Res. 29:3389-3405.

Held, R.J., and M.A. Celia. 2001. Modeling support of functional relationships between capillary pressure, saturation, interfacial area and common lines. Adv. Water Resour. 24:325-343.

Helmig, R. 1997. Multiphase flow and transport processes in the subsurface. Springer, Berlin. p. 367.

Hilpert, M., and C.T. Miller. 2001. Pore-morphology-based simulation of drainage in totally wetting porous media. Adv. Water Resour. 24:243-255.

Jerauld, G.R., and S.J. Salter. 1990. The effect of pore-structure on hysteresis in relative permeability and capillary pressure: Pore-level modeling. Transp. Porous Media 5:103-151.

Joekar-Niasr, V., and S.M. Hassanizadeh. 2011. Effect of fluids properties on non-equilibrium capillarity effects: Dynamic pore-network modeling. Int. J. Multiphase Flow 37:198-214.

Joekar-Niasar, V., S.M. Hassanizadeh, and A. Leijnse. 2008. Insights into the relationships among capillary pressure, saturation, interfacial area and relative permeability using pore-network modeling. Transp. Porous Media 74:201-219.

Joekar-Niasar, V., S.M. Hassanizadeh, L.J. Pyrak-Nolte, and C. Berentsen. 2009. Simulating drainage and imbibition experiments in a high-porosity micromodel using an unstructured pore network model. Water Resour. Res. 45:W02430.

Joekar-Niasar, V., M. Prodanović, D. Wildenschild, and S.M. Hassanizadeh. 2010. Network model investigation of interfacial area, capillary pressure and saturation relationships in granular porous media. Water Resour. Res. 46:W06526.

Khan, F., F. Enzmann, M. Kersten, A. Wiegmann, and K. Steiner. 2012. 3D simulation of the permeability tensor in a soil aggregate on basis of nanotomographic imaging and LBE solver. J. Soil Sediment 12:86-96.

Koku, H., R.S. Maier, K.J. Czymmek, M.R. Schure, and A.M. Lenhoff. 2011. Modeling of flow in a polymeric chromatographic monolith. J. Chromatogr. A 1218:3466-3475.

Marone, F., C. Hintermüller, S. McDonald, R. Abela, G. Mikuljan, A. Isenegger , and M. Stampanoni. 2009. X-ray tomographic microscopy at TOMCAT. J. Phys.: Conf. Ser. 186. doi:10.1088/1742-6596/186/1/012042.

Marone, F., B. Münch, and M. Stampanoni. 2010. Fast reconstruction algorithm dealing with tomography artifacts. Proceedings of SPIE: Developments in X-ray tomography VII 7804. doi:10.1117/12.859703.

Mualem, Y. 2010. Hysteretical models for prediction of the hydraulic conductivity of unsaturated porous media. Water Resour. Res. 12:1248-1254.

Nabovati, A., and A.C.M. Sousa. 2007. Fluid flow simulation in random porous media at pore level using the lattice Boltzmann method. J. Eng. Sci. Technol. 2:226-237.

Ohser, J., and F. Mücklich. 2000. Statistical analysis of microstructures in materials science. John Wiley & Sons, Chichester. p. 114-117.

Peth, S. 2010. Applications of microtomography in soils and sediments. Dev. Soil Sci. 34:73-101. doi:10.1016/S0166-2481(10)34003-7.

Pierret, A., Y. Capowiez, L. Belzunces, and C.J. Moran. 2002. 3D reconstruction and quantification of macropores using X-ray computed tomography and image analysis. Geoderma 106:247-271.

Porter, M.L., M.G. Schaap, and D. Wildenschild. 2009. Lattice-Boltzmann simulations of the capillary pressure-saturation-interfacial area relationship for porous media. Adv. Water Resour. 32:1632-1640.

Poulsen, T.G., P. Moldrup, B.V. Iversen, and O.H. Jacobsen. 2002. Three-region Campbell model for unsaturated hydraulic

conductivity in undisturbed soils. Soil Sci. Soc. Am. J. 66:744-752.

Prodanović, M., W. Lindquist, and R.S. Seright. 2007. 3D image-based characterization of fluid displacement in a Berea core. Adv. Water Resour. 30:214-226.

Rezanezhad, F., W.L. Quinton, J.S. Price, D. Elrick, T.R. Elliot, and R.J. Heck. 2009. Examining the effect of pore size distribution and shape on flow through unsaturated peat using computer tomography. Hydrol. Earth Syst. Sci. Discuss. 6:3835-62.

Schaap, M.; M. Porter, B. Christensen, D. Wildenschildt. 2007. Comparison of pressure-saturation characteristics derived from computed tomography and lattice Boltzmann simulations. Water Resour. Res. 43:W12S06.

Shi, X.Y., H. Gao, V.I. Lazouskaya, Q. Kang, Y. Jin, and L.P. Wang. 2010. Viscous flow and colloid transport near air-water interface in a microchannel. Comput. Math. Appl. 59:2290-2304.

Sirivithayapakorn, S, and A. Keller. 2003. Transport of colloids in unsaturated porous media: A pore-scale observation of processes during the dissolution of air-water interface. Water Resour. Res. 39:1346-1355.

Stampanoni, M., A. Groso, A. Isenegger, G. Mikuljan, Q. Chen, A. Bertrand, S. Henein, R. Betemps, U. Frommherz, P. Bohler, D. Meister, M. Lange, and R. Abela. 2006. Trends in synchrotron-based tomographic imaging: the SLS experience. Proceedings of SPIE: Developments in X-ray Tomography V 6318. doi:10.1117/12.679497.

Steenhuis, T.S., A. Dathe, Y. Zevi, J.L. Smith, B. Gao, S.B. Shaw, D. DeAlwis, S. Amaro-Garcia, R. Fehrman, M. E. Cakmak, I. C. Toevs, B. M. Liu, S. M. Beyer, J. T. Crist, A. G. Hay, B. K. Richards, D. DiCarlo, J. F. McCarthy. 2006. Biocolloid retention in partially saturated soils. Biologia 61 (Suppl. 19): S229-S233. doi: 10.2478/s11756-006-0163-0.

Sukop, M.C., H. Huanq, C.L. Lin, M.D. Deo, K. Oh, and J.D. Miller. 2008. Distribution of multiphase fluids in porous media: Comparison between lattice Boltzmann modeling and micro-X-ray tomopraphy. Phys. Rev. E 77:026710.

Torkzaban, S., S.M. Hassanizadeh, J.F. Schijven, and H.H.J.L. Van den Berg. 2006. Role of air-water interfaces on retention of viruses under unsaturated conditions. Water Resour. Res. 42:W12S14. doi:10.1029/2006WR004904.

Valiantzas, J.D. 2011. Combined Brooks-Corey/Burdine and Van Genuchten/Mualem closed-form model for improving prediction of unsaturated conductivity. J. Irrig. Drain. Eng. 137:223-233.

Van Genuchten, M.T.H. 1980. A closed-form equation for predicting the hydraulic conductivity of unsaturated soils. Soil Sci. Soc. Am. J. 44:892-898.

Wildenschild, D., and A.P. Sheppard. 2013. X-ray imaging and analysis techniques for quantifying pore-scale structure and processes in subsurface porous medium systems. Adv. Water Resour. 51:217-246.

Wan, J., and J.L. Wilson. 1994. Visualization of the role of the gas-water interface on the fate and transport of colloids in porous media. Water Resour. Res. 30:11-23.

Supporting Information

(Paper III)

Pore morphology and lattice Boltzmann approach to modeling unsaturated soil capillary hysteresis and permeability tensor

Supporting Information

This Supporting Information gives some more detailed methodological explanation on the μCT image post-processing steps including region-of-interest selection, filtering, and segregation.

1. Region-of-interest selection

Recent developments in synchrotron-based X-rays computed tomography (μCT) enable us for an effective visualization of complex pore-geometry up to submicron voxel resolution (= 0.74 μm). Further processing or investigation on the reconstructed 3D raw data of 2.048^3 voxels demands high computing (HPC) resources. Therefore, it is necessary to select a region-of-interest (ROI) best representing the whole domain as shown in Fig. S1. The ROI dimensions are thus reduced to 500x500x1000 voxels in which lattice Boltzmann calculations can well be performed using a server size HPC facility (64 cores, 1 TB RAM).

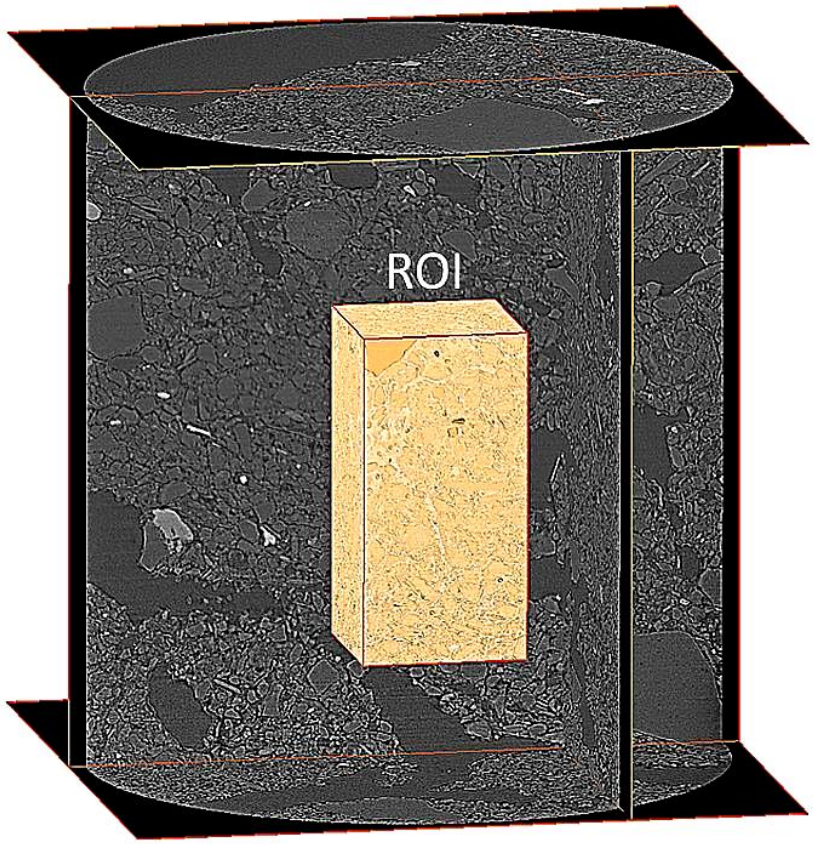

Fig. S1. Selection of best ROI with in original sample of dimensions 2.048^3 voxels. The ROI height is 0.74 mm (= 1000 voxels), and width is 0.37 mm (= 500 voxels).

2. Filtering and segregation method

Nonlinear filtering (NF) methods have attained much attention in the image post-processing due to their ability to preserve the edges while smoothing the noise. A range of de-noising methods have been developed by implementing iterative NF methods such as anisotropic diffusion (Perona and Malik, 1990), or by utilizing non-iterative NF methods with an edge-preserving capability such as bilateral filtering (Tomasi and Manduchi, 1998), mean shift filter (Domínguez et al., 2003), and 3D median filtering (Jiang and Crookes, 2006). We used the latter approach with help of the common AMIRA/AVIZO software package run on each sub-volume mask (3x3x3) to reduce uncorrelated noise, which is a typical result of μCT imagery. The replacement of voxels by median of neighboring voxels causes smoothing of raw data. After filtering, the image is segmented by assigning a material-specific value to each voxel in the grey-scale image, and binarized by separating features of interest between void and solid phases only. We are well aware of the fact, that the application of various thresholding and locally adaptive segmentation techniques on μCT gray scale images yield vastly differing results with respect to micro-scale pore characterization and fluid dynamics simulation (Lee and Chung, 1990; Tabb and Ahuja, 1997; Oh and Lindquist, 1999; Kanungo et al., 2002; Iassonov et al., 2009; Ojeda-Magaña et al., 2009; Baveye et al., 2010; Wang et al., 2011). Although the grey-scale range (GSR) histogram of the entire dataset is not very decisive (Fig. S2), it is still easily segregable into the two phases of interest (voids and solid matrix) based on the edge enhancement effect as a typical feature for parallel beam synchrotron μCT.

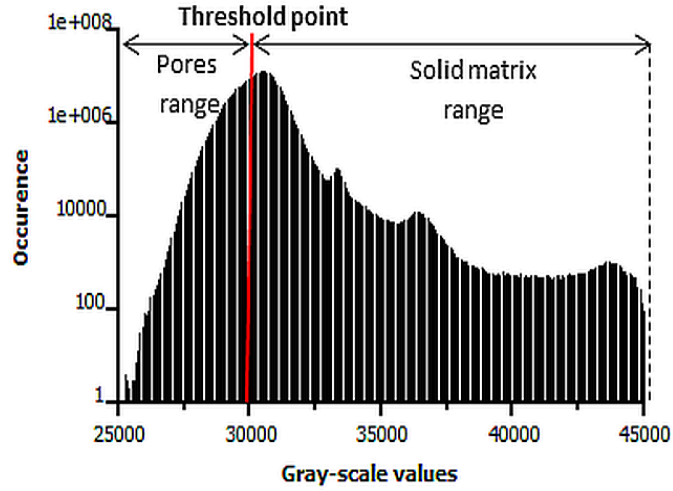

Fig. S2. Sample grey-scale values histogram for the entire 3D ROI dataset

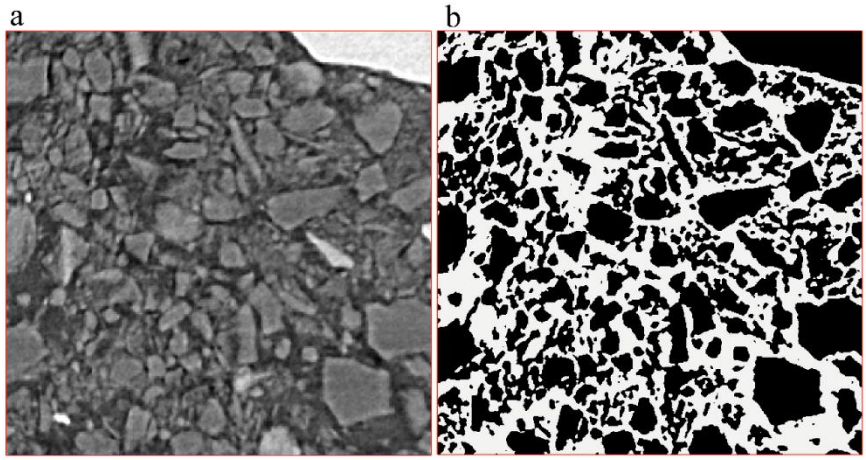

Fig. S3. Segmentation process with (a) original image 2D slice (*xy* slice), and (b) resulting segmented 2D image where white pixels represent the pore network of the soil aggregate (edge length 500 voxels = 0.37 mm).

Based on that effect, a threshold value is chosen carefully, and a GSR was set for each phase with reference to a global threshold value. This is justified because of the use of monochromatic synchrotron radiation, where the absorption coefficient for each voxel remains the same independent of the projection angle. The ambits of each phase with the chosen GSR ranges are controlled slice-by-slice by employing the AVIZO visualization software. This simple approach enabled us to convert ultimately the whole raw grey-scale into a reliable binary black-and-white image representing solids and voids as shown in Fig. S3.

References

Baveye P.C., M. Laba, W. Otten, L. Bouckaert, P.D. Sterpaio, R.R. Goswami, et al. 2010. Observer-dependent variability of the thresholding step in the quantitative analysis of soil images and X-ray microtomography data. Geoderma 157:51-63.

Domínguez G., H. Bischof, and R. Beichel. 2003. Fast 3D mean shift filter for CT images. Proceedings of the 13th Scandinavian conference on image analysis p. 438-445.

Iassonov P., T. Gebrenegus, and M. Tuller. 2009. Segmentation of X-ray computed tomography images of porous materials: A crucial step for characterization and quantitative analysis of pore structures. Water Resour. Res. doi:10.1029/2009WR008087.

Jiang M., and D. Crookes. 2006. High-performance 3D median filter architecture for medical image despeckling. Electron. Lett. 42:1379-1380.

Kanungo T., D.M. Mount, N.S. Netanyahu, C.D. Piatko, R. Silverman, and A.Y. Wu. 2002. An efficient k-means clustering algorithm: Analysis and implementation. IEEE, Pattern Anal. Mach. Intell. 24:881-892.

Lee S.U., and S.Y. Chung. 1990. A comparative performance study of several global thresholding techniques for segmentation. Comput. Vis. Graph. Image Process. 52:171-190.

Oh W., and W.B. Lindquist. 1999 Image thresholding by indicator kriging. IEEE, Pattern Anal. Mach. Intell. 21:590-602.

Ojeda-Magaña B., J. Quintanilla-Domínguez, R. Rueles, and D. Andina. 2009. Images sub-segmentation with the PFCM clustering algorithm. 7th IEEE International conference on industrial informatics. p. 499-503.

Perona P., and J. Malik. 1990. Scale-space and edge detection using anisotropic diffusion. IEEE Tans. Pattern. Anal. Mach. Intell. 12:629-639.

Tomasi C., and R. Manduchi. 1998. Bilateral filtering for gray and color images. Proceedings of the IEEE International conference on computer vision, Bombay p. 839-846.

Tabb M., and N. Ahuja. 1997 Multiscale image segmentation by integrated edge and region detection. IEEE Trans. Image Process. 6:642-655.

Wang W., A.N. Kravchenko, A.J.M. Smucker, and M.L. Rivers. 2011 Comparison of image segmentation methods in simulated 2D and 3D microtomographic images of soil aggregates. Geoderma 162:231-241.